

*Department of Construction Sciences*  
Solid Mechanics

ISRN LUTFD2/TFHF-18/5225-SE(1-96)

# **Simulation of Delamination Migration in Laminated Composite Structures**

**– An Approach Combining Extended Finite Elements  
and a Cohesive Zone Model**

Master's Dissertation by  
**Viktor Björklund**

**Supervisors:**

Assoc. Prof. Ralf Denzer  
Division of Solid Mechanics, Lund University

Assoc. Prof. Heinz Pettermann  
Univ. Ass. Jan Kaul  
Institute of Lightweight Design and Structural Biomechanics, E317  
TU Wien

**Examiner:**

Prof. Mathias Wallin  
Division of Solid Mechanics, Lund University

Copyright © 2018 by the Division of Solid Mechanics  
and Viktor Björklund

Printed by Media-Tryck AB, Lund, Sweden

For information, address:

Division of Solid Mechanics, Lund University, Box 118, SE-221 00 Lund, Sweden

Webpage: [www.solid.lth.se](http://www.solid.lth.se)



## Abstract

Fiber-reinforced polymer matrix composites are being used increasingly in lightweight applications where high strength and stiffness is required. One of the main challenges with designing components from such materials is to predict the ultimate strength and behaviour of the structure. Furthermore, due to anisotropic material response and a complex micro structure, various interacting failure modes exist.

In the present work, the interaction between inter- and intralaminar cracks that causes delamination to migrate from one ply interface to another is simulated for cross-ply laminates. A modeling approach that combines the extended finite element method and a surface-based contact formulation with a cohesive zone model is employed. This enables the propagation of arbitrary intralaminar cracks and delamination to be predicted, and non-linear material effects in the process zone ahead of the crack tip can be accounted for.

Two experiments from the literature are simulated in order to evaluate the performance and the predictive capabilities of the modeling approach. Differences between experiments and simulations are found regarding the intralaminar crack path and the force-displacement response of the structure. However, the series of unstable fracture events, including delamination migration is successfully simulated. The predicted delamination length, crack direction and migration location is in good agreement with the experimental results. The presented approach is computationally demanding and lacks flexibility but shows that with further improvements, more efficient and accurate modeling techniques can be developed based on the same concepts.





## Acknowledgment

This work has been carried out in collaboration with the Institute of Lightweight Design and Structural Biomechanics at TU Wien. I would like to express my deepest gratitude to Prof. Heinz Pettermann and Univ. Ass. Jan Kaul for providing me this opportunity. Their invaluable guidance, support and feedback throughout this work has helped me improving my engineering and analytical skills. Moreover, their ideas and profound knowledge has greatly contributed to giving me further insight into the topic and triggered my curiosity for this research field.

I would like to thank the Crafoord Foundation for granting me financial support for the work with this project and during my stay in Vienna. A big thanks goes to each of my student colleagues for their companionship and support, but also for keeping our minds on anything but studying when we need it the most. I would also like to express my gratitude to my family and friends in Lund. Finally, I want to thank Anja Stauffer for her endless support, encouragement and for always keeping my spirits up.

Viktor Björklund  
Wien, April 2018



# Contents

Abstract . . . . .	I
Acknowledgment . . . . .	III
List of Figures . . . . .	VII
List of Tables . . . . .	IX
<b>1 Introduction</b>	<b>1</b>
1.1 Delamination migration in fiber-reinforced polymers . . . . .	2
1.2 Review of previous work on the topic . . . . .	5
1.3 Scope of the present work . . . . .	7
<b>2 Experiments from the literature</b>	<b>9</b>
2.1 Delamination migration in a single cantilever beam . . . . .	9
2.2 Delamination migration in a curved laminate . . . . .	14
<b>3 Theory</b>	<b>17</b>
3.1 Fracture mechanics . . . . .	17
3.1.1 Linear elastic fracture mechanics . . . . .	18
3.1.2 Mixed mode fracture criterion . . . . .	21
3.1.3 Kinking of cracks in isotropic materials and bi-material interfaces	22
3.2 Progressive damage modeling . . . . .	23
3.2.1 Damage mechanics and stiffness degradation . . . . .	24
3.2.2 The Dugdale model . . . . .	25
3.2.3 The cohesive traction-separation model . . . . .	26
3.2.4 The cohesive traction-separation model under mixed-mode loading . . . . .	29
3.3 XFEM formulation . . . . .	32
3.3.1 FEM – Strong and weak form . . . . .	32
3.3.2 XFEM – Enrichment of the FEM formulation . . . . .	34
3.3.3 Definition of XFEM matrices . . . . .	35

3.3.4	Crack modeling in XFEM . . . . .	37
<b>4</b>	<b>Method</b>	<b>41</b>
4.1	The general structure of the continuum model with propagating cracks	41
4.2	Ply Modeling . . . . .	42
4.2.1	Crack propagation in XFEM . . . . .	43
4.2.2	Practical application of XFEM for propagating cracks . . . . .	45
4.3	Interface modeling . . . . .	47
4.3.1	Discretisation of the cohesive interfaces . . . . .	48
4.4	Viscous regularisation . . . . .	49
4.5	FEM model of the single cantilever beam test . . . . .	49
4.6	FEM model of the L-flange test . . . . .	52
4.7	The simulation procedure . . . . .	55
<b>5</b>	<b>Results</b>	<b>59</b>
5.1	Computational results from the single cantilever beam simulations . . .	59
5.1.1	Mesh sensitivity . . . . .	63
5.1.2	Energy evaluation . . . . .	65
5.1.3	The snap-back behaviour of the structure and the influence of viscous regularisation . . . . .	66
5.1.4	Comparison between simulation and experiment for the SCB test	70
5.2	Computational results from the L-flange simulation . . . . .	75
5.2.1	Comparison between simulation and experiment for the L-flange	78
5.2.2	The effect of interface strength and toughness . . . . .	80
5.3	Assessment of the modeled interaction between inter- and intralaminar cracks . . . . .	81
<b>6</b>	<b>Discussion and conclusions</b>	<b>85</b>
6.1	Concluding remarks . . . . .	87
6.2	Future work . . . . .	87
	<b>Appendices</b>	<b>88</b>
	<b>Appendix A</b>	<b>89</b>
	<b>Appendix B</b>	<b>91</b>
	<b>Bibliography</b>	<b>93</b>

# List of Figures

1.1	Delamination and a transverse matrix crack in a cross-ply FRP. . . . .	3
1.2	Homogenisation of the material properties for FRP plies . . . . .	4
2.1	Specimen configuration and load introduction in the SCB test [33]. . .	10
2.2	Force-displacement response of a specimen in the SCB test [33] . . . . .	12
2.3	Delamination and crack migration in the SCB test . . . . .	13
2.4	A detailed picture of an actual specimen from the SCB test [33] . . . . .	13
2.5	The experimental test set-up for the curved L-flange laminate in [37] . .	15
2.6	A migrated interface crack in a specimen from the L-flange test in [37].	16
3.1	The local cylindrical coordinate system $(r, \theta)$ with origin at the crack tip.	18
3.2	The three modes for loading of a crack [9]. . . . .	19
3.3	A crack kinking out of a bi-material interface . . . . .	23
3.4	The <i>Dugdale model</i> . . . . .	26
3.5	The cohesive zone modeling approach . . . . .	27
3.6	The bi-linear traction-separation model for single-mode loading. . . . .	28
3.7	The traction-separation model for mixed-mode loading . . . . .	31
3.8	Crack represented by level-set functions in a 2D-domain. . . . .	38
3.9	XFEM representation of a crack in a 2D-domain. . . . .	39
4.1	Conceptual overview of the applied crack models . . . . .	42
4.2	Propagating XFEM crack . . . . .	44
4.3	Boundary conditions and load introduction for the SCB model . . . . .	50
4.4	Schematic contact discretisation . . . . .	51
4.5	Boundary conditions and load introduction for the L-flange model . . .	53
4.6	Simulation procedure for finding the migration location. . . . .	56
5.1	The force-displacement response in the SCB simulation . . . . .	60
5.2	The simulated key fracture events along the crack path in the SCB model	61

5.3	The predicted intralaminar crack path and the migration angle $\alpha$ in the SCB model. . . . .	61
5.4	Damage in the ply interface . . . . .	62
5.5	Force-displacement response for the mesh sensitivity study of the SCB model. . . . .	64
5.6	Interlaminar traction for different discretisations. . . . .	65
5.7	Energy shares in the SCB simulation . . . . .	66
5.8	The snap-back behaviour of the SCB model . . . . .	67
5.9	Force-displacement response for different viscosity parameter in the SCB model. . . . .	68
5.10	Viscous dissipated energy for different viscosity parameters. . . . .	69
5.11	Comparison of the force-displacement response with experiments for the SCB model. . . . .	71
5.12	The predicted migration location compared to the experiments in [33].	74
5.13	The predicted migration angle compared to the experiments in [33]. . .	74
5.14	The force-displacement response from the L-flange simulation. . . . .	76
5.15	The failed L-flange model and the predicted crack path. . . . .	77
5.16	Shear stress and damage at delamination migration for the L-flange model. . . . .	78
5.17	Comparison of the predicted force-displacement response to the experiments for the L-flange. . . . .	79
5.18	Force-displacement response for different interface properties. . . . .	81
5.19	Nodal shear stress and traction in the ply interface . . . . .	82

# List of Tables

4.1	Material properties for a unidirectional IM7/8552 carbon/epoxy laminate	52
4.2	Interface properties for the SCB model . . . . .	52
4.3	Material properties for a Cycom <sup>®</sup> 977-2-35%-12KHTA-134-300 carbon/epoxy unidirectional laminate . . . . .	54
4.4	Interface properties for the L-flange model . . . . .	54
5.1	Comparison of the different mesh sizes . . . . .	64
5.2	Comparison of the linear elastic stiffness in the simulations and the experiments in [33]. . . . .	70
5.3	Comparison of the maximum load in the simulation and the experiments in [33]. . . . .	72
5.4	Comparison of the potential energy in the simulation and the experiments in [33]. . . . .	73
5.5	Comparison of key parameters between simulation and experiments for the L-flange . . . . .	78
5.6	Location for delamination migration with different interface properties .	80
A.1	Force-displacement data from the experiments in [33] . . . . .	89
A.2	Experimental migration distance and crack angle from the SCB test in [33]. . . . .	90
B.1	Experimental force-displacement data extracted from the L-flange test.	91





# Chapter 1

## Introduction

Fiber-reinforced polymer (FRP) matrix composites provide unique material properties for lightweight structures that require high strength and stiffness. As the material configurations can be modified and customised to adequately meet the high standards of modern structural design, FRPs have become widely used in the aerospace, automotive and wind industries. A carbon fiber-reinforced polymer (CFRP) composite can have a tensile strength and elastic modulus comparable to steel, but with a density significantly lower than a conventional aluminium alloy. This makes the material attractive, not only for use in high-performance applications, but also in order to reduce emissions and energy consumption by building lighter and more efficient vehicles, air planes and modern transport solutions. Furthermore, the possibility of tailoring the fiber architecture in FRP structures enables the opportunity to develop durable components, specifically designed to withstand the exact loads that are exerted to them in their ultimate application.

For any engineering material, it is of great importance to understand the material behaviour and to be able to model and predict how and why a structure fails. In the case of FRPs, this is of particular interest since the material has a complex nature in terms of anisotropy and micro structure. A failure can be caused by high loads and large deformations. Moreover, local stress concentrations due to the heterogeneous micro structure, material imperfections and cracks may propagate and eventually lead to a catastrophic failure.

In order to deal with this, the development of numerical models that can predict the mechanical behaviour is essential. It leads to a better understanding of the material, thus appropriate design constraints for FRP components can be established. Furthermore, the earlier in the design process weaknesses and problems can be identified, the more time and cost efficient it is.

In the present work, a finite element modeling strategy is developed to simulate crack propagation in cross-ply FRPs. A continuum model is used as an idealisation of the constituent plies with homogeneous material properties. Inter- and intralaminar crack propagation is simulated by using cohesive zone models (CZM) and the extended finite element method (XFEM). The CZM enables progressive damage to be introduced to the material along a predefined crack path while XFEM has the capability of representing cracks with an arbitrary path. The models, which are created in the commercial finite element analysis (FEA) software *Abaqus/Standard 2017* (Dassault Systems Simulia Corp., Providence, RI, USA) are based on experimental tests from the literature. By introducing boundary conditions, material properties and loads accordingly, the performance and accuracy of the modeling strategy can be evaluated.

The first part of this thesis is an introduction to the materials and the failure mechanisms that are modeled. Two experimental tests from the literature are then introduced, which in the present work are used for comparison and to evaluate the results from the numerical models. Following this, the physical concepts of fracture mechanics and crack propagation through the CZM are presented in the theory section. Moreover, an XFEM formulation is given, which is capable of representing arbitrary propagating cracks in a discretised domain. In chapter 4, the practical application of the models in FEA is explained. A strategy for dealing with the limitations associated with the XFEM implementation in *Abaqus/Standard* is also presented. In the last part of the work the simulated results are evaluated, analysed and compared with the actual experiments from the literature.

## 1.1 Delamination migration in fiber-reinforced polymers

The material structure of FRPs consists of long continuous fibers that provide stiffness and strength. This is combined with a matrix material which distributes the load between the fibers. Due to the heterogeneous micro structure, a number of different failure mechanisms can be identified. Some of these are matrix cracking, fiber failure, fiber bridging and debonding between fiber and matrix. Additionally, delamination and buckling are common failure modes. The failure mechanisms can also be coupled and interact with each other, so that a delamination can propagate to trigger the initiation of a matrix crack. The fundamental concepts of fracture mechanics assume that a crack has a clearly defined shape and extends from a crack tip. When dealing

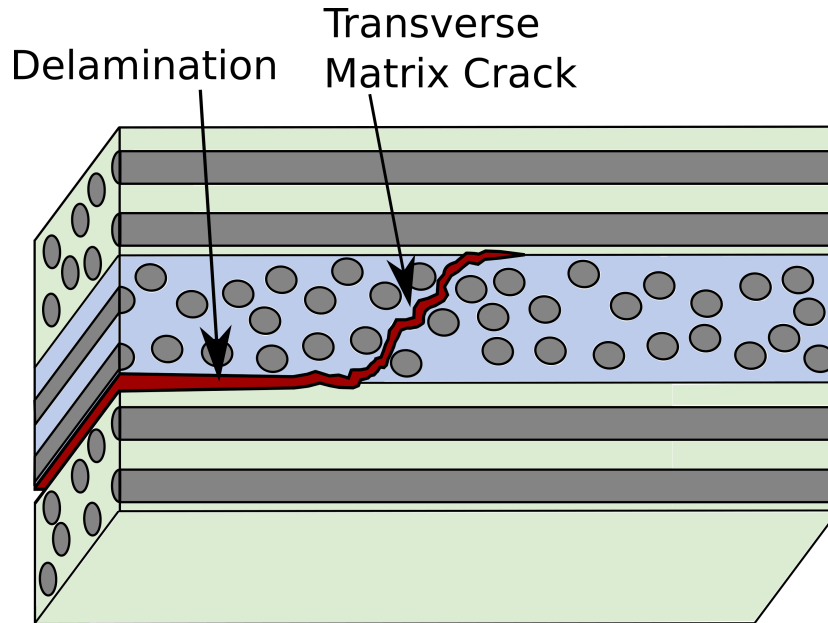


**Figure 1.1.** *Delamination migration by initiation of a transverse matrix crack in a cross-ply FRP.*

with FRPs, this is not always directly applicable due to the various failure modes and the fact that clusters of microscopic cracks often can be observed instead of one clearly defined crack front.

Two failure mechanisms and their interactions are simulated in the present work. These are inter-ply failure in form of interface cracks and intra-ply failure in the form of transverse matrix cracks.

Delamination can be defined as a crack located at the interface between two plies, separating the sub-laminates into two or more parts. It mainly occurs due to out-of-plane shear stresses, but also compressive load in the fiber direction and miss-match in the Poisson's ratio between two plies during loading can be the initial cause [2]. In contrast to most of the other failure mechanisms in FRPs, delamination propagates in a self-similar manner. Additionally, the strength and toughness of an interface is not necessarily as high as in the adjacent plies, which makes crack growth in this region very likely.

A Matrix crack is located in a ply or at a ply interface and propagates through the matrix material, which for a CFRP typically is an epoxy resin. The propagation of transverse matrix cracks is typically influenced by the presence of fibers in the neighbourhood of the crack tip. However, this interaction is not considered in the present work.

Delamination migration is the phenomenon where a delamination relocates from

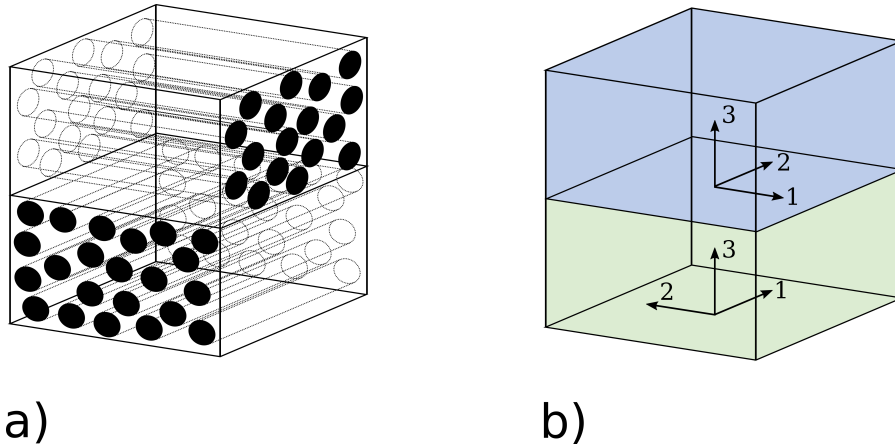


**Figure 1.2.** *A segment of a cross-ply FRP laminate lay-up consisting of two plies where a) is the actual composite configuration and b) is its homogeneous representation. The material properties are defined with respect to each local ply coordinate system.*

one ply interface to another. This can happen through interaction with matrix cracks, which is depicted in Fig. 1.1. The interface crack kinks into the adjacent ply and propagates in the transverse direction of the fibers. As modeling of delamination migration is the topic for this thesis, the interaction between these two failure mechanisms is studied in detail.

Homogenised material properties can be employed for the plies in a FRP laminate in order to make the modeling easier, which is shown in Fig. 1.2. This is done by assuming that the effective homogeneous elastic properties in one of the plies in Fig. 1.2 a) applies to the corresponding ply in Fig. 1.2 b), defined with respect to the local ply coordinate system. Due to this simplification, the modeling of the micro structure is avoided while maintaining sufficient mechanical properties of the ply.

The fibers in a laminate can be orientated in different directions relative to each other according to the stacking sequence and result in anisotropic stiffness properties. If only one of the constituent plies are considered and the homogenisation is made as in Fig. 1.2 b), the properties for a single ply can be assumed to be orthotropic. Furthermore, due to the isotropic properties in any direction perpendicular to the fibers, a single ply is assumed to be transversely isotropic. Hence, the normal to the isotropic plane is parallel to the direction of the fibers. This property is essential for the present work and makes it possible to simulate transverse crack propagation in an isotropic plane while assuming plane strain conditions.

## 1.2 Review of previous work on the topic

Due to the complex nature of FRPs and the various failure modes associated with them, the modeling of such materials has been the subject for extensive research. For simulating failure events in the form of propagating cracks, the finite element method (FEM) has been widely used. Different material models and discretisation schemes have been developed and applied with varying results. In order to evaluate the performance and accuracy, the numerical models are in general compared to actual experiments. Furthermore, additional factors such as computational expenses and the feasibility of the method for use in practice should always be considered.

Camanho and Dávila [8] used a "zero-thickness" decohesion element to simulate mixed-mode delamination propagation in CFRPs and found good agreement between simulations and experiments. The implemented decohesion element uses a cohesive traction-separation model with a damage initiation criterion based on the interlaminar stress, and a damage evolution defined by the critical strain energy release rate. The model does not only show good agreement with experimental results for extension of self-similar cracks, but the formulation also enables delamination propagation to be simulated without prior knowledge of the initial crack tip location.

*The stacked shell approach*, which uses shell elements to model the plies in FRPs and a cohesive surface-based contact formulation in the interfaces has been proposed as an alternative method [16]. In comparison to a regular continuum model, this approach showed good computational efficiency.

An engineering approach for dealing with the mesh dependency associated with the use of cohesive zone models was proposed by Camanho et al. [7], and provided further insight in how delamination can be modeled in a consistent way. Following this work, a sufficient element size in the cohesive zone can be estimated, leading to improvements for large-scale simulations and correct computation of the dissipated fracture energy. Additionally, a point-decohesion element has been proposed by Cui et al. [11] for simulating delamination in FRPs, which has the benefit of being easy to include in conventional FEM analyses and is based on a formulation of non-linear springs.

The advances of cohesive zone models have led to that this approach has become a standard solution for simulating delamination in FRPs in the recent years. Cohesive elements for various applications are also included in most commercial FEM software today, such as in *Abaqus/Standard*.

The XFEM was introduced by Belytschko [5] in 1999 and is based on the *partition of unity method* (PUM) [3], combining FEM with concepts from mesh-free

methods. By introducing enrichment functions to represent discontinuous features within the FEM framework, crack propagation can be modeled independent of the mesh topology [15]. Due to this, an arbitrary crack path can be predicted without the need for re-defining the mesh, and a coarser discretisation can be used, which potentially decreases the computational expenses. Moës et al. [30] also demonstrated the benefits of XFEM and calculated good numerical results for the stress intensity factor in stationary cracks.

As delamination migration includes two different failure modes in FRPs and their mutual interaction, a wide range of modeling approaches can be combined. *The stacked shell approach*, using cohesive elements in the ply interfaces and a *Hashin damage criterion* to account for propagation of the transverse matrix cracks showed promising results, although it could not capture all fracture events in detail [34]. In order to do this, different continuum-based approaches have been developed instead. *The floating node method* [12] was used successfully to simulate delamination migration in cross-ply laminates. It requires a floating node element to be implemented, which can model both material interface discontinuities and cracks within a single element. In the original implementation, propagation of delamination and transverse matrix cracks is determined through the *virtual crack closure technique* (VCCT), which requires the presence of an initial crack tip. The method showed good agreement with experimental results but is not available in any commercial FEA software. Some similar methods with capabilities of modeling intra-element discontinuities have been proposed, such as in the *augmented finite element method* [27,28] and *the extended cohesive damage model* (ECDM) [26].

An integrated approach using the XFEM and cohesive elements with enriched nodes was suggested by Hu et al. [21] for delamination migration in multi-directional FRPs. This requires the implementation of cohesive elements with additional degrees of freedom and adequate nodal enrichment functions. Furthermore, the XFEM was used by Zhao et al. [38] to simulate delamination migration in cross-ply FRPs, where both plies and interfaces are modeled with enriched XFEM elements. Combining this with a cohesive damage model and a crack-leading sub-routine to determine crack direction and initiation generated a good prediction of the migration location and the crack path.

Due to the efforts that have been made to model delamination migration by implementation of new elements, discretisation schemes and damage criteria, it is clearly not a trivial task to simulate it properly. In the present work, a modeling strategy is sought that does not require implementation of new subroutines or

elements, but combining two existing modeling approaches, the XFEM and the CZM. These two models are evidently working well separately and combining them can potentially result in an applicable simulation approach.

### 1.3 Scope of the present work

A numerical FEM modeling strategy is introduced in order to simulate the mechanical response and delamination migration in FRPs. By doing this, it cannot be expected that the model is able to fully represent all the physical events that occurs, since the crack propagation is partially dependent on the micro structure of the material, which is not considered. However, from an engineering point of view, it may be more relevant to be able to predict such fracture events on a larger scale. Thereby, more practical use can be gained with a less complex model, leading to decreased computational expenses, while avoiding the introduction of uncertainties in the form of material parameters that can be difficult to measure properly.

This leads to the main research question to be answered in the present work. Can delamination migration in cross-ply FRPs be simulated by using a homogeneous continuum model together with the XFEM and CZM? This general question can be rephrased and divided in to the specific sub-questions as follows:

- I. Can a modeling strategy within the frame work of *Abaqus/Standard* be developed for simulating delamination migration with sufficient precision?
- II. Can the interaction between inter- and intralaminar crack propagation be simulated by the proposed model?
- III. Can the structural response of a cross-ply FRP structure be adequately represented?
- IV. Can the fracture events in terms of crack length, crack direction and location of delamination migration be predicted by the model?





# Chapter 2

## Experiments from the literature

The numerical simulations in the present work are compared to physical experiments in order to evaluate the predictive capabilities and the performance of the models. The experiments can be found in detail in their original literature, and they are here presented as an introduction to delamination migration and the problem in general. Furthermore, the actual test configurations are explained in terms of specimen geometries, stacking sequences and load introduction. The results from the experiments are presented separately together with the results from the simulations in chapter 5. Additionally, some of the mechanical concepts which are briefly mentioned here in order to describe the experiments are further discussed in the theory section.

### 2.1 Delamination migration in a single cantilever beam

A benchmark test with the aim of experimentally investigating delamination migration in carbon/epoxy cross-ply laminates has been developed by Ratcliffe et al. [33], which in this work is referred to as the single cantilever beam (SCB) test. The results from this experiment have previously been used as a benchmark test for various numerical simulations of delamination migration [12,26,38]. It is a test where the fracture events happen in a sequential order without excessive interference from external factors.

The test is designed in such way that the combination of the stacking sequence in the laminate, the load introduction point and the initial crack location together promote delamination growth, followed by a single migration event. The delamination propagates in the  $0^\circ$ -direction of a  $0^\circ/90^\circ$ -interface between two plies. At some location, the interface crack migrates to another  $90^\circ/0^\circ$ -interface by kinking into the

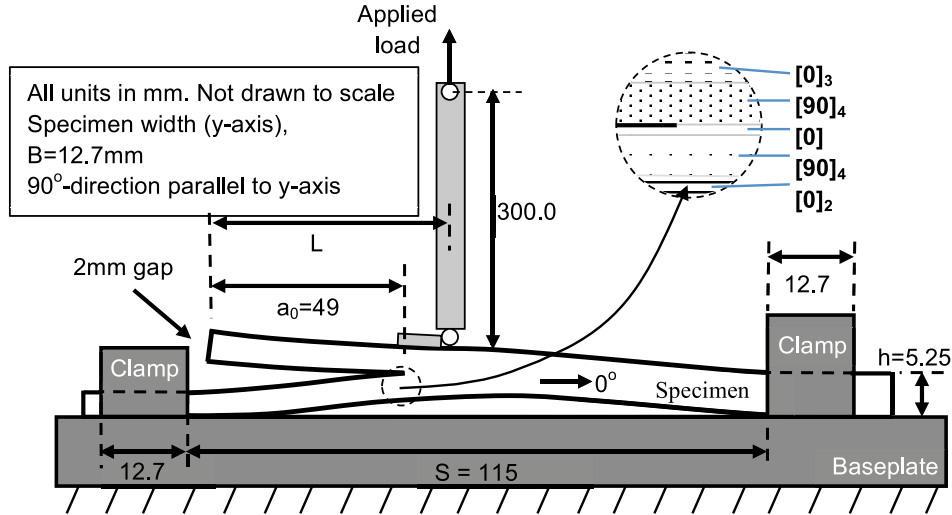


**Figure 2.1.** Specimen configuration and load introduction in the SCB test [33].

90°-plies and initiating a transverse matrix crack. As the matrix crack reaches the second 90°/0°-interface, a new interface crack forms. With the specimen configuration in the test, the loading mode of the first interface crack gradually changes as the crack propagates. By starting with a mixed mode configuration and reaching a point where mode II starts to dominate, kinking of the interface crack is possible and migration of the delamination to another interface is expected. In the experimental tests conducted in [33], the specimen material is a IM7/8552 carbon/epoxy cross-ply tape laminate, consisting of 44 plies with the stacking sequence

$$\underbrace{[90_4/0_3/(90/0)_{2s}/0_3/90_4/PTFE/0/90_4/0/0/(90/0)_{2s}/0/0/90_3/0/90]}_{\text{Ply } 1 \rightarrow 44}$$

The stacking sequence from left to right represents top to bottom in the set-up depicted in Fig. 2.1. A polytetrafluoroethylene (PTFE) insert is placed between ply 22 and 23, partially over the laminate length to create an initial delamination front called a pre-crack. The manufacturing process of the specimen in the experimental test included a standard vacuum infusion and curing in a hot press oven at approximately 180°C(350°F) [10]. The specimen is placed in a fixture and the test configuration can be seen in Fig. 2.1. The whole set-up is mounted on a steel base plate which is fixed. The laminate is clamped on top of the base plate, leaving a span of free laminate length between the clamps of  $S = 115$  mm. The specimen has a rectangular cross section with the width  $B = 12.7$  mm and the total thickness  $h = 5.25$  mm, which results in a ply thickness of approximately 0.12 mm. The PTFE insert is placed over

the length  $a_0 = 49$  mm measured from the left clamp, which is the initially pre-cracked length for all load configurations. On top of the specimen, a piano hinge is attached, connected to a 300 mm long rod, which is hinged at both ends and attached to the loading head from which the load is applied. The load introduction point at a distance  $L$  from the left clamp is the variable in the experiment. In [33], four different cases were tested for  $L = a_0$ ,  $L = 1.1a_0$ ,  $L = 1.2a_0$  and  $L = 1.3a_0$ . For each load case, 3-4 samples were tested in order to minimize the influence of deviating specimens.

At the initial state of the test, the structure is completely unloaded. Subsequently, the displacement-controlled load is introduced with a rate of 0.127 mm/min, and the force and the displacement is recorded at the load application point. During loading of the laminate, a series of events happen in the following order:

1. The specimen is loaded without any crack growth up to a critical limit, resulting in a linear structural response. This can be seen in Fig. 2.2.
2. Stable delamination starts to grow and propagates along the first  $0^\circ/90^\circ$ -interface between ply 22 and 23, starting from the tip of the PTFE insert as indicated in Fig. 2.3 a).
3. The delamination reaches a distance  $L$  from the left clamp, which is also the horizontal position of the load introduction to the structure. Unstable delamination takes place and the direction of the shear stress reverses ahead of the crack tip as can be seen in Fig. 2.3 b). The mode of the interface crack gradually changes to be more mode II-dominated which promotes the crack to kink in to the layers of  $90^\circ$ -plies.
4. The crack changes its propagating direction from growing in the first  $0^\circ/90^\circ$ -interface between ply 22 and 23 and kinks in to the  $90^\circ$  ply stack as seen in Fig. 2.3 b). The crack continues through all the four  $90^\circ$ -plies.
5. The ply crack reaches the second  $90^\circ/0^\circ$ -interface between ply 18 and 19 and initiates delamination in this interface.

It should be stated that for the case where  $L = a_0$ , the initial delamination front is located directly underneath the load introduction point, hence it starts in a mode I-dominated loading. Unstable delamination starts directly and the force-displacement response is slightly different in the experimental test in [33] for this case. However, the migration events take place in the same order as described above in point 3-5. In the other load cases, the delamination starts in a mixed mode loading and is

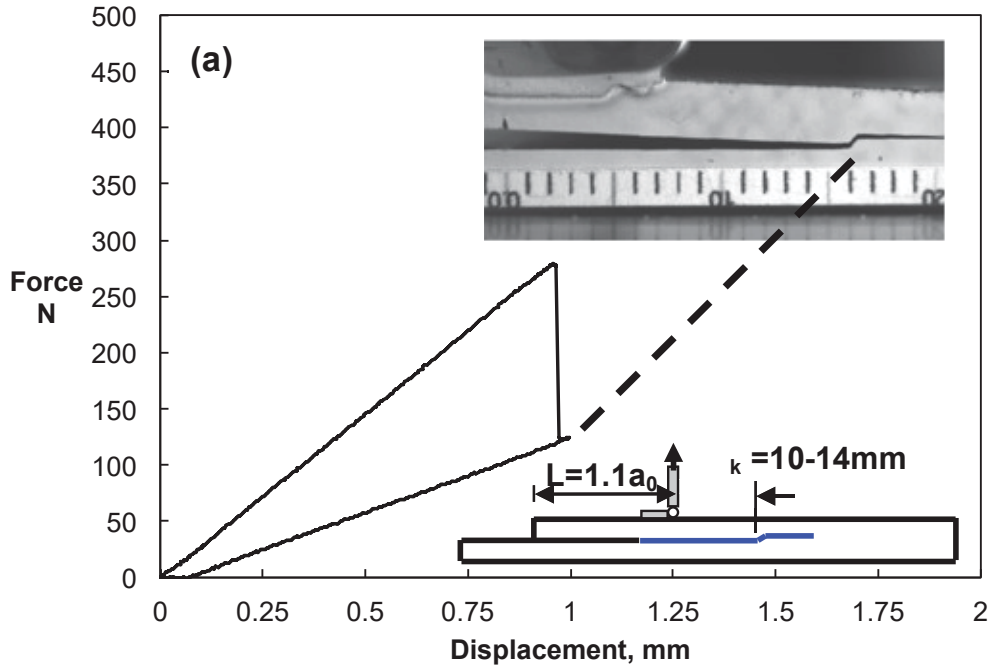


**Figure 2.2.** Force-displacement response of a specimen in the SCB test in [33] with the configuration  $L = 1.1a_0$ .

mode I-dominated as the interface crack propagates directly underneath the load application point [33]. Apart from recording the force-displacement of the structural response during the test, the delamination length at migration and the kink angle of the transverse matrix crack can be measured. A picture of the interface crack and the migration event can be seen in Fig. 2.4. The fracture surfaces from the experiments in [33] were examined in a scanning electron microscope to gain more detailed information about the mode of fracture at different stages. The results from this test are presented together with the simulated results in the present work for comparison in chapter 5.

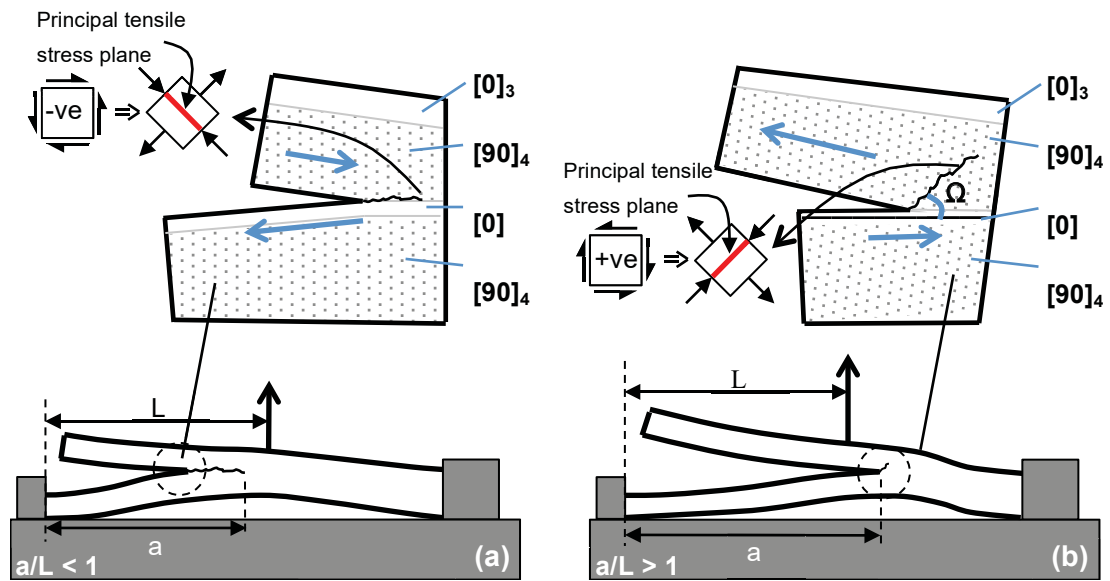


**Figure 2.3.** Delamination and formation of a transverse matrix crack for a loaded specimen in the SCB test [33].

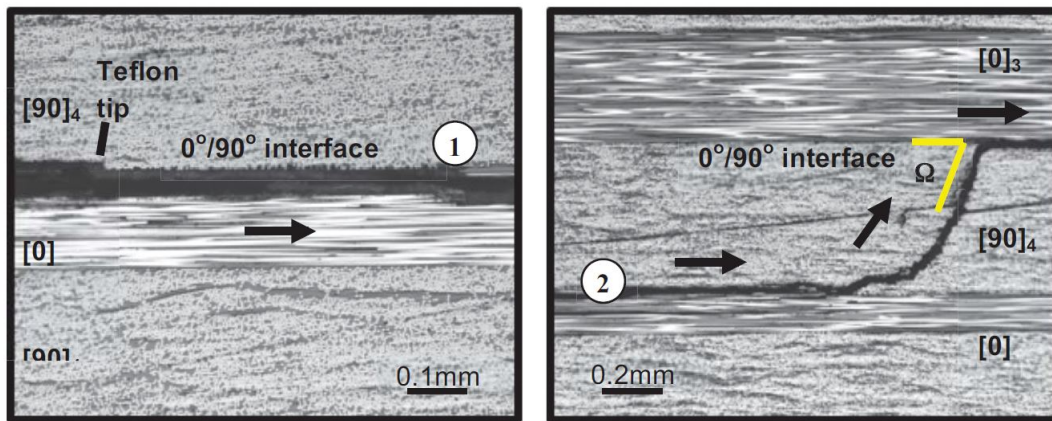


**Figure 2.4.** A detailed picture of an actual specimen from the SCB test in [33] where the PTFE-insert (Teflon) at the tip of the pre-cracked delamination front (left) and the delamination migration event (right) can be observed.

## 2.2 Delamination migration in a curved laminate

An experimental test of delamination in a curved cross-ply laminate has been conducted by Wimmer [37], which in the present work is referred to as the L-flange test. This test involves initiation of delamination in a pristine undamaged structure, where the interface crack eventually migrates from one interface to another. In contrast to the SCB test, the size and location of the delamination is not known a priori. Furthermore, an undamaged structure may be subjected to a higher load than one with an existing pre-crack, leading to relatively high strain energy in the system before emergence of cracks, which potentially can result in very unstable fracture events. Also the curved geometry of the specimen can be a challenge when simulating the test with a numerical model. This experiment is selected as a complement to the SCB test, and the numerical models can thereby be further evaluated.

The geometry and dimensions of the L-shaped specimen and the loading device used in the experiments in [37] are shown in Fig. 2.5.

The structure of the L-shaped cross-ply laminate is built up by plies of a *Cycom*<sup>®</sup> 977-2-35%-12KHTA-134-300 unidirectional carbon/epoxy composite with the stacking sequence

$$[0_3/90_3/0_3/90_3/0_3]_s.$$

The specimen has a rectangular cross section with the width  $B = 30$  mm and a total thickness of 3.75 mm, which corresponds to a ply-thickness of 0.125 mm. The vertical leg of the L-flange is clamped to the fixed steel loading device. The upper part of the loading device on the left side of the vertical leg gives the laminate additional support up to where the curved part begins.

On the horizontal part of the L-flange, a loading block is glued on to the lower side of the specimen. The loading block is connected through a cylindrical joint at the point C to the loading head of a hydraulic testing machine, which introduces a vertical displacement in the positive Y-direction at a rate of 2 mm/min. In the present work, only the case with an initially undamaged laminate is considered, even though tests with an initial interface crack also are carried out in [37]. The following events occur during the test, starting from an initially unloaded state:

1. The L-flange is loaded up to a critical limit without crack growth, resulting in a linear structural response while the interlaminar stress increases.
2. At a critical force, delamination initiates in the  $0^\circ/90^\circ$ -interface in the curved part of the laminate between ply 9 and 10, counted from the inner to the outer

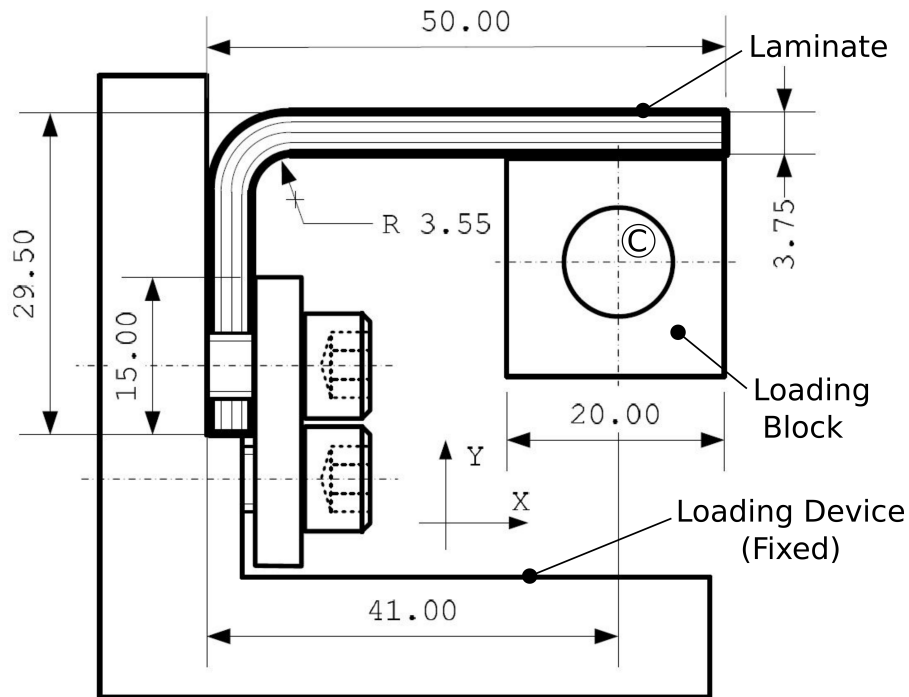


**Figure 2.5.** *The experimental test set-up for the curved L-flange laminate in [37]*

radius.

3. An unstable fracture event takes place when the delamination propagates and the applied load rapidly decreases.
4. The delamination migrates to the  $90^\circ/0^\circ$ -interface between ply 12 and 13 by forming a transverse matrix crack through ply 10-12, which are orientated in the  $90^\circ$ -direction.
5. As the transverse matrix crack reaches the  $90^\circ/0^\circ$ -interface between ply 12 and 13, delamination is initiated and continues to propagate in this interface.

The vertical force and the displacement is recorded at the load introduction point. The results from the experiments in [37] are presented in chapter 5 for comparison with the numerical simulations. As kinking of the interface crack was not the scope of this test, no exact measurements of migration location and kink angle exist. A picture of the resulting failed structure can be seen in Fig. 2.6 where the delamination starts somewhere in the middle of the curved part, followed by migration through the plies to the next interface.

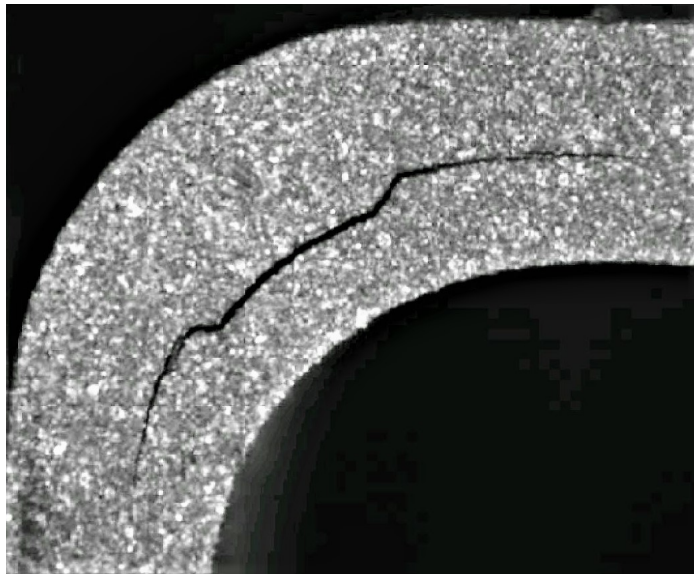


**Figure 2.6.** *A migrated interface crack in a specimen from the L-flange test in [37].*



# Chapter 3

## Theory

The purpose of this chapter is to introduce the theory on which the numerical models in the present work are based. It covers concepts of fracture mechanics, progressive damage modeling for crack propagation and the XFEM formulation. As the respective topics are quite extensive, the focus is on the parts which are relevant for modeling inter- and intralaminar cracks in FRPs. Hence, the physics, assumptions and constitutive models that are applied in the method in chapter 4 are introduced here.

### 3.1 Fracture mechanics

The field of fracture mechanics aims to describe and model how cracks effect the strength and behaviour of solid structures. A crack cannot adequately be described within the classic strength of material models but could propagate and cause a severe structural failure in form of a fracture. A lot of different models have been developed in order to capture these phenomena and to predict under which conditions the structure is going to fail.

For the present work where FRPs are considered, an overview is here given for the fracture models that can be used to predict their failure. The parameters and equations presented in this section lay the foundation for how cracks can be represented in an XFEM discretisation. The propagation of cracks is described through the CZM presented in section 3.2.

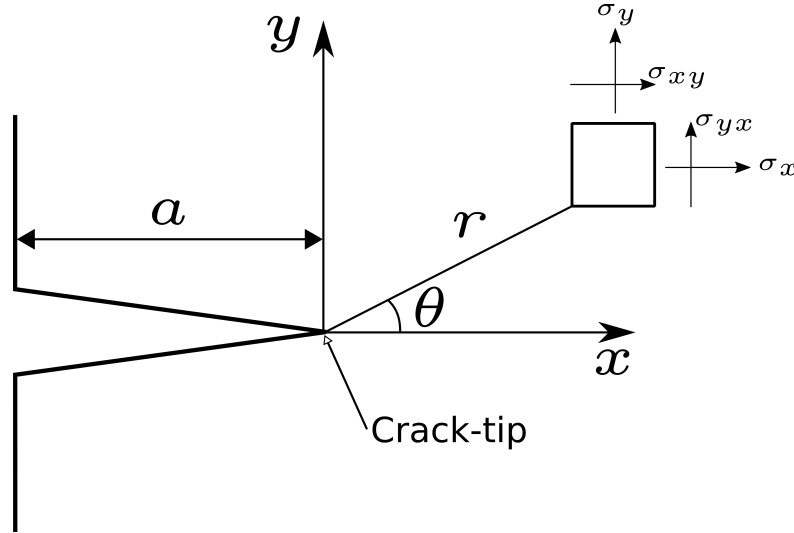


**Figure 3.1.** The local cylindrical coordinate system  $(r, \theta)$  with origin at the crack tip.

### 3.1.1 Linear elastic fracture mechanics

Linear elastic fracture mechanics (LEFM) is valid for brittle linear elastic materials where only small-scale yielding appears. Analytical solutions to the fracture problem have been developed by Westergaard [36] and Irwin [22]. An expression for the stress field that occurs in a linear elastic isotropic body with an infinitely sharp crack can be written as

$$\sigma_{ij} = \left( \frac{k}{\sqrt{r}} \right) f_{ij}(\theta) + \text{H.O.T.} \quad (3.1.1)$$

where  $\sigma_{ij}$  are the components in the *Cauchy stress tensor*,  $k$  is a constant and  $f_{ij}$  is a dimensionless trigonometric function of  $\theta$  [2]. The definition of  $r$  and  $\theta$  can be seen in Fig. 3.1. The higher order terms in Eq. (3.1.1) depends on the geometry and are finite or close to zero as  $r \rightarrow 0$  close to the crack tip, where the first term approaches infinity. The asymptotic stress function has a singularity at  $r = 0$ , and if only the singularity dominated zone close to the crack tip is considered, the equation can be approximated to

$$\lim_{r \rightarrow 0} \sigma_{ij} = \frac{K}{\sqrt{2\pi r}} f_{ij}(\theta) \quad (3.1.2)$$

where the stress intensity factor

$$K = Y\sigma\sqrt{a\pi} \quad (3.1.3)$$

and  $\sigma$  is the far-field stress. The crack length is  $a$  and  $Y$  depends on the geometry and mode of loading. An expression for the stress intensity factor can be derived

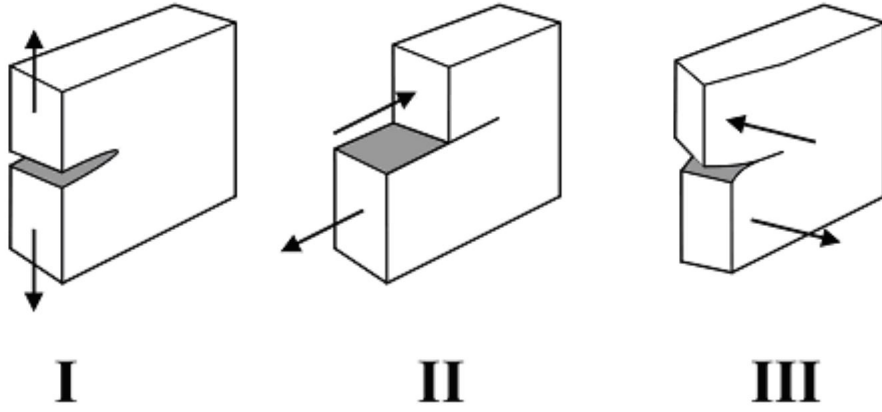


**Figure 3.2.** *The three modes for loading of a crack [9].*

analytically in some special cases. Furthermore, all crack configurations consist of one or a combination of three different fracture modes, which can be seen in Fig. 3.2 [2]. The stress intensity factors are written  $K_I$ ,  $K_{II}$  and  $K_{III}$  respectively, and the stress fields caused by each mode separately can be added together by using the superposition principle to obtain the mixed mode stress field for any crack.

While the stress and strain field has a singularity at the crack tip, the displacement field is a fully defined function and of great importance when incorporating LEFM in a FEM analysis. By solving for the displacements when a crack is loaded in mixed mode I and mode II in a plane deformation state

$$\begin{aligned}
 u_x(r, \theta) = & \frac{K_I}{2G} \sqrt{\frac{r}{2G}} \cos\left(\frac{\theta}{2}\right) \left[ \kappa - 1 + 2\sin^2\left(\frac{\theta}{2}\right) \right] \\
 & + \frac{K_{II}}{2G} \sqrt{\frac{r}{2G}} \sin\left(\frac{\theta}{2}\right) \left[ \kappa + 1 + 2\cos^2\left(\frac{\theta}{2}\right) \right]
 \end{aligned} \tag{3.1.4}$$

and

$$\begin{aligned}
 u_y(r, \theta) = & \frac{K_I}{2G} \sqrt{\frac{r}{2G}} \sin\left(\frac{\theta}{2}\right) \left[ \kappa + 1 - 2\cos^2\left(\frac{\theta}{2}\right) \right] \\
 & - \frac{K_{II}}{2G} \sqrt{\frac{r}{2G}} \cos\left(\frac{\theta}{2}\right) \left[ \kappa - 1 - 2\sin^2\left(\frac{\theta}{2}\right) \right]
 \end{aligned} \tag{3.1.5}$$

is obtained where  $\kappa$  is the *Kolosov* constant defined as

$$\kappa = \begin{cases} 3 - 4\nu, & \text{plane strain} \\ \frac{3 - \nu}{1 + \nu}, & \text{plane stress} \end{cases} \quad (3.1.6)$$

with  $\nu$  being the *Poisson's* ratio,  $G$  the shear modulus and  $u_x$  and  $u_y$  the horizontal and vertical displacements respectively [2].

The stress intensity factor can be used to evaluate some fracture criteria, thus a mode I-crack propagates when  $K_I = K_{Ic}$ .  $K_{Ic}$  is the fracture toughness for pure mode I-loading of the crack, and this material constant can be seen as the resistance to crack growth. As  $K$  is a local parameter to every single crack, it is preferable to have a global measurement of the fracture toughness that easier can be used in practice when the external loads of a system are known. Based on the *first law of thermodynamics*, the energy balance for incremental crack growth under equilibrium conditions has been formulated by Griffith [18] as

$$\frac{dE_{\text{tot}}}{d\mathcal{A}} = \frac{d\Pi}{d\mathcal{A}} + \frac{dW_s}{d\mathcal{A}} = 0 \quad (3.1.7)$$

where  $E_{\text{tot}}$  is the total energy,  $\Pi$  is the potential energy and  $W_s$  the work that is required for breaking the atomic bonds in the material, and thereby create the new incremental crack surface area  $d\mathcal{A}$ . The idea behind this formulation is that the energy dissipated in the system when the crack extends is equal to the decrease in potential energy, supplied by the potential of internal strain energy and the external forces. Hence, the total energy of the system remains constant. Based on this, an expression for the energy release rate,  $\mathcal{G}$  can be stated as

$$\mathcal{G} = -\frac{d\Pi}{d\mathcal{A}}. \quad (3.1.8)$$

The energy release rate reaches a critical value similar to the case of the stress intensity factor, so that from Eq. (3.1.7), the critical energy release rate can be defined as

$$\mathcal{G}_c = \frac{dW_s}{d\mathcal{A}} = 2w_f. \quad (3.1.9)$$

The fracture energy  $w_f$  can include both the free surface energy required to create new surfaces as well as plastic and viscoelastic effects. As a result of the basic assumptions in LEFM, where the material is linear elastic and only small-scale yielding occurs,

the fracture energy  $w_f$  is constant. The small-scale yielding can be approximated by adding a correction factor in the model [2]. For materials where non-linear effects occur, such as plasticity and large-scale yielding, other models must be applied. In the present work, this is done by introducing the CZM. Thereby, the assumption of small scale yielding in the vicinity of the crack tip can be replaced by an assumption of a slender cohesive process zone ahead of the crack tip. Some of the non-linear effects related to crack propagation in FRPs can thereby be incorporated in the model.

### 3.1.2 Mixed mode fracture criterion

When a crack is under mixed mode loading, the mode mixity can change as the crack propagates. This is especially true for delamination, which is bound to propagate along the interface path. It makes it necessary to employ a robust fracture criterion that can take different combinations of fracture modes in to account. For mixed mode loading of delamination in unidirectional FRPs, a semi-empirical fracture criterion based on the energy release rate has been derived by Benzeggagh and Kenane [6] as

$$\mathcal{G}_c^{\text{BK}} = \mathcal{G}_{\text{Ic}} + (\mathcal{G}_{\text{IIc}} - \mathcal{G}_{\text{Ic}}) \left( \frac{\mathcal{G}_{\text{shear}}}{\mathcal{G}_{\text{T}}} \right)^\eta \quad (3.1.10)$$

where

$$\begin{cases} \mathcal{G}_{\text{shear}} = \mathcal{G}_{\text{II}} + \mathcal{G}_{\text{III}} \\ \mathcal{G}_{\text{T}} = \mathcal{G}_{\text{I}} + \mathcal{G}_{\text{II}} + \mathcal{G}_{\text{III}} \end{cases} \quad (3.1.11)$$

for a combination of mode I,II and III, and

$$\begin{cases} \mathcal{G}_{\text{shear}} = \mathcal{G}_{\text{II}} \\ \mathcal{G}_{\text{T}} = \mathcal{G}_{\text{I}} + \mathcal{G}_{\text{II}} \end{cases} \quad (3.1.12)$$

for a combination of only mode I and II. The parameter  $\eta$  depends on the material and has to be determined experimentally. This criterion was originally developed in [6] for mixed mode delamination in fiber glass/epoxy composites and is generally considered to be a sufficient representation of the effective fracture energy. It is a straight-forward criterion and has previously been applied successfully together with various numerical models [8, 12, 38]. In the present work, it is employed in all crack models.

### 3.1.3 Kinking of cracks in isotropic materials and bi-material interfaces

For a crack under mixed mode loading, the direction in which it will propagate is of great interest. Yet, the kinking mechanism is not fully understood, even though different criteria have been developed to describe it. Some of the challenges with modeling this is how to deal with anisotropic materials, branching of cracks, plasticity and interaction with discontinuities. However, based on the *minimum strain energy density criterion*, the crack always extends in the direction which is the most energetically favourable, meaning that the energy required to extend is minimised [35]. For use in practice together with numerical models, this is generally hard to incorporate, hence other methods to determine the direction of the crack extension have been developed. In the present work, two different situations occur where the direction of the crack extension changes. One is when a crack propagates in an isotropic material, such as in the transversely isotropic plane of a unidirectional FRP with homogenised material properties. The other situation is when a crack propagates in a bi-material interface and branches or kinks out of the interface into one of the adjacent plies. The latter one is the interaction between delamination and transverse ply cracking, where a crack kinks out of, or into a material interface.

For isotropic materials, a common assumption can be made that the crack locally extends in the direction perpendicular to the maximum principal stress [14]. This can easily be calculated for any stress state by computing the eigenvectors to the Cauchy stress tensor. As the eigenvectors define the principle directions, the direction of the crack propagation can be determined from solving the characteristic equation

$$\det(\mathbf{S} - \sigma \mathbf{I}) = 0 \quad (3.1.13)$$

where the solutions are the principle stresses  $\sigma_1 > \sigma_2 > \sigma_3$  and  $\mathbf{S}$  is the Cauchy stress tensor. The surface(3D) or line(2D) has to be found that is perpendicular to the eigenvector  $\mathbf{s}_1$ , which corresponds to the maximum principal stress  $\sigma_1$ . It is defined from the equation

$$(\mathbf{S} - \sigma_1 \mathbf{I})\mathbf{s}_1 = \mathbf{0}. \quad (3.1.14)$$

It follows from this assumption that a crack in an isotropic material always extends in a direction corresponding to mode I loading. The problem with this approach is that the stress state has to be evaluated very close to the crack tip and that this continuum-based kink criterion thereby can be inaccurate for a discretised domain

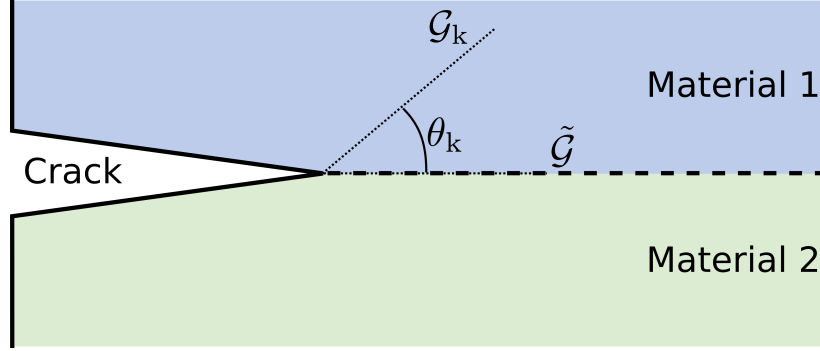


**Figure 3.3.** *The potential for a crack to kink out of a bi-material interface with the critical angle  $\theta_k$ , for which the strain energy release rate in material 1 has its maximum  $\mathcal{G}_k$ .*

with insufficient mesh resolution. Moreover, the presence of a process zone ahead of the crack tip can compromise the assumption that the crack propagates under pure mode I-loading in some numerical treatments of the problem.

For cracks that kink out of bi-material interfaces, the situation is more complicated if one of the materials is more compliant than the other, or if one of them is anisotropic. Based on that the crack always extends in the direction that is the most energetically favourable, a criterion based on the critical strain energy release rate has been developed by He and Hutchinson [19]. It states that a crack kinks out of an isotropic material interface when

$$\frac{\mathcal{G}_k}{\mathcal{G}_{Ic}} > \frac{\tilde{\mathcal{G}}}{\tilde{\mathcal{G}}_c}. \quad (3.1.15)$$

is satisfied. The strain energy release rate for extension of the crack in the direction defined by the angle  $\theta \neq 0$  has a maximum  $\mathcal{G}_k$  for the critical angle  $\theta_k$ . The kink angle is defined in Fig. 3.3.  $\tilde{\mathcal{G}}$  is the strain energy release rate of the interface between the two materials and  $\tilde{\mathcal{G}}_c$  its critical value. By comparing the ratios in Eq. (3.1.15), a readily comprehensive energy-based kink criterion is obtained. It is limited to interfaces between two dissimilar elastic isotropic materials. However, the general concept can still indicate under which conditions a crack kinks out of a bi-material interface also when one of the substrates is orthotropic, as is the present work.

## 3.2 Progressive damage modeling

In the present work, the propagation of cracks is simulated by using the CZM. This is an intuitive way of introducing material degradation prior to the extension of a

crack, and it has proven to be an applicable model for delamination in FRPs [8]. The CZM is based on the *Dugdale Model* [13] and assumes a process zone ahead of the propagating crack, which can be represented by a cohesive traction-separation law [4]. This requires a history dependent damage variable to be introduced at every material point in the process zone and affects the constitutive elastic stiffness.

### 3.2.1 Damage mechanics and stiffness degradation

In continuum damage mechanics, the degradation of a material due to the appearance of microscopic cracks and defects is described on a mesoscopic scale. For elastic materials, the effective stress due to the reduced load carrying capacity in an isotropically damaged zone can be modeled by introducing a monotonically increasing scalar damage variable  $d \in [0, 1]$ . The damage variable accounts for the reduced stiffness of the material as the damage progresses. The value  $d = 0$  corresponds to an undamaged state and  $d = 1$  a completely damaged state. The effective stress  $\hat{\sigma}$  can in a uniaxial stress state be defined as

$$\hat{\sigma} = \frac{\sigma}{1 - d} \quad (3.2.1)$$

where  $\sigma$  is the undamaged Cauchy stress. Based on the *hypothesis of strain equivalence*, the strains are equal in both states so that

$$\epsilon = \frac{\sigma}{E_d} = \frac{\hat{\sigma}}{E} \quad (3.2.2)$$

where  $E_d$  and  $E$  is the Young's modulus for the damaged and the undamaged state [25]. This leads to the formulation for the stress-strain relationship in a uniaxial stress state as

$$\sigma = E_d \epsilon = (1 - d)E\epsilon. \quad (3.2.3)$$

The formulation of the damage as a scalar is not applicable for anisotropic damage in 2D or 3D with a non-uniform distribution of micro defects. Hence, the general formulation, in which anisotropic damage can be accounted for has to be represented in tensor form. By introducing the fourth-order linear transformation tensor  $\mathbf{M} = \mathbf{M}(\Phi)$  called the damage effect tensor, dependent on the damage tensor  $\Phi$ , the effective stress can be written [31]

$$\hat{\sigma} = \mathbf{M}\sigma. \quad (3.2.4)$$



The elastic constants are given in the elasticity matrix  $\mathbf{D}$ , and when accounting for damage the matrix  $\mathbf{D}_d$  can be written as

$$\mathbf{D}_d = \mathbf{M}^{-1}\mathbf{D} \quad (3.2.5)$$

which results in the stress-strain relationship

$$\boldsymbol{\sigma} = \mathbf{D}_d\boldsymbol{\epsilon}. \quad (3.2.6)$$

### 3.2.2 The Dugdale model

The Dugdale model, also known as the strip yield model is the precursor to the CZM. It describes the plastic zone ahead of a physical crack tip as a slender segment in the tangent direction of the crack in a linear elastic-perfectly plastic material [13]. It is based on the principle of superposition for an equilibrium crack with the length  $2a + 2\rho$ , where a remote tension must be in balance with the closure stress acting in the strip yield plastic zone with the length  $\rho$ . The closure stress in the plastic zone is equal to the yield stress of the material  $\sigma_{YS}$ . A description of the crack representation according to the Dugdale model can be seen in Fig. 3.4.

For a certain length of the plastic zone in front of the physical crack tip, the stress intensity factor caused by the remote tension and the stress intensity factor caused by the closure stress cancel each other out, and the stress becomes finite.

As the leading term in the stress field function from Eq. (3.1.1) changes with  $1/\sqrt{r}$  close to the crack tip, it can be shown that the stress intensity factor due to the closure stress is

$$K_{\text{closure}} = -2\sigma_{YS}\sqrt{\frac{a+\rho}{\pi}}\cos^{-1}\left(\frac{a}{a+\rho}\right) \quad (3.2.7)$$

for a through crack in a plate with unit thickness and the closure stress acting over the length  $\rho$ , as seen in Fig. 3.4 b) [2]. In an infinite plate subjected to a remote tensile stress  $\sigma_\infty$ , the stress intensity factor for a through crack with the length  $2a + 2\rho$  is defined as  $K_\infty = \sigma_\infty\sqrt{\pi(a+\rho)}$ . The Dugdale model requires  $K_{\text{closure}} + K_\infty = 0$ , resulting in the expression

$$\frac{a}{a+\rho} = \cos\left(\frac{\pi\sigma_\infty}{2\sigma_{YS}}\right) \quad (3.2.8)$$

from which the estimated plastic zone length can be calculated for a given crack configuration.

The Dugdale model was originally developed to model plasticity in metal sheets [13], but it turns out that the model is more similar to the narrow bands

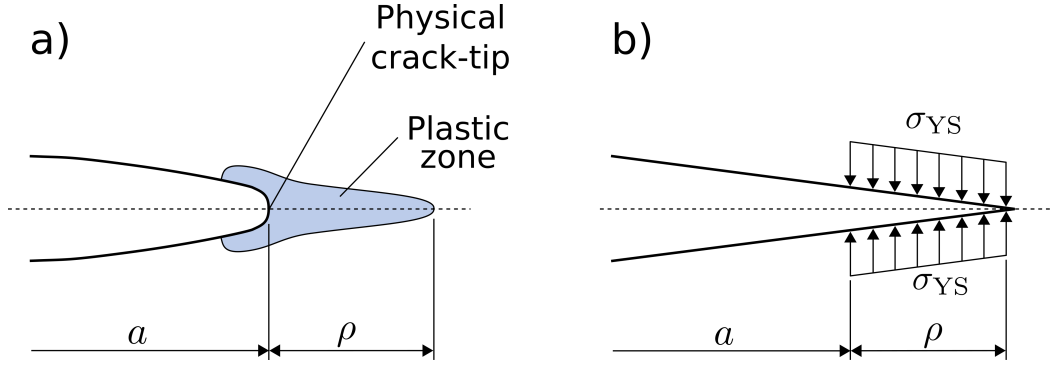


**Figure 3.4.** The representation of a crack with the length  $2a + 2\rho$  in the Dugdale model. The plastic zone with the length  $\rho$  in a) is represented by the fictitious crack tip in b), where the closure stress  $\sigma_{YS}$  is acting on the crack faces.

of crazing ahead of the crack tip in some polymers [2]. The model is presented here for the pure mode I-case but can be extended to also apply for mixed mode loading.

### 3.2.3 The cohesive traction-separation model

The description of the process zone ahead of the crack tip in the Dugdale model has been used by Barenblatt [4] to develop the CZM. The model is used to represent the non-linear effects which occur ahead of the crack tip in the cohesive process zone, and has been further developed and successfully applied in delamination simulations by Camanho and Dávila [8]. It combines a traction-separation formulation with progressive damage, where the damage is only considered in the slender cohesive segment in the tangent direction of the crack, referred to as a cohesive interface. The equation

$$\underbrace{\begin{bmatrix} t_n \\ t_s \\ t_t \end{bmatrix}}_{\mathbf{t}} = \underbrace{\begin{bmatrix} K_{nn} & 0 & 0 \\ 0 & K_{ss} & 0 \\ 0 & 0 & K_{tt} \end{bmatrix}}_{\mathbf{D}^{cz}} \underbrace{\begin{bmatrix} \delta_n \\ \delta_s \\ \delta_t \end{bmatrix}}_{\boldsymbol{\delta}} \quad (3.2.9)$$

relates the interface traction  $\mathbf{t}$  to the separation  $\boldsymbol{\delta}$  through the uncoupled interface stiffness matrix  $\mathbf{D}^{cz}$ . The indices  $n$ ,  $s$  and  $t$  stands for the normal, first- and second shear direction with respect to the cohesive interface, as indicated in Fig. 3.5.

A cohesive zone subjected to a single-mode loading can be modeled by the bi-linear traction-separation law shown in Fig. 3.6. The load response at any point located in the cohesive interface is elastic with the initial stiffness  $K_{ii}$  until the traction reaches the value for the maximum strength  $\hat{t}_i$  with the corresponding separation  $\delta_i^0$ . This value is typically the tensile- or shear strength for the material, and in the case for

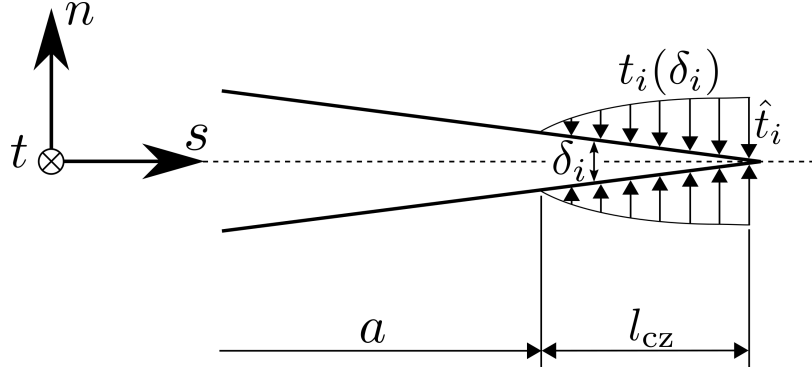


**Figure 3.5.** The cohesive zone model for single mode loading, depicted for the case where  $i = n$  with the distributed traction in the process zone  $t_i(\delta_i)$  and the opening separation  $\delta_i$ . The coordinate system  $(n, s, t)$  defines the normal, first- and second shear direction with respect to the crack plane.

delamination of FRPs, the interface strength. At this point, the damage variable  $d$  is introduced. As the interface is further loaded, the damage evolves and leads to proportional reduction of the stiffness to  $(1 - d)K_{ii}$ . If the interface is completely unloaded at a partially damaged state, it will be unloaded elastically so that  $\delta_i = 0$  and  $t_i = 0$ . Upon further loading, the response is again elastic with the reduced interface stiffness. The damage proceeds when the traction reaches the maximum strength for the current damage state, corresponding to the separation  $\delta_i^{\max}$ . Eventually, the failure separation  $\delta_i^{\max} = \delta_i^f$  is reached and the strength and stiffness in the cohesive interface is zero. The constitutive bi-linear traction-separation law for a single-mode loading can mathematically be described as

$$t_i = \begin{cases} K_{ii}\delta_i & \text{if } \delta_i^{\max} \leq \delta_i^0 \\ (1 - d)K_{ii}\delta_i & \text{if } \delta_i^0 < \delta_i^{\max} < \delta_i^f \\ 0 & \text{if } \delta_i^{\max} \geq \delta_i^f \end{cases} \quad (3.2.10)$$

and

$$d = \frac{\delta_i^f(\delta_i^{\max} - \delta_i^0)}{\delta_i^{\max}(\delta_i^f - \delta_i^0)} \quad \text{where } i = n, s, t \quad d \in [0, 1]. \quad (3.2.11)$$

In the present work, no damage is caused by compressive stress, which requires the additional condition

$$\delta_n^{\max} \geq 0 \quad (3.2.12)$$

to be fulfilled for loading in the normal direction [8]. The maximum separation  $\delta_i^{\max}$  is a state variable dependent on the loading history and is the separation corresponding

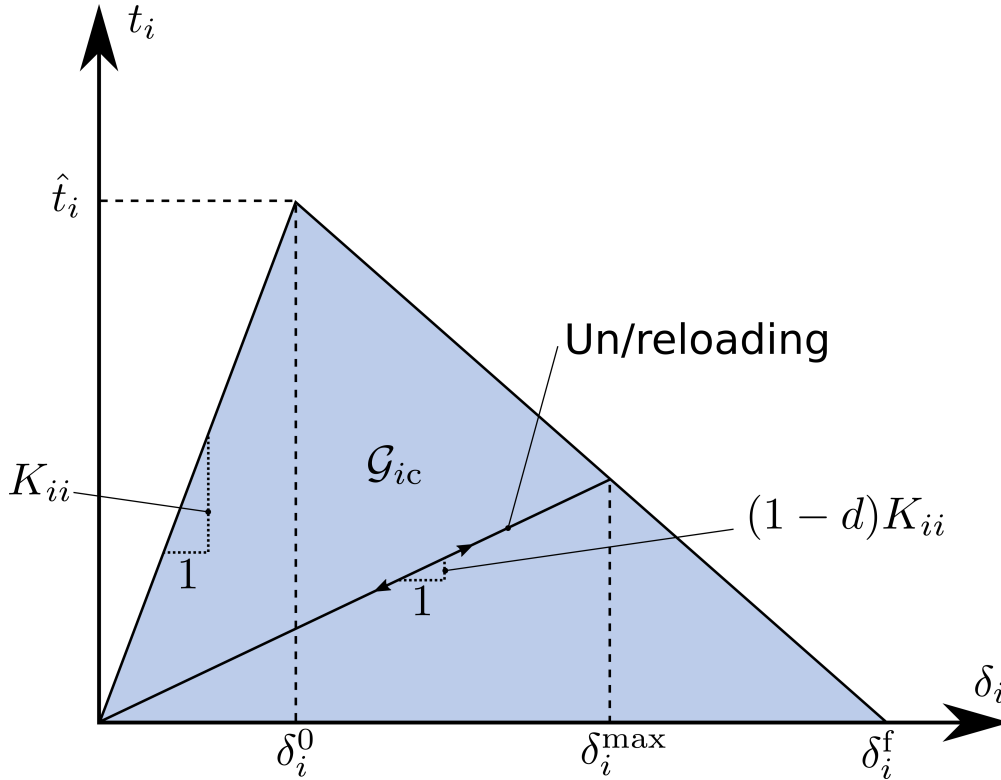


**Figure 3.6.** The constitutive bi-linear traction-separation model for single-mode loading of a cohesive zone where  $i=n,s,t$ .

to the maximum strength at the current damage state. It can be defined as

$$\delta_n^{\max} = \max \{ \delta_n^{\max}, \delta_n \} \quad (3.2.13)$$

for loading in mode I and

$$\delta_{i=s,t}^{\max} = \max \{ \delta_i^{\max}, |\delta_i| \} \quad (3.2.14)$$

for loading in mode II and III. To avoid interpenetration of the crack surfaces when using this model, the normal traction obeys

$$t_n = K_{nn}\delta_n \quad \text{if } \delta_n \leq 0. \quad (3.2.15)$$

When the propagation of a crack is modeled by using the traction-separation law, the critical strain energy release rate corresponding to complete decohesion can be interpreted as the "area under the graph", as seen in Fig. 3.6. In order to fulfil Griffith's fracture criterion in Eq. (3.1.7),  $\mathcal{G}_{ic}$  must be equal to the work done by the cohesive traction required to reach the failure separation across the interface. This

can be obtained through the integral

$$\mathcal{G}_{ic} = \int_0^{\delta_i^f} t_i d\delta_i. \quad (3.2.16)$$

### 3.2.4 The cohesive traction-separation model under mixed-mode loading

To be able to use the traction-separation model in practice, it is necessary to adapt it for mixed mode loading. In this section, a mixed-mode cohesive traction-separation model including damage initiation and damage evolution is presented.

The damage is initiated for single-mode loading when the traction reaches the value of the maximum strength. However, under mixed mode loading the damage can be initiated before any of the tractions in the respective direction has reached the maximum strength, and a criterion including the combined traction must be applied instead. A quadratic criterion is therefore introduced as

$$\left(\frac{\langle t_n \rangle}{\hat{t}_n}\right)^2 + \left(\frac{t_s}{\hat{t}_s}\right)^2 + \left(\frac{t_t}{\hat{t}_t}\right)^2 = 1 \quad (3.2.17)$$

where  $\langle \rangle$  is the *Macaulay operator* and prevents damage to be initiated due to compressive stress. The total mixed-mode separation  $\delta_m$  can be calculated as the magnitude of the resulting separation vector so that

$$\delta_m = \sqrt{\langle \delta_n \rangle^2 + \delta_s^2 + \delta_t^2} = \sqrt{\langle \delta_n \rangle^2 + \delta_{\text{shear}}^2}, \quad (3.2.18)$$

and the distinction is only made between normal- and shear separation. A failure criterion for mixed mode loading that includes mode III is hard to find, mainly because the lack of trustworthy test methods to provide verification [8]. Furthermore, it is generally difficult to measure the critical fracture energy for mode III experimentally for delamination in FRPs in a consistent and satisfying way. Following [8], both shear directions are here treated together so that  $\hat{t}_s = \hat{t}_t$  and  $\mathcal{G}_{\text{shear}} = \mathcal{G}_{\text{II}} + \mathcal{G}_{\text{III}}$ . In the present work, no fractures in mode III are simulated but in order to maintain a general approach when defining the model, mode III is included in this way. The initial undamaged stiffness in all directions is given the same value so that  $K = K_{ii}$  for  $i = n, s, t$ . The mode-mix ratio  $\beta$  can be defined as

$$\beta = \frac{\delta_{\text{shear}}}{\delta_n} \quad \text{for} \quad \delta_n > 0. \quad (3.2.19)$$

With the assumptions made above and by combining Eq. (3.2.17) to (3.2.19) the total separation at damage initiation can be defined as

$$\delta_m^0 = \begin{cases} \delta_n^0 \delta_s^0 \sqrt{\frac{1 + \beta^2}{(\delta_s^0)^2 + (\beta \delta_n^0)^2}} & \text{if } \delta_n > 0 \\ \delta_{\text{shear}} & \text{if } \delta_n \leq 0 \end{cases} \quad (3.2.20)$$

To determine the failure separation for mixed mode loading  $\delta_m^f$ , for which complete decohesion occurs, the mixed mode fracture criterion by Benzeggagh and Kenane in Eq. (3.1.10) is used in combination with the equations above. From this follows that

$$\delta_m^f = \begin{cases} \frac{2}{K \delta_m^0} \left[ \mathcal{G}_{\text{Ic}} + (\mathcal{G}_{\text{IIc}} - \mathcal{G}_{\text{Ic}}) \left( \frac{\beta^2}{1 + \beta^2} \right)^\eta \right] & \text{if } \delta_n > 0 \\ \sqrt{(\delta_s^f)^2 + (\delta_t^f)^2} & \text{if } \delta_n \leq 0. \end{cases} \quad (3.2.21)$$

The constitutive behaviour for the mixed-mode bi-linear traction-separation model can be defined by using the Kronecker delta property  $\bar{\delta}_{pq}$ , where the indices  $p$  and  $q$  relate to the matrix components  $D_{pq}^{\text{cz}}$  defined in Eq. (3.2.9). This results in

$$t_p = D_{pq}^{\text{cz}} \delta_q \quad (3.2.22)$$

where

$$D_{pq}^{\text{cz}} = \begin{cases} \bar{\delta}_{pq} K & \text{if } \delta_m^{\text{max}} \leq \delta_m^0 \\ \bar{\delta}_{pq} \left[ (1 - d) K + \bar{\delta}_{p1} K d \frac{\langle -\delta_n \rangle}{\delta_n} \right] & \text{if } \delta_m^0 < \delta_m^{\text{max}} < \delta_m^f \\ \bar{\delta}_{p1} \bar{\delta}_{1q} K \frac{\langle -\delta_n \rangle}{\delta_n} & \text{if } \delta_m^{\text{max}} \geq \delta_m^f \end{cases} \quad (3.2.23)$$

$$d = \frac{\delta_m^f (\delta_m^{\text{max}} - \delta_m^0)}{\delta_m^{\text{max}} (\delta_m^f - \delta_m^0)} \quad d \in [0, 1]. \quad (3.2.24)$$

with the state variable

$$\delta_m^{\text{max}} = \max \{ \delta_m^{\text{max}}, \delta_m \} \quad (3.2.25)$$

The bi-linear traction-separation model presented here is a standard approximation for the constitutive cohesive behaviour. With an appropriate damage initiation criterion such as in Eq. (3.2.17) and the fracture criterion in Eq. (3.1.10), the rest

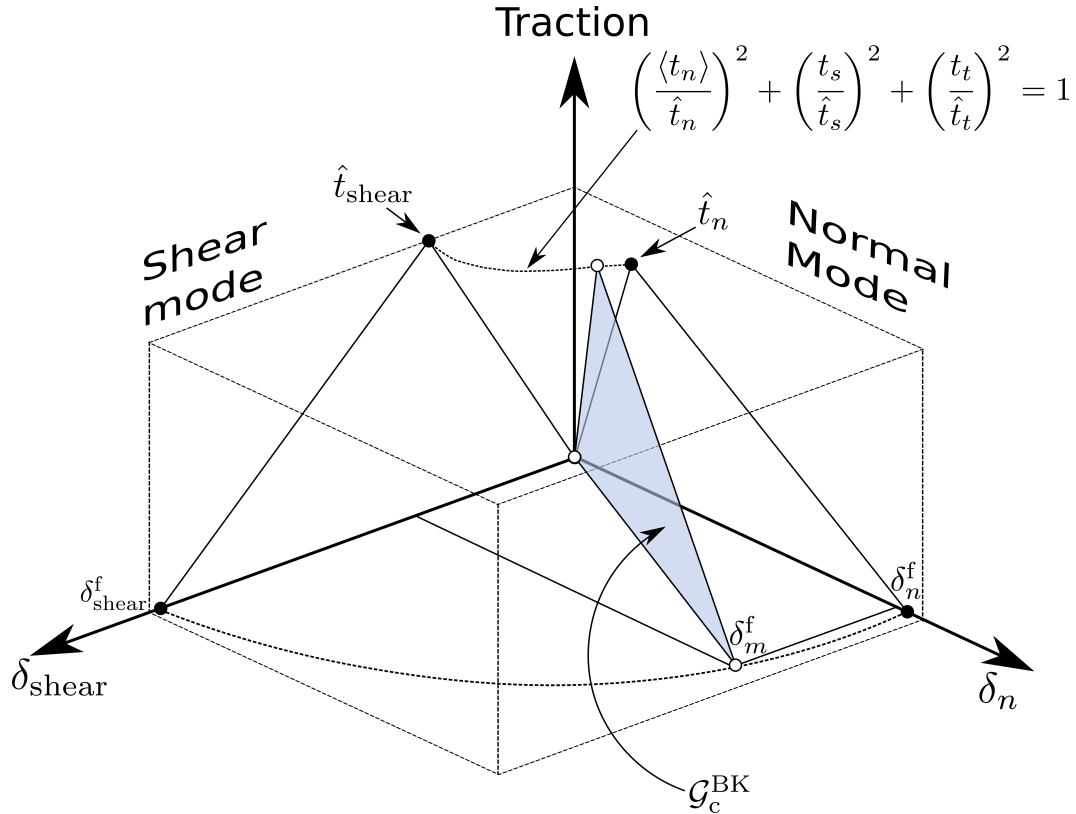


**Figure 3.7.** *The constitutive bi-linear traction-separation model for mixed-mode loading.*

of the model is simply defined through geometric relationships. This can be seen in Fig. 3.7 where the mixed mode traction-separation model is shown and the resulting response for a given mode mix is highlighted.

The traction-separation curve does not have to show the bi-linear shape which is presented here. Depending on the material and the type of fracture that is to be modeled, an exponential, tri-linear or parabolic softening shape of the curve can also be used, and the constitutive formulation slightly changes. As long as the cohesive zone is relatively small in comparison to the characteristic geometrical lengths, the model is in general considered to be valid [8]. In the present work, the bi-linear traction-separation law presented here is used exclusively.

### 3.3 XFEM formulation

XFEM is a PUM-based method and an extension of the standard FEM framework [3, 15]. The general concept of XFEM is to combine the continuum-based FEM with enrichment functions that describe a physical discontinuous behaviour. By doing so, the discontinuities can be treated relatively independent of the mesh topology, which is desirable for various numerical simulations in solid and fluid mechanics. Depending on the choice of enrichment function, the XFEM can represent both weak discontinuities, such as in interfaces between different materials, and strong discontinuities such as cracks [15]. For the application of simulating propagating cracks, the XFEM is of interest since an arbitrary crack path potentially can be predicted, which does not have to conform with the mesh [5]. Furthermore, the same mesh can be used throughout a simulation and redefinition of the mesh as the crack propagates is avoided. Hence this saves some computational expenses, which is of great importance in any kind of non-linear numerical simulation.

The purpose of the following sections is to briefly present the fundamental equations in the FEM formulation, which can be found more in detailed in [32]. Based on this, the concept, structure and system matrices in XFEM are defined, and it is demonstrated how the method can be applied to represent an arbitrary discretised crack.

#### 3.3.1 FEM – Strong and weak form

The finite element formulation is based on a virtual energy form of the equations of motion, also known as the weak form, and can be obtained directly from the strong formulation. For an arbitrary three-dimensional body in equilibrium, the strong form differential equation

$$\tilde{\nabla}^T \boldsymbol{\sigma} + \mathbf{b} = \mathbf{0} \quad (3.3.1)$$

is valid regardless of any constitutive behaviour [32]. The matrix differential operator  $\tilde{\nabla}^T$  is defined as

$$\tilde{\nabla}^T = \begin{bmatrix} \frac{\partial}{\partial x} & 0 & 0 & \frac{\partial}{\partial y} & \frac{\partial}{\partial z} & 0 \\ 0 & \frac{\partial}{\partial y} & 0 & \frac{\partial}{\partial x} & 0 & \frac{\partial}{\partial z} \\ 0 & 0 & \frac{\partial}{\partial z} & 0 & \frac{\partial}{\partial x} & \frac{\partial}{\partial y} \end{bmatrix}$$



the Cauchy stresses

$$\boldsymbol{\sigma} = \begin{bmatrix} \sigma_{xx} & \sigma_{yy} & \sigma_{zz} & \sigma_{xy} & \sigma_{xz} & \sigma_{yz} \end{bmatrix}^T$$

and the body-force vector

$$\mathbf{b} = \begin{bmatrix} b_x & b_y & b_z \end{bmatrix}^T.$$

A vector  $\mathbf{v}$ , containing the arbitrary weight functions is multiplied with Eq. (3.3.1). Integration over the volume and by using the *Green-Gauss theorem* yields the weak form of the differential equation of equilibrium

$$\int_V (\tilde{\nabla} \mathbf{v})^T \boldsymbol{\sigma} dV = \int_S \mathbf{v}^T \mathbf{t} dS + \int_V \mathbf{v}^T \mathbf{b} dV, \quad (3.3.2)$$

where  $V$  is the volume of the body,  $S$  is the surface defining the boundary of the body and  $\mathbf{t}$  is the traction vector acting on  $S$ . To derive the FEM equations for elasticity, the displacements  $\mathbf{u}$  in the body are approximated as

$$\mathbf{u} = \mathbf{N} \mathbf{a} \quad (3.3.3)$$

where  $\mathbf{a}$  is the nodal displacement vector in a discretised domain and  $\mathbf{N}$  is the global shape function matrix. By using the *Galerkin method*, the weight functions are chosen so that

$$\mathbf{v} = \mathbf{N} \mathbf{c} \quad (3.3.4)$$

with the arbitrary matrix  $\mathbf{c}$ . It follows that  $\tilde{\nabla} \mathbf{v} = \mathbf{B} \mathbf{c}$  where  $\mathbf{B} = \tilde{\nabla} \mathbf{N}$ . Inserted into the weak form in Eq. (3.3.2) and eliminating  $\mathbf{c}$ , the expression

$$\int_V \mathbf{B}^T \boldsymbol{\sigma} dV = \int_S \mathbf{N}^T \mathbf{t} dS + \int_V \mathbf{N}^T \mathbf{b} dV \quad (3.3.5)$$

is obtained [32]. If a thermoelastic material is considered with properties described by the constitutive matrix  $\mathbf{D}$ , the kinematic relation for the strains can be written  $\boldsymbol{\epsilon} = \tilde{\nabla} \mathbf{u}$ . The strain vector  $\boldsymbol{\epsilon}$  has the shear components  $\gamma_{ij}$  which per definition are related to the corresponding tensorial shear strain components  $E_{ij}$  so that  $2E_{ij} = \gamma_{ij}$ . The stresses can be written

$$\boldsymbol{\sigma} = \mathbf{D} \mathbf{B} \mathbf{a} - \mathbf{D} \boldsymbol{\epsilon}_0, \quad (3.3.6)$$

where  $\boldsymbol{\epsilon}_0$  are the known initial strains, typically due to a thermal load. Together with Eq. (3.3.5) this yields

$$\int_V \mathbf{B}^T \mathbf{D} \mathbf{B} dV \mathbf{a} = \int_S \mathbf{N}^T \mathbf{t} dS + \int_V \mathbf{N}^T \mathbf{b} dV + \int_V \mathbf{B}^T \mathbf{D} \boldsymbol{\epsilon}_0 dV. \quad (3.3.7)$$

From this equation, the system matrices for the standard FEM formulation

$$\mathbf{K} \mathbf{a} = \mathbf{f} \quad (3.3.8)$$

which is to be solved for  $\mathbf{a}$  are defined as

$$\mathbf{K} = \int_V \mathbf{B}^T \mathbf{D} \mathbf{B} dV \quad (3.3.9)$$

and

$$\mathbf{f} = \int_S \mathbf{N}^T \mathbf{t} dS + \int_V \mathbf{N}^T \mathbf{b} dV + \int_V \mathbf{B}^T \mathbf{D} \boldsymbol{\epsilon}_0 dV, \quad (3.3.10)$$

where  $\mathbf{K}$  is the stiffness matrix and  $\mathbf{f}$  is the force vector. Depending on the boundary conditions that apply to the problem, the first term on the right-hand side in Eq. (3.3.7) can be split in two parts to represent the essential and natural boundary conditions respectively. On the boundary  $S = S_h + S_g$ , the traction vector  $\mathbf{t}$  is known on  $S_h$  and the displacement vector  $\mathbf{u}$  is known on  $S_g$ . By using *Cauchy's stress formula* with the stress tensor  $\mathbf{S}$  and the unit vector  $\mathbf{n}$ , normal to the boundary surface  $S$ , it can be written that  $\mathbf{t} = \mathbf{S} \mathbf{n} = \mathbf{h}$  on  $S_h$  where  $\mathbf{h}$  is known. Hence, the force vector in Eq. (3.3.10) can be rewritten as

$$\mathbf{f} = \int_{S_h} \mathbf{N}^T \mathbf{h} dS + \int_{S_g} \mathbf{N}^T \mathbf{t} dS + \int_V \mathbf{N}^T \mathbf{b} dV + \int_V \mathbf{B}^T \mathbf{D} \boldsymbol{\epsilon}_0 dV, \quad (3.3.11)$$

to include appropriate boundary conditions in the formulation.

### 3.3.2 XFEM – Enrichment of the FEM formulation

The XFEM is based on the standard FEM formulation obtained in section 3.3.1. Additionally, some essential modifications are made to this formulation to be able to include discontinuities inside the elements. Based on some prior knowledge about the characteristics of the solution, a nodal enrichment is added to the elements in the part of the domain that may contain a discontinuity. This is done by introducing additional degrees of freedom to the nodes in these elements, which are included by using certain discontinuous enrichment functions. The enrichment functions are

specific for each type of physical problem and must be chosen with care in order to accurately represent a discontinuous feature in the FEM model. In the present work, strong discontinuities in the form of propagating cracks are modeled, hence the XFEM formulation is presented for this type of problem.

The nodal enrichment is added, starting from Eq. (3.3.3). In a domain  $\Omega$ , the approximated displacement function  $u^h(\mathbf{x}) \approx u(\mathbf{x})$  in the standard FEM formulation can be written

$$u^h(\mathbf{x}) = \sum_{i \in I} N_i(\mathbf{x}) a_i \quad (3.3.12)$$

where  $I$  is the set of all nodes in the domain,  $a_i$  are the degrees of freedom and  $\mathbf{x} \in \Omega$ . By introducing a nodal enrichment function to a subset of nodes  $I^* \subset I$  that contains the discontinuity, the approximation

$$u^h(\mathbf{x}) = \underbrace{\sum_{i \in I} N_i(\mathbf{x}) a_i}_{\text{Std. FEM approx.}} + \underbrace{\sum_{i \in I^*} N_i^*(\mathbf{x}) \psi(\mathbf{x}) b_i}_{\text{Enrichment}} \quad (3.3.13)$$

can be formulated [15]. The superscript  $*$  in the equations indicates that the quantity is related to the enriched part. The enrichment function is here given by  $\psi(\mathbf{x})$ ,  $b_i$  are the extra degrees of freedom in the enriched nodes and the shape function  $N_i^*(\mathbf{x})$  is associated with the enriched subdomain. As XFEM is based on partition of unity, an important property of  $N_i^*(\mathbf{x})$  is that

$$\sum_{i \in I} N_i^*(\mathbf{x}) = 1, \quad (3.3.14)$$

which is analogue to the standard FEM shape functions. It is common to define  $N_i^* = N_i$ , though this is not always the case. However, for simulation of propagating cracks in *Abaqus/Standard*, the same shape functions are used for enriched and non-enriched elements by default.

### 3.3.3 Definition of XFEM matrices

As a consequence of adding the enrichment term in Eq. (3.3.13), the XFEM formulation can be obtained by introducing the changes directly to the standard FEM formulation. The weak form of the equation of equilibrium in Eq. (3.3.5) still applies,

and leads to the two equations

$$\int_V \mathbf{B}^T \boldsymbol{\sigma} dV = \int_S \mathbf{N}^T \mathbf{t} dS + \int_V \mathbf{N}^T \mathbf{b} dV \quad (3.3.15)$$

$$\int_V \mathbf{B}^{*T} \boldsymbol{\sigma} dV = \int_S \mathbf{N}^{*T} \mathbf{t} dS + \int_V \mathbf{N}^{*T} \mathbf{b} dV, \quad (3.3.16)$$

which together must be fulfilled. Since the approximation  $\mathbf{u} = \mathbf{N}\mathbf{a} + \mathbf{N}^*\boldsymbol{\psi}\mathbf{a}^*$  will apply when the enriched part is included, the complete XFEM formulation is obtained through the same substitution made in Eq. (3.3.7), by using the Galerkin method and the kinematic relation.  $\boldsymbol{\psi}$  is a matrix containing the nodal enrichment function associated with each additional degree of freedom and  $\mathbf{B}^* = \tilde{\nabla}\mathbf{N}^*\boldsymbol{\psi}$  and  $\mathbf{B} = \tilde{\nabla}\mathbf{N}$  respectively. Eq. (3.3.15) and (3.3.16) now becomes

$$\int_V \mathbf{B}^T \mathbf{D}\mathbf{B} dV \mathbf{a} + \int_V \mathbf{B}^T \mathbf{D}\mathbf{B}^* dV \mathbf{a}^* = \int_S \mathbf{N}^T \mathbf{t} dS + \int_V \mathbf{N}^T \mathbf{b} dV + \int_V \mathbf{B}^T \mathbf{D}\boldsymbol{\epsilon}_0 dV \quad (3.3.17)$$

$$\int_V \mathbf{B}^{*T} \mathbf{D}\mathbf{B} dV \mathbf{a} + \int_V \mathbf{B}^{*T} \mathbf{D}\mathbf{B}^* dV \mathbf{a}^* = \int_S \mathbf{N}^{*T} \mathbf{t} dS + \int_V \mathbf{N}^{*T} \mathbf{b} dV + \int_V \mathbf{B}^{*T} \mathbf{D}\boldsymbol{\epsilon}_0 dV. \quad (3.3.18)$$

The equations can be written in a more compact matrix form, so that the stiffness matrix in the XFEM formulation becomes [23]

$$\mathbf{K}_{\text{XFEM}} = \begin{bmatrix} \mathbf{K}_{\text{Std.FEM}} & \mathbf{K}_{\text{Blended}} \\ \mathbf{K}_{\text{Blended}}^T & \mathbf{K}_{\text{Enriched}} \end{bmatrix} = \begin{bmatrix} \int_V \mathbf{B}^T \mathbf{D}\mathbf{B} dV & \int_V \mathbf{B}^T \mathbf{D}\mathbf{B}^* dV \\ \int_V \mathbf{B}^{*T} \mathbf{D}\mathbf{B} dV & \int_V \mathbf{B}^{*T} \mathbf{D}\mathbf{B}^* dV \end{bmatrix}$$

the displacement vector

$$\mathbf{a}_{\text{XFEM}} = \begin{bmatrix} \mathbf{a} \\ \mathbf{a}^* \end{bmatrix}$$

and the force vector

$$\mathbf{f}_{\text{XFEM}} = \begin{bmatrix} \mathbf{f} \\ \mathbf{f}^* \end{bmatrix} = \begin{bmatrix} \int_S \mathbf{N}^T \mathbf{t} dS + \int_V \mathbf{N}^T \mathbf{b} dV + \int_V \mathbf{B}^T \mathbf{D}\boldsymbol{\epsilon}_0 dV \\ \int_S \mathbf{N}^{*T} \mathbf{t} dS + \int_V \mathbf{N}^{*T} \mathbf{b} dV + \int_V \mathbf{B}^{*T} \mathbf{D}\boldsymbol{\epsilon}_0 dV \end{bmatrix}.$$

The resulting stiffness matrix consists of one part that is exactly the same as for the standard FEM formulation, hence it defines the stiffness for the elements outside the enriched domain. The completely enriched part is related to the elements in which all the nodes are enriched, and the blended stiffness applies to the elements where just some nodes are subjected to an enrichment function [15]. Depending on the chosen

enrichment function, some nodes in elements subjected to the blended stiffness may face the problem that  $u(x_i)^h \neq u(x_i)$ , which is especially problematic when applying essential boundary conditions. However, with the enrichments that are used in the present work for propagating cracks, i.e. the *Heaviside function*, this problem is not present.

### 3.3.4 Crack modeling in XFEM

Modeling of cracks is an application where the capabilities of XFEM is especially useful, and it was also one of the first problems in mechanics which were modeled by using the method [5].

A domain that contains a crack has a discontinuous displacement field across the open crack faces. Furthermore, the asymptotic stress function has a singularity at the crack tip according to the LEFM theory. The discontinuous "jump" in the displacement field at the crack faces can be realised in XFEM by choosing a step function as enrichment function at the nodes in elements which are completely cut by the crack. In order to keep track of where the crack face is located in the element, the level-set method is applied. In the level-set method, a level-set function  $\phi(\mathbf{x})$  is introduced, which for open interfaces can be defined on vector form as

$$\phi(\mathbf{x}) = (\mathbf{x} - \mathbf{x}_c) \cdot \mathbf{n}. \quad \forall \mathbf{x} \in \Omega \quad (3.3.19)$$

The vector  $\mathbf{n}$  is a unit vector orthogonal to the crack surface in the point  $\mathbf{x}_c$ .  $\mathbf{x}_c$  is the point on the crack surface closest to the point  $\mathbf{x}$ , in which the function is evaluated. A level-set function can be defined in different ways depending on what kind of problem that is to be modeled. However, it is always a continuous function with a constant value along a certain level, which on the crack face means that  $\phi(\mathbf{x}_c) = 0$ . In the resulting two sub-domains on each side of the crack, the level-set function is positive on one side and negative on the other. To completely define the crack, an additional tangential level-set function  $\gamma(\mathbf{x})$  can be used to define the position of the crack tip. The function is constructed so that the line  $\gamma(\mathbf{x}) = 0$  is perpendicular to the crack face at the crack tip. This can be done by defining

$$\gamma(\mathbf{x}) = (\mathbf{x} - \mathbf{x}_{\text{tip}}) \cdot \mathbf{t}_{\text{tip}} \quad \forall \mathbf{x} \in \Omega \quad (3.3.20)$$

where  $\mathbf{t}_{\text{tip}}$  is a tangent vector to the crack at the crack tip, located in the point  $\mathbf{x}_{\text{tip}}$ . The result of the level-set functions is a complete definition of the crack geometry

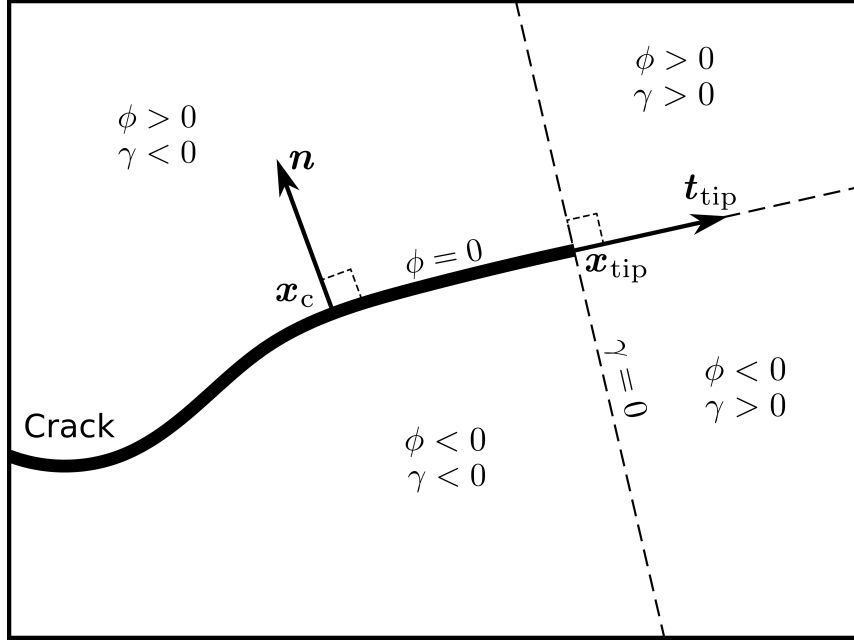


**Figure 3.8.** Crack represented by level-set functions in a 2D-domain.

as all points with the level-set values  $\{\phi(\mathbf{x}) = 0, \gamma(\mathbf{x}) \leq 0\}$ , which can be seen in Fig. 3.8. The crack-face discontinuity in the displacement field can be introduced as the discontinuous Heaviside function  $H(\phi(\mathbf{x}))$ , dependent on the level-set. The enrichment function  $\psi_{cf}(\mathbf{x})$  for elements which are completely cut by a crack is then defined as

$$\psi_{cf}(\mathbf{x}) = H(\phi(\mathbf{x})) = \begin{cases} 1 & \text{if } \phi(\mathbf{x}) \geq 0 \\ -1 & \text{if } \phi(\mathbf{x}) < 0 \end{cases} \quad (3.3.21)$$

When a stationary crack is modeled in a brittle linear elastic material, the LEFM concepts can be applied. The stress singularity at the crack tip is incorporated by using an enrichment function based on the corresponding displacement field close to the crack tip, which has the analytical solution presented in Eq. (3.1.4) and (3.1.5). Based on these equations, the displacement field in the neighbourhood of a crack tip in an isotropic material can be represented by the four enrichment functions contained in the vector

$$\begin{aligned} \boldsymbol{\psi}_{tip}(\mathbf{x}) &= \left[ \psi_{tip,1}(\mathbf{x}), \psi_{tip,2}(\mathbf{x}), \psi_{tip,3}(\mathbf{x}), \psi_{tip,4}(\mathbf{x}) \right] = \\ &= \left[ \sqrt{r} \cos\left(\frac{\theta}{2}\right), \sqrt{r} \sin\left(\frac{\theta}{2}\right), \sqrt{r} \sin\left(\frac{\theta}{2}\right) \sin(\theta), \sqrt{r} \cos\left(\frac{\theta}{2}\right) \sin(\theta) \right] \end{aligned} \quad (3.3.22)$$

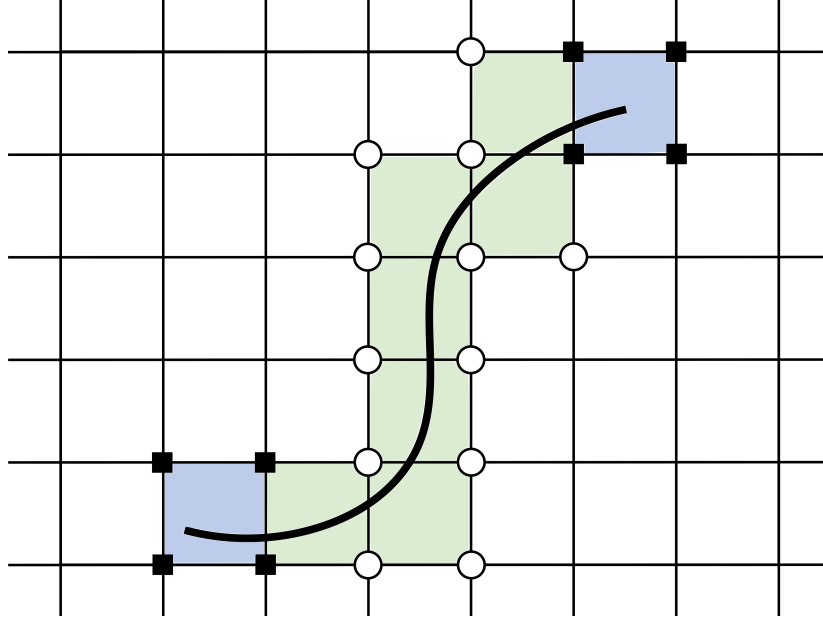


**Figure 3.9.** XFEM representation of a crack in a 2D-domain. The squares represent nodes where the crack tip enrichment is applied, and the circles represent the nodes enriched with the discontinuous step function

which are only applied to the degrees of freedom at the nodes in elements that contain a crack tip [5, 23]. The local coordinates  $r$  and  $\theta$ , defined in Fig. 3.1, relates to the level-set functions so that

$$\theta = \arctan\left(\frac{\phi}{\gamma}\right) \quad (3.3.23)$$

$$r = \sqrt{\phi^2 + \gamma^2}. \quad (3.3.24)$$

With the two types of enrichment functions, where the step function represents the discontinuous crack face and the displacement functions from Eq. (3.3.22) represent the crack tip singularity, the XFEM approximation for the displacements can explicitly be written as

$$u^h(\mathbf{x}) = \underbrace{\sum_{i \in I} N_i(\mathbf{x}) a_i}_{\text{Std. FEM approx.}} + \underbrace{\sum_{i \in I_{\phi, \gamma}^*} N_i^*(\mathbf{x}) \psi_{\text{cf}}(\mathbf{x}) b_i}_{\text{Crack surface enrichment}} + \underbrace{\sum_{j=1}^4 \sum_{i \in I_{\text{tip}}^*} N_i^*(\mathbf{x}) \psi_{\text{tip}, j}(\mathbf{x}) c_{i, j}}_{\text{Crack tip enrichment}} \quad (3.3.25)$$

for a stationary crack. In this equation,  $c_{i, j}$  are the additional degrees of freedom at the nodes in the element that contains the crack tip and  $b_i$  are the degrees of freedom at the nodes in elements cut by the crack face. This discretisation can graphically be seen in Fig. 3.9, where the squares are the nodes with the crack tip enrichment and the circles are the nodes enriched with the discontinuous step function. It is emphasised

that in the present work only propagating cracks are modeled, and the discretisation of such cracks in XFEM usually does not include any crack tip enrichment. Since the crack tip element is changing as the crack propagates, it is difficult to incorporate this enrichment in an efficient way. The drawback with not including the crack tip enrichment is that the crack tip can only be represented at the element boundaries by the discontinuous enrichment function  $\psi_{\text{cf}}$ . Therefore, some other criterion has to be used instead of evaluating the stress intensity factor to calculate when the crack will extend, which is further discussed in chapter 4. The discretised displacement function for a propagating crack then results in

$$u^{\text{h}}(\mathbf{x}) = \underbrace{\sum_{i \in I} N_i(\mathbf{x}) a_i}_{\text{Std. FEM approx.}} + \underbrace{\sum_{i \in I_{\phi, \gamma}^*} N_i^*(\mathbf{x}) \psi_{\text{cf}}(\mathbf{x}) b_i}_{\text{Crack surface enrichment}} \quad (3.3.26)$$



# Chapter 4

## Method

In this chapter the theory concepts are applied in the numerical FEM models through the CZM and the XFEM implementations in *Abaqus/Standard*. The discretisations of the L-flange and the SCB test with their associated boundary conditions and material properties are presented. Furthermore, the procedure of the simulation strategy is explained which enables delamination migration to be simulated within the limitations set by the FEM software.

### 4.1 The general structure of the continuum model with propagating cracks

In the numerical models, laminated FRPs with homogeneous material properties are represented by linear continuum elements. An assumption of plane strain is made, which is applicable for planar symmetric structures. If the out-of-plane width in the actual 3D-geometry is sufficiently large, it is assumed that all strain deformations are within one plane. Hence, the size of the numerical models can be reduced to a 2D-structure.

Only cross-ply laminates with ply orientations  $0^\circ$  and  $90^\circ$  are simulated, and the transversely isotropic plane of the  $90^\circ$ -plies coincides with the modeling plane. As a result, all plies with a  $90^\circ$ -orientation are modeled as isotropic materials while the plies with a  $0^\circ$ -orientation are modeled as orthotropic. Moreover, all materials are assumed to be massless, and dynamic effects due to inertia are thereby neglected.

The discretised plies are joined together according to the stacking sequence of the respective model. The interface connection between two plies is achieved through a surface-based cohesive contact interaction. As an interface crack initiates and

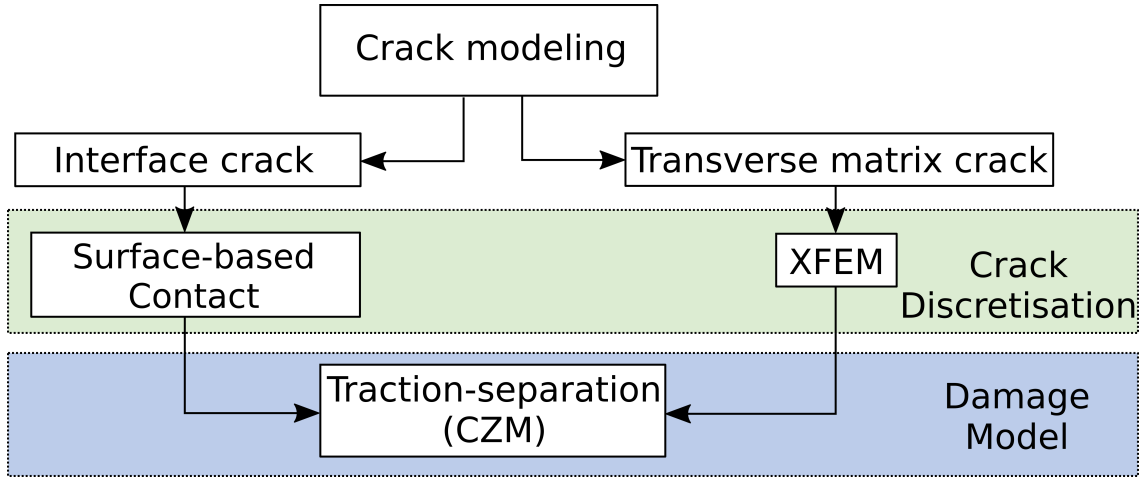


**Figure 4.1.** Overview of the applied crack models for delamination and transverse matrix cracks

propagates in the ply-interface, this interaction is governed by the CZM.

The other type of crack that is present in the models are intralaminar ply cracks in the form of transverse matrix cracks. As their crack path and location is unknown a priori, they are modeled by applying XFEM in regions where matrix cracks are likely to occur. This is exclusively done in plies orientated in the  $90^\circ$ -direction and consequently the material properties in the enriched elements are isotropic. The damage evolution for XFEM cracks is simulated with the cohesive traction-separation model, similarly to the interface cracks. An overview of how the two crack types are incorporated in the model is given in Fig. 4.1.

## 4.2 Ply Modeling

Plane strain continuum elements are used to model each ply, and the ply orientations are obtained by defining the in-plane material properties accordingly. The ply-angle is defined relative to the modeling plane so that  $0^\circ$ -plies have their fibers aligned parallel to this plane. Consequently, the  $90^\circ$ -plies are defined as isotropic by the Young's modulus, Poisson's ratio, tensile strength and fracture toughness in the transverse direction of the ply.

Based on the experiments presented in chapter 2, intralaminar crack initiation and propagation during delamination migration is expected to occur in the  $90^\circ$ -plies. To account for the transverse matrix cracks, XFEM is applied due to the ability of predicting an arbitrary crack path. This should be seen in contrast to delamination, which always extends in a ply interface.

### 4.2.1 Crack propagation in XFEM

A sub-domain of elements within a 90°-ply is defined as a crack domain in which a potential crack can nucleate and propagate. In the crack domain, the nodes have additional degrees of freedom which are incorporated through the enrichment functions. However, in the absence of discontinuities, the additional degrees of freedom are disabled. When a discontinuous feature in form of a propagating crack is introduced to the crack domain, the additional degrees of freedom at the nodes of the elements which are hosting the crack are enabled. This can be seen in Fig. 4.2 a) where a nucleated edge-crack interface can be seen in one element. The enrichment degrees of freedom are active in this element and inactive in the other elements in the crack domain.

For propagating cracks, the discontinuous level-set dependent step function is the enrichment function, as in Eq. (3.3.26). The asymptotic crack tip enrichment function is not applied. As a result of this, the crack can only propagate a discrete number of whole elements so that the crack tip always is located on an element boundary.

In the present work, a crack nucleates in an element located in the pristine undamaged crack domain when a stress-based crack initiation criterion is fulfilled during a load increment step. This can be expressed as

$$f = \frac{\langle \sigma_{\max} \rangle}{R_{22}^t} \quad (4.2.1)$$

where  $\sigma_{\max}$  is the largest principle stress and  $R_{22}^t$  is the tensile strength in the transverse direction of a ply. The crack is initiated when

$$1 \leq f \leq 1 + f_{\text{tol}} \quad (4.2.2)$$

and  $f_{\text{tol}}$  is a tolerance that has to be set sufficiently small. If  $f > 1 + f_{\text{tol}}$  in the current load increment step, cut-backs are made until Eq. (4.2.1) is satisfied. The crack path which is splitting the element in two halves is determined by finding the direction perpendicular to the eigenvector corresponding to  $\sigma_{\max}$ , i.e. the direction perpendicular to the maximum principle stress. Additionally, in the XFEM implementation in *Abaqus/Standard*, a crack in an initially intact crack domain always passes through the centre of the first element in which it nucleated.

When the crack is introduced in the first element and its direction is established, it can propagate to a second adjacent intact element where the crack tip is located on one of its edges. Again, the initiation criterion in Eq. (4.2.1) and (4.2.2) must be

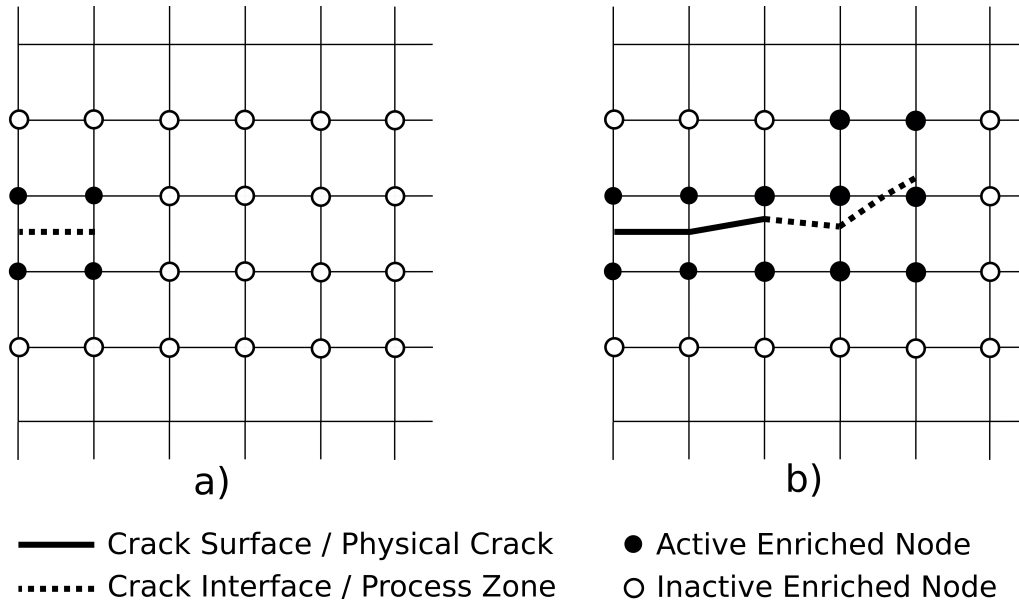


**Figure 4.2.** A crack domain defined by the elements with circular nodes. In a) a crack has been initiated in the first element and a crack interface in form of a cohesive process zone is created. In b) the crack has propagated in the crack domain and the process zone can be seen ahead of the crack tip.

satisfied in the point of the crack tip and the propagation direction is determined as perpendicular to the maximum principal stress in the intact element. Following this procedure, the crack can propagate through the crack domain and the arbitrary path in Fig. 4.2 b) is obtained.

The distinction should be made between crack interfaces and crack surfaces. Since a progressive damage model is applied to the XFEM cracks, the cohesive traction-separation model describes the stresses acting in the crack interface which coincides with the initiated crack path. This interface is the cohesive process zone of the XFEM crack. A crack surface on the other hand is the physical crack where the material has failed completely, the critical strain energy release rate has been reached and no cohesive tractions remain. The crack surface and the cohesive crack interface ahead of the physical tip can be seen in Fig. 4.2 b).

When the crack interface in an element is established through the initiation criterion, the progressive damage across this interface is modeled using cohesive segments. This essentially means that phantom nodes are superposed on the real nodes on each side of the crack interface which are completely constrained to each other at the undamaged state. As the damage progresses, the separation between the phantom nodes and their corresponding real nodes is governed by the CZM. When the interface has failed completely according to the CZM, the phantom nodes and the

real nodes can move independently from each other. The integration of an element cut by a crack interface is made over each half of the element defined by the real nodes and the level-set.

### 4.2.2 Practical application of XFEM for propagating cracks

In order to simulate propagating cracks with sufficient accuracy in XFEM, care has to be taken when the mesh is created. Although XFEM can work with a coarse mesh, the calculation of the crack extension depends on the discretisation. The direction in which the crack propagates, calculated by finding the direction perpendicular to the maximum principle stress, is only valid in the region close to the crack tip. Furthermore, if the crack extends a discrete number of first order elements, the size of these must be sufficiently small to minimise the influence from the mesh topology.

As the crack path is arbitrary, some numerical issues can occur when an element is cut by a crack interface close to a node or an element edge. If the element is split in two halves that are very unequal in size, the area ratio between these two halves is large. Consequently, the stiffness matrix can become ill-conditioned, leading to problems with convergence in the numerical solver and in worst case the calculation fails [15]. This problem can potentially be helped by using an adaptive re-meshing technique or by introducing additional constraints for the crack path, but this is not supported with XFEM in *Abaqus/Standard* [1] and is not done in the present work. Instead, the topology of the mesh in the crack domain is slightly modified when this problem occurs and if the crack path is sufficiently mesh independent, the problem can potentially be resolved in this way.

In the present work, the XFEM implementation in *Abaqus/Standard* is used to simulate all intralaminar cracks. As this is a commercial FEM software, many parameters in the code are fixed. The limitations have to be identified and dealt with accordingly, in order to perform simulations that can represent the actual physics of the problem. Some of the issues related to propagating cracks are summarised as follows:

- The crack tip singularity is not explicitly represented by the enrichment functions.
- No initial crack is required in the crack domain and nucleation of new cracks occur by fulfilling the stress-based initiation criterion.
- Only one crack can exist in an element.

- A crack can only extend through a whole element at the time and only propagate through one element per load increment.
- An initiated crack in a pristine intact crack domain always passes through the centre of the element in which it nucleated.
- A crack nucleates in all elements in an intact crack domain where the crack initiation criterion is satisfied for a given load increment. Consequently, if the criterion is met in multiple elements in the same crack domain during one load increment, multiple cracks will nucleate.
- When one or multiple propagating cracks are initiated, no new cracks can nucleate in the same crack domain.
- The change of direction in which the crack propagates is limited to  $\pm 90^\circ$  over one element.
- A crack can propagate from one crack domain to another if they are adjacent and no other crack exist in the second crack domain.
- If the crack propagates completely over the crack domain and thereby stops to propagate, only then can new cracks nucleate in the same crack domain.
- Branching and intersection of cracks is not supported.
- Only isotropic material properties can be applied to the elements within the crack domain.
- Only first order elements can be used for plane strain models.

When considering these limitations, it is clear that some difficulties may arise when XFEM in *Abaqus/Standard* is applied to complex problems with interacting failure mechanisms and irregular geometries. Some of the issues mentioned above can even result in unphysical representations of the fracture events if not dealt with properly. However, XFEM has its potential, and a workaround for some of the shortcomings in the implementation is developed in the present work, which is described in the simulation procedure in section 4.7.

### 4.3 Interface modeling

Delamination takes place in the interface between the plies, hence the possible delamination path is thereby essentially known a priori. However, if the laminate consists of many plies and no initial interface crack exist, it is necessary to determine where and in which interface delamination initiates. The modeling of the interfaces can be divided in two parts; A contact formulation between the continuum elements that represent the plies, and the CZM which is the damage model and the constitutive coupling across the ply interfaces. The CZM enables initiation and propagation of cracks at an arbitrary location along the interface path

Due to the approach in the ply modeling where homogeneous material properties are applied, the interfaces between plies with the same orientation are not created, and a ply section can thereby represent one or many plies. The interfaces between plies with different orientation are discretised with a surface-based cohesive contact that represents the material discontinuity. This assumes that the initial thickness of the actual interface segment is zero. The contact is based on a master-slave formulation where contact elements between the surfaces are generated internally. Since the contact is defined between the element surfaces and not through a node-to-node or node-to-surface formulation, it is possible to have non-conforming meshes on each side of an interface. By using the surface-based contact, the risk for interpenetration of the surfaces is reduced and stresses can be transferred across the interface more accurately than for a node-to-surface formulation. A finer mesh on the slave surface than on the master surface thereby increases the accuracy of the stress field. Additionally, an assumption of small sliding in the surface-based contact is made. This means that the relative displacement of the surfaces is measured from the initial contact point, which is in accordance with the nature of bonded surfaces.

For an intact laminate, initial contact and constitutive coupling in form of the CZM is applied between the plies. The elastic interface stiffness  $K_{ii}$  from Eq. (3.2.9) should be set relatively high in comparison to the Young's modulus of the material since the interface thickness is assumed to be zero [7]. Theoretically, an infinitely large value of  $K_{ii}$  corresponds to a completely constrained coupling between the elastic surfaces but is due to convergence difficulties not suitable.

The interface crack is initiated through the quadratic initiation criterion from Eq. (3.2.17). Similar to the initiation of the XFEM crack, the criterion must be fulfilled within a small tolerance. If the criterion is exceeded above the tolerance, cut-backs in the load increment are made. The CZM is employed to model the traction-separation behaviour between the contact surfaces. When the failure displacement is reached,

which correlates to  $\mathcal{G} = \mathcal{G}_c^{\text{BK}}$ , the surfaces can move independently from each other and a physical crack is thereby introduced.

The post-failure behaviour of the crack surfaces, created by delamination propagation, is assumed to be a hard contact that prevents interpenetration. This is enforced through Eq. (3.2.15), and by re-initialising the normal stiffness  $K_{nn}$ . Moreover, the interaction between the failed surfaces is defined as frictionless.

### 4.3.1 Discretisation of the cohesive interfaces

An adequate discretisation of the ply interfaces is of great importance in order to capture the delamination and the cohesive process zone ahead of the crack tip accurately. By doing an estimate of the cohesive zone length and determine the sufficient number of elements required to represent it, the element length in this zone can be calculated. The length of the cohesive zone  $l_{cz}$  can be estimated according to [7] as

$$l_{cz} = ME \frac{\mathcal{G}_c}{\hat{t}_s^2}. \quad (4.3.1)$$

For transversely isotropic materials,  $E = E_2$  which is the Young's modulus in the transverse direction of the ply material and  $M$  is a correction factor. Hillerborg [20] has suggested that  $M = 1$  and Barenblatt [4]  $M = \frac{\pi}{8} \approx 0.4$ .  $\mathcal{G}_c$  is the critical strain energy release rate and depends on the mode of fracture. For mixed mode loading, a rough estimation of  $l_{cz}$  is made in the present work as

$$\frac{0.4E_2\mathcal{G}_c^{\min}}{\hat{t}_s^2} \leq l_{cz} \leq \frac{E_2\mathcal{G}_c^{\max}}{\hat{t}_s^2}. \quad (4.3.2)$$

The element length can be calculated as

$$l_e = \frac{l_{cz}}{n_e} \quad (4.3.3)$$

where  $n_e$  is the number of elements in the cohesive process zone which typically is in the range of 3-8 elements. This method of estimating the required size of the elements is very approximative and should only be taken as a starting point when doing the discretisation. However, it does provide some initial knowledge about the size of the cohesive process zone.



## 4.4 Viscous regularisation

In non-linear implicit FEM simulations with propagating cracks, convergence can be an issue. This is especially true if unstable fracture events are involved, which is the case in the present work. The bi-linear damage model can lead to a sudden softening of the structural stiffness, and measures must be taken to make sure that a positive definite tangent stiffness matrix is maintained [24]. In order to deal with this, a viscous regularisation scheme is introduced, which works as a purely artificial numerical damping of the system. A viscous damage variable  $d_v$  is introduced so that

$$\frac{d(d_v)}{dt} = \frac{(d - d_v)}{\mu} \quad (4.4.1)$$

where  $dt$  is the time increment and  $d$  is the current damage state. The interpretation of  $dt$  for a non-linear static simulation is the fraction of the complete load step that corresponds to the current load increment. By assigning a value to the viscosity parameter  $\mu$ , the viscous damage variable can be calculated for a given time increment. Thus, the viscous damage variable can be substituted for the regular damage parameter in the stiffness matrix.

An adequate value of  $\mu$  is related to  $dt$  and has to be determined somewhat iteratively from case to case. A very unstable crack propagation requires small increment steps for which a sufficient value of  $\mu$  must be chosen. If  $\mu$  is set to a relatively high value, the structural behaviour of the system can be affected during damage progression since the viscous damage contributes to the stiffness. On the other hand, the calculation time can be reduced and the convergence rate increased. If  $\mu$  is set to a relatively low value, it affects the system less, but slower or no convergence is to be expected. Hence, it is crucial to find a sufficient value of  $\mu$  that helps the calculation to overcome converge difficulties without affecting the system too much. In the present work, different values are tested and their impact is evaluated in order to achieve good numerical simulations.

## 4.5 FEM model of the single cantilever beam test

The FEM model of the specimen in the SCB test is created in *Abaqus/Standard* with the ply- and interface discretisation explained in the previous sections. First order quadrilateral plane strain continuum elements with full integration are used to model the plies. Adjacent plies with the same fiber direction are meshed together as one element set, and the surface-based cohesive contact is used in the  $0^\circ/90^\circ$  interfaces in

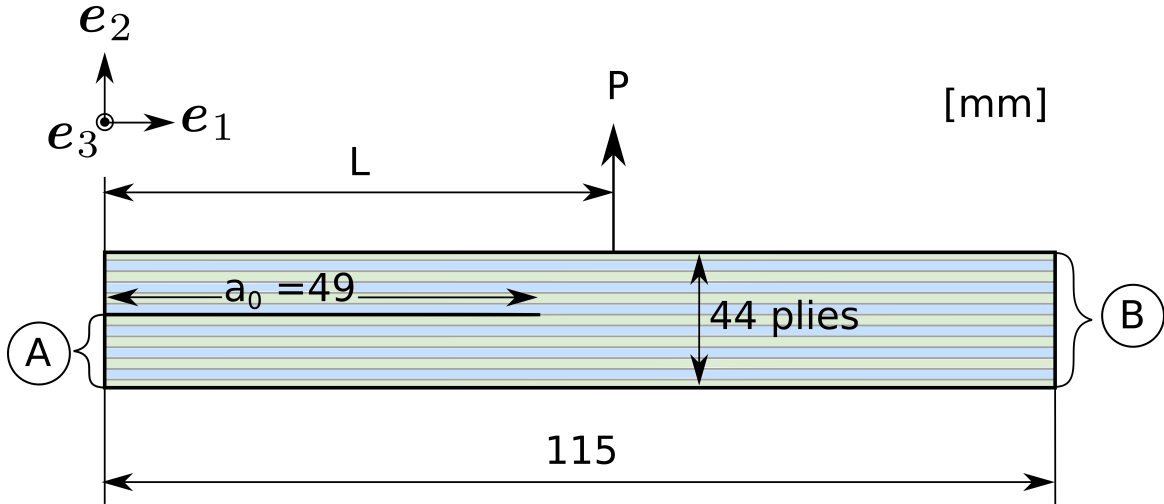


**Figure 4.3.** *Boundary conditions and load introduction for the discretised plane strain model of the SCB test.*

the cross-ply laminate.

Some simplifications are made in the numerical model compared to the experimental set-up in Fig. 2.1. This can be seen in Fig. 4.3 where the loads and boundary conditions are indicated. In the coordinate system  $(e_1, e_2, e_3)$  the  $0^\circ$ -ply direction is parallel to  $e_1$  and the  $90^\circ$ -direction is parallel to  $e_3$ . The clamping of the specimen to the bottom plate is not modeled and instead replaced with a fixed boundary condition at all nodes along the edges indicated as A and B. This can be written as  $U_1 = U_2 = 0$  where  $U_1-U_3$  are the translational degrees of freedom in the coordinate system directions. The simplification of the clamped ends is based on [34], where different boundary conditions for the SCB test have been compared. Hence, the simplified model has less degrees of freedom compared to a model which includes the entire clamping and the introduction of uncertainties in form of contact interaction with the clamps is avoided.

The material properties of a unidirectional IM7/8552 carbon/epoxy laminate of which each ply in the SCB test is made can be seen in Table 4.1 [33]. The material properties are assigned to the plies according to the stacking sequence in section 2.1. An initial delamination front is created by defining a long debonded contact between ply 22 and 23 over the length  $a_0 = 49$  mm. This is indicated in Fig. 4.3 and only Eq. (3.2.15) with the penalty stiffness  $K_{nm}$  is applied here in order to avoid interpenetration. The properties of the interfaces between the plies can be seen in Table 4.2, where the initial stiffness is assumed to be in the order of 10 times the Young's modulus of the ply material.

The structured mesh is refined over the length for which the delamination is

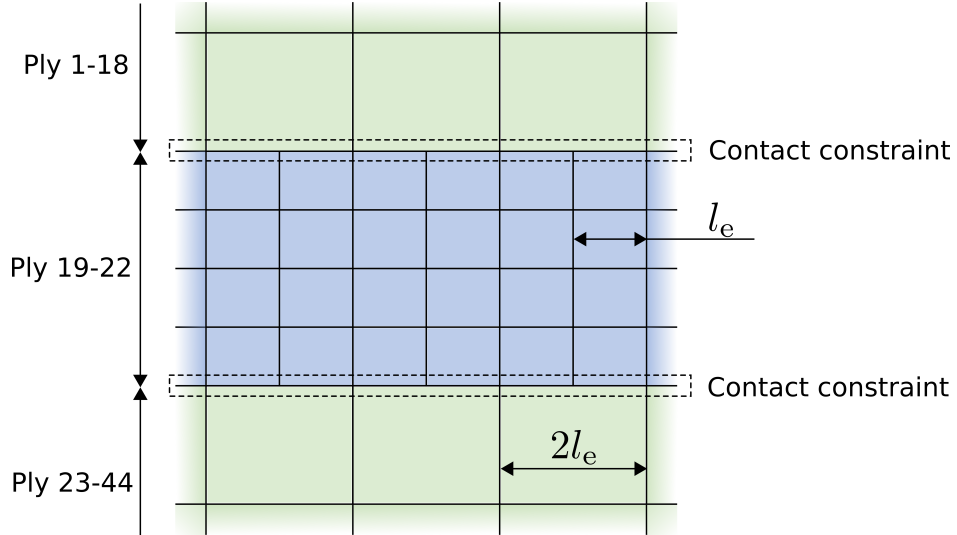


**Figure 4.4.** Schematic discretisation of ply 19-22 and the adjacent plies. The characteristic element length  $l_e$  is defined and the surface-based contact is applied in the interfaces as indicated.

expected to propagate, starting from the location of the initial crack tip. In the mesh domain that represents ply 19-22, the transverse matrix crack nucleated in the experiments in [33] and the delamination propagated along the adjacent interfaces. Hence, it is meshed finer than the other plies with approximately one half of the element length. This is shown in Fig. 4.4 for a coarse discretisation where only one element is used over the ply thickness in ply 19-22. The characteristic element length  $l_e$  is in the present work defined as indicated in Fig. 4.4, and consequently the number of elements over the ply thickness depends on  $l_e$ , as the same aspect ratio is maintained for all discretisations. The reason for using a non-conforming mesh in the contact region is that the accuracy increases with a finer mesh on the slave surface than on the master surface. Additionally, it can provide a sufficient mesh size for the XFEM cracks to propagate without refining the whole mesh, and thereby can the computational cost be decreased.

The length of the cohesive process zone in the ply interface is estimated through Eq. (4.3.2) to  $0.08 \text{ mm} \leq l_{cz} \leq 0.73 \text{ mm}$ . This estimation is the starting point for the discretisation of the model. A mesh sensitivity study is performed for  $0.025 \text{ mm} \leq l_e \leq 0.5 \text{ mm}$ , corresponding to 1-4 elements over the ply thickness, to determine an adequate discretisation, which is presented in the result section.

At the beginning of the simulation, all interfaces except for the traction-free initial delamination front are assumed to be undamaged. A displacement  $U_2 = 1.2 \text{ mm}$  is introduced directly to ply 1 at a distance  $L$  from the left end of the laminate, resulting

in the force  $P$  at this point. In order to verify the model, the mesh sensitivity study is carried out and the amount of viscous regularisation that is required is evaluated. Three different load cases for  $L = 1.1a_0$ ,  $L = 1.2a_0$  and  $L = 1.3a_0$  are simulated for comparison with the experimental results from the SCB test in [33].

**Table 4.1.** *Material properties for a unidirectional IM7/8552 carbon/epoxy laminate where the 1-direction is parallel to the fibers [33, 34].*

Elastic constants	$E_1 = 161$ GPa	$E_2 = 11.38$ GPa	$E_3 = 11.38$ GPa
	$G_{12} = 5.17$ GPa	$G_{13} = 5.17$ GPa	$G_{23} = 3.98$ GPa
	$\nu_{12} = 0.32$	$\nu_{13} = 0.32$	$\nu_{23} = 0.436$
Transverse tensile strength	$R_{22}^t = 73$ MPa		
Critical strain energy release rate	$\mathcal{G}_{Ic}^{\text{matrix}} = 200$ J/m <sup>2</sup>	$\mathcal{G}_{IIc}^{\text{matrix}} = 770$ J/m <sup>2</sup>	

**Table 4.2.** *Interface properties for the model of the cross-ply laminate in the SCB test [34].*

Interface stiffness	$K_{nn} = 1000$ GPa	$K_{ss} = 1000$ GPa
Interface strength	$\hat{t}_n = 60$ MPa	$\hat{t}_s = 110$ MPa
Critical strain energy release rate	$\mathcal{G}_{Ic} = 210$ J/m <sup>2</sup>	$\mathcal{G}_{IIc} = 770$ J/m <sup>2</sup>

## 4.6 FEM model of the L-flange test

The model of the L-flange is discretised in a very similar manner as for the case of the SCB model regarding plies and ply interfaces. First order quadrilateral plane strain continuum elements with full integration are used to model the plies, and the interfaces between plies with different orientation are modeled with the contact formulation and the CZM. The relevant geometry of the model can be seen in Fig. 4.5 together with the boundary conditions and the load introduction point. A coordinate system ( $\mathbf{e}_1, \mathbf{e}_2, \mathbf{e}_3$ ) is defined and the corresponding degrees of freedom  $U_1$ - $U_3$  are the displacements in these directions.

The lower part of the vertical leg, indicated as A is fixed so that  $U_1 = U_2 = 0$  at all nodes along these two edges. At the left side of the upper vertical part indicated as

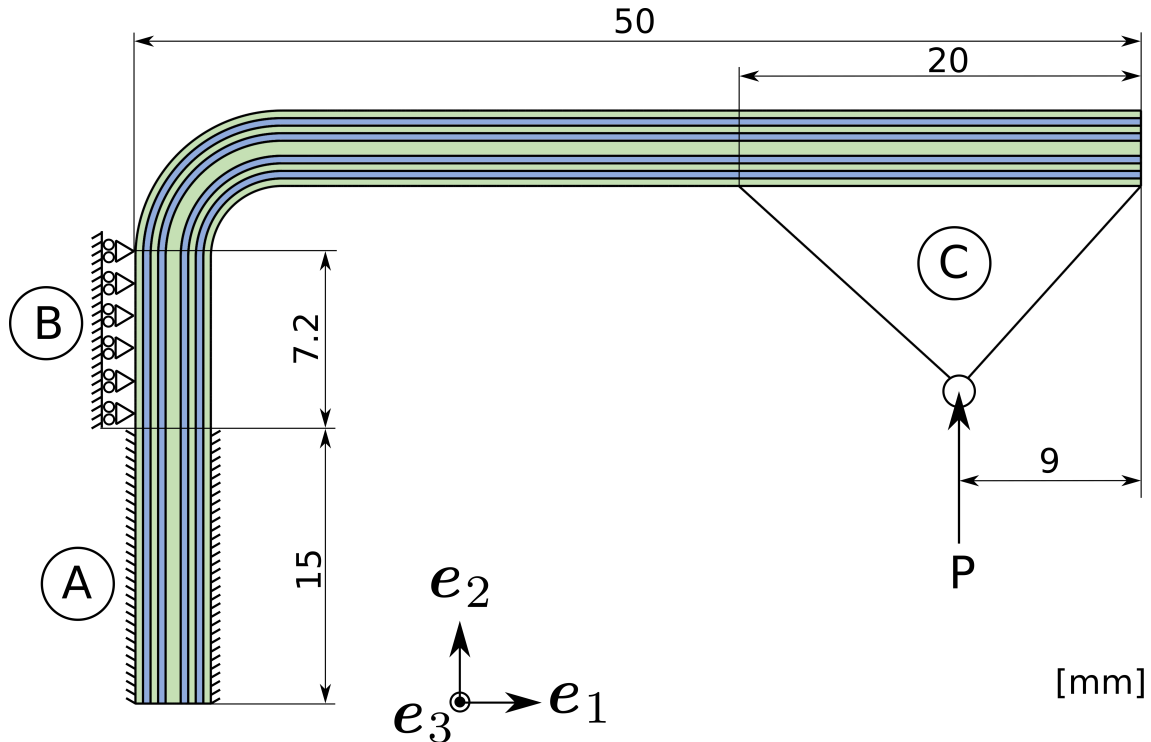


**Figure 4.5.** *Boundary conditions and load introduction for the plane strain model of the L-flange test.*

B, the nodes are constrained in the horizontal direction which corresponds to  $U_1 = 0$ . This is a simplification that is made from the physical model where this part of the L-flange is in contact with the fixed loading device. However, according to the simulations in [37] the contact area does not change significantly during loading and can thereby be approximated this way. The alternative is to model the loading device as a rigid part and introducing a contact with the L-flange instead. This results in higher computational cost and uncertainty in form of a possibly frictional contact interaction and is therefore not considered.

The point C indicates the asymmetric loading block on which a displacement is introduced. The loading block is modeled as a triangularly shaped rigid part where the resulting force  $P$  is acting at the lower tip during loading. A tie-constraint is used between the loading block and the lower edge of the horizontal arm on the L-flange, preventing the two surfaces from moving relative to each other.

In the coordinate system in Fig. 4.5, the  $0^\circ$ -direction of the plies is parallel to  $e_1$ - $e_2$ -plane and the  $90^\circ$ -direction is parallel to  $e_3$ . The properties of the unidirectional material which the plies are made of can be seen in Table 4.3. The isotropic elastic properties of the  $90^\circ$ -plies in the modeling plane are defined by the constants  $E_2$  and  $\nu_{23}$  and the  $0^\circ$ -plies are defined as orthotropic. The interface properties between the

plies in the model can be seen in Table 4.4.

The mesh consists of rectangular elements with an aspect ratio close to 1 except for in ply 10-12. In the mesh domain that represents ply 10-12 the transverse matrix crack nucleated in the experiments in [37] and the delamination propagated in the adjacent interfaces. Similarly to the case of the SCB model as shown in Fig. 4.4, the same definition of  $l_e$  is made, so that the elements in this mesh domain are refined to one half of the length of the elements in the other plies. An estimation of the cohesive zone length in the ply interface yields  $0.04 \text{ mm} \leq l_{cz} \leq 0.34 \text{ mm}$  according to Eq. (4.3.2), and the element length  $l_e = 0.05 \text{ mm}$  is applied, resulting in 5 elements over the ply thickness. A mesh sensitivity study is performed in the exact same manner as explained for the SCB model in the result section to verify that the mesh size is sufficient.

At the initial state of the simulation, all interfaces and plies are intact and no initial crack exist. A displacement is prescribed in the positive  $\mathbf{e}_2$ -direction by assigning a value to  $U_2$  at the lower tip of the loading block, resulting in the force  $P$ .

**Table 4.3.** *Material properties for a unidirectional Cycom<sup>®</sup> 977-2-35%-12KHTA-134-300 carbon/epoxy laminate, which is the ply material in the model of the L-flange. The 1-direction is paralell to the fibers [29, 37].*

Elastic constants	$E_1 = 133 \text{ GPa}$	$E_2 = 9 \text{ GPa}$	$E_3 = 9 \text{ GPa}$
	$G_{12} = 4.4 \text{ GPa}$	$G_{13} = 4.4 \text{ GPa}$	$G_{23} = 3.5 \text{ GPa}$
	$\nu_{12} = 0.35$	$\nu_{13} = 0.35$	$\nu_{23} = 0.2857$
Transverse tensile strength	$R_{22}^t = 82 \text{ MPa}$		
Critical strain energy release rate	$\mathcal{G}_{Ic}^{\text{matrix}} = 200 \text{ J/m}^2$		$\mathcal{G}_{IIc}^{\text{matrix}} = 600 \text{ J/m}^2$

**Table 4.4.** *Interface properties for the L-flange model [29, 37].*

Interface stiffness	$K_{nn} = 1000 \text{ GPa}$	$K_{ss} = 1000 \text{ GPa}$
Interface strength	$\hat{t}_n = 60 \text{ MPa}$	$\hat{t}_s = 110 \text{ MPa}$
Critical strain energy release rate	$\mathcal{G}_{Ic} = 133 \text{ J/m}^2$	$\mathcal{G}_{IIc} = 460 \text{ J/m}^2$

## 4.7 The simulation procedure

In the present work, two types of crack propagation are modeled with two different approaches. The XFEM discretisation is used for arbitrary intralaminar cracks and the surface-based contact formulation is used for the interlaminar cracks. Both models are combined with the CZM to account for progressive damage ahead of the crack tip.

It is clear from the literature that these two models are working good separately. However, combining them to make them work together in the current implementation of *Abaqus/Standard* offers some challenges, mainly due to the limited capabilities of XFEM, as discussed in 4.2.2. Hence, a simulation strategy is employed that can overcome some of these shortcomings.

In order to find the location for delamination migration, the simulation of one load configuration is run multiple times. This can be summarised in three steps as initial approximation, verification and adjustment of the location.

The first completed simulation run is performed with multiple crack domains assigned at different locations in the ply where transverse matrix cracks are expected. The schematic outcome of such simulation is visualised in Fig. 4.6 a), where the coordinate  $s$  refers to a position along the ply. In this case, the delamination propagates in the positive  $s$ -direction in the first interface between the lower and the middle ply. In each crack domain 1-8, a matrix crack can initiate due to the XFEM crack initiation criterion and propagate partially through the ply. In crack domain 9, the initiated matrix crack propagates through the ply to the second interface between the middle and the upper ply, leading to delamination migration. The first simulation run can thereby predict an approximate location for the migration event.

If delamination migration is detected in one crack domain as in Fig. 4.6 a), all other crack domains are suppressed when restarting the simulation from the beginning and initialising the second run. By doing so, the assumption is made that no damage occurs in the middle ply before a single matrix crack is initiated at a location where it causes complete delamination migration. In Fig. 4.6 b) this can be seen where crack domain 9, located at the position  $s_0$  is the only crack domain in the ply, and verifies the initial approximation of the migration location.

If the result in Fig. 4.6 b) is obtained, it is possible that the location  $s_0$  of the crack domain needs to be corrected. This is done because of the discrete distribution of crack domains during the first simulation run and since damage before migration in the second simulation run is neglected, which may affect the stress field in the ply. By adjusting the position  $s_0$  and restarting the simulation a third time, the final predicted location for delamination migration  $s^*$  can be found, depicted in Fig. 4.6 c).

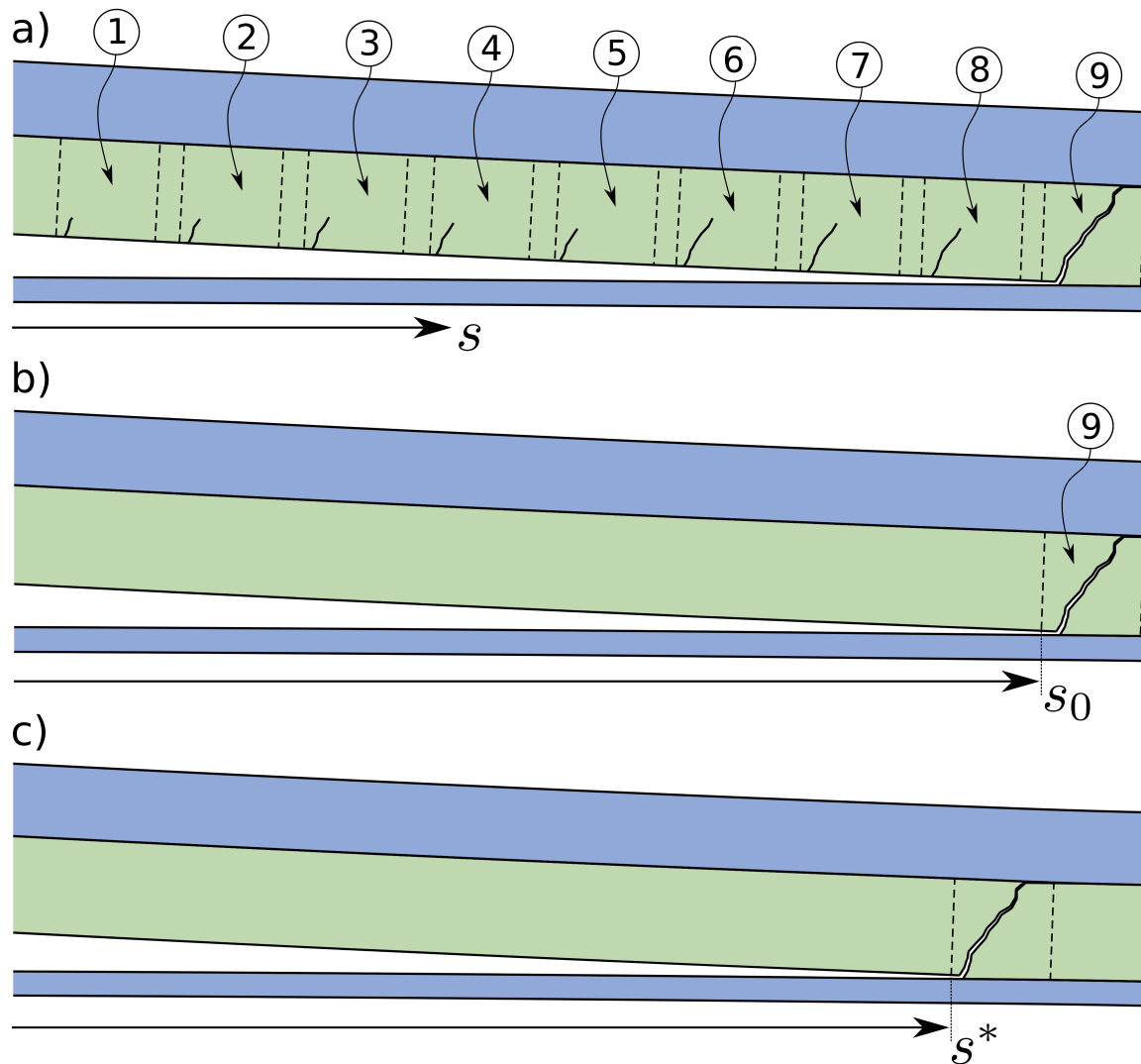


**Figure 4.6.** *The simulation procedure for finding the delamination migration location. In the first simulation run a) multiple crack domains are assigned and transverse matrix cracks are initiated. The location is verified in b) and corrected in c) according to the assumption of no ply-damage before complete migration.*

Depending on the required accuracy, the simulation can be restarted additional times while iteratively adjusting  $s_0$ . The location  $s^*$  is defined as the first point that the interface crack reaches where the initiated matrix crack causes complete delamination migration.

The main reason for employing this procedure with a sequence of simulations is that only one propagating crack is permitted per crack domain. As the maximum principle stress may be high in the neighbourhood of the delamination front, initiation of transverse matrix cracks can be triggered. However, if the crack driving force in the



direction of the transverse crack is too low, the matrix crack cannot propagate and instead delamination proceeds. If only one long crack domain is applied over the whole mid-ply in Fig. 4.6, no new cracks can nucleate after the first one has been initiated. Subsequently, multiple crack domains have to be employed in order to generate an initial prediction of the migration location.

An important assumption that is made in the presented simulation procedure is that damage to the plies prior to complete delamination migration is neglected. To only have a discrete number of assigned crack domains as in Fig. 4.6 a) is not an appropriate modeling approach, hence the three steps in the simulation procedure are required.



# Chapter 5

## Results

In this chapter, the computational results from the FEM simulations of the SCB test and the L-flange are presented. The influence from parameters such as mesh size and viscous regularisation is evaluated for the SCB test in order to minimise their impact on the results. Furthermore, the interaction between delamination and intralaminar cracks in the simulation is studied in detailed. The computational results from both models are compared with the experiments presented in chapter 2, and based on this, the modeling approach is evaluated.

### 5.1 Computational results from the single cantilever beam simulations

The FEM model of the SCB test is simulated by employing the strategy presented in section 4.7. By doing so, an adequate crack domain is assigned in which the delamination migration successfully takes place. The three different load configurations generate the same series of fracture events which are here explained for the case  $L = 1.1a_0$ . The presented model is simulated with a mesh where the characteristic element length  $l_e = 0.05$  mm and the viscosity parameter  $\mu = 1 \cdot 10^{-6}$  s. The motivation for using this mesh and viscosity parameter is further explained in the following sections.

The force-displacement response measured at the load introduction point can be seen in Fig. 5.1, and the corresponding position of the crack tip along the crack path is shown in Fig. 5.2. The force increases linearly until the maximum load of the system is reached at the point A, where  $P = 306.2$  N and the displacement  $U_2 = 0.7501$  mm. Up to this point no crack growth takes place, and a cohesive zone gradually develops

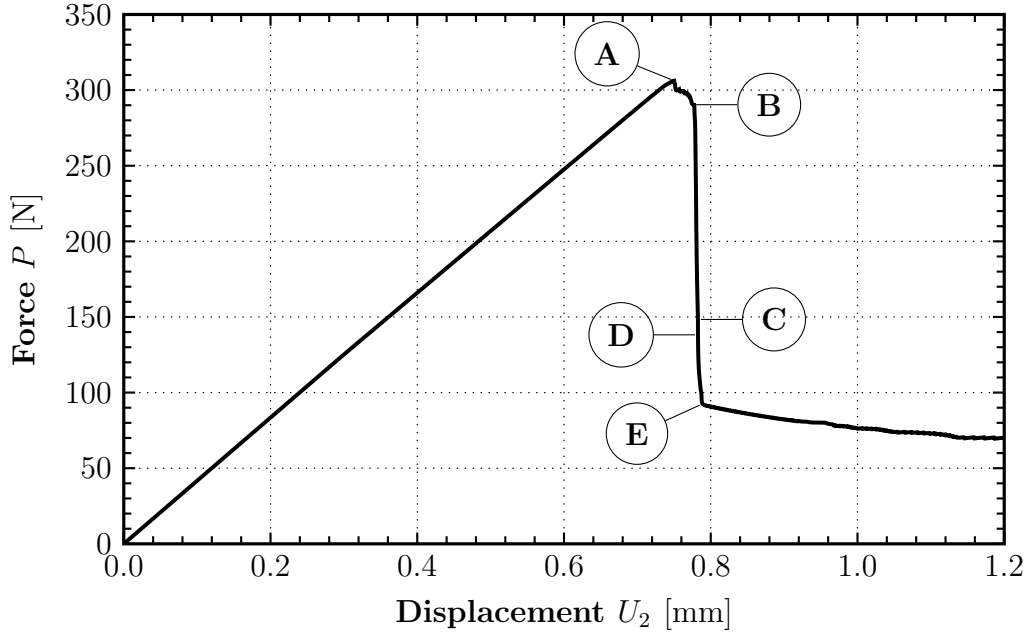


**Figure 5.1.** *The force-displacement response in the SCB simulation for the case  $L = 1.1a_0$  where the key fracture events are indicated as point A-E.*

in front of the pre-crack with the tip located at point A in Fig. 5.2.

Between point A and B, stable delamination growth starts from the initial crack tip and the load decreases. At point B, the crack tip is located almost underneath the load introduction point, corresponding to a displacement of  $U_2 = 0.7745$  mm and the propagation of the delamination becomes unstable. During the unstable fracture event, the delamination front reaches a point where the crack initiation criterion is satisfied in the adjacent continuum elements, indicated as C. An intralaminar crack starts to propagate through the crack domain in the ply along a path represented by the level-set in the activated enriched elements and delamination stops. At the point D, the crack reaches the next ply interface and triggers a new delamination. The delamination continues to propagate unstable until point E, which corresponds to the deformed state depicted in Fig. 5.2. The force at this instance is  $P = 92.5$  N. Further loading until the final displacement  $U_2 = 1.2$  mm results in stable delamination growth.

The migration event and the delamination initiation in the second interface occurs during unstable crack propagation and has no visible effect on the force-displacement response. Delamination migration takes place at the distance 12.9 mm, measured in the horizontal direction from the load introduction point to where the intralaminar crack initiates. A detailed picture of the predicted path for the matrix crack that

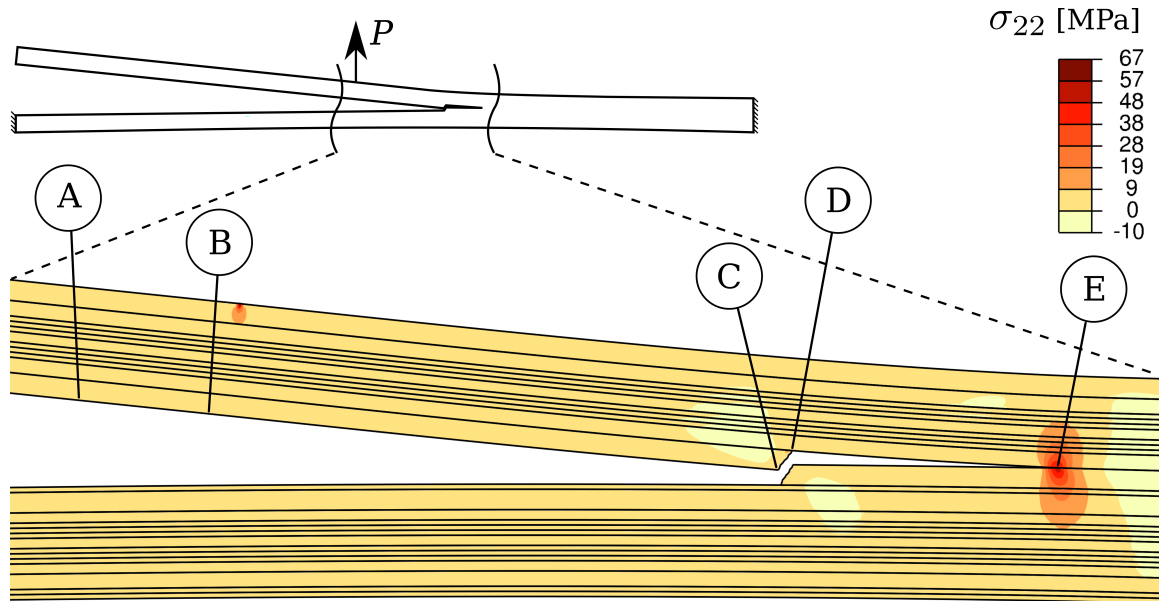


**Figure 5.2.** The deformed SCB model for  $L = 1.1a_0$  at the state where stable delamination starts in the second interface. The stress  $\sigma_{22}$  is represented by the contour plot and the crack tip position at the key fracture events is indicated along the crack path at point A-E. The displacements are scaled with a factor 3.

propagates through the continuum elements during migration can be seen in Fig. 5.3. The crack angle, defined in the figure as  $\alpha$ , is measured to  $55^\circ$ . This definition of  $\alpha$  originates from the crack angle measured in the experiments in [33], where the same angle was measured to  $47^\circ$ - $65^\circ$  for  $L = 1.1a_0$ . However, in both the numerical model and the experiments the measurement is slightly subjective since the crack path is not a straight line. Hence, the number of elements over the thickness that are used to estimate the angle have a clear influence, but is in the present work done as indicated

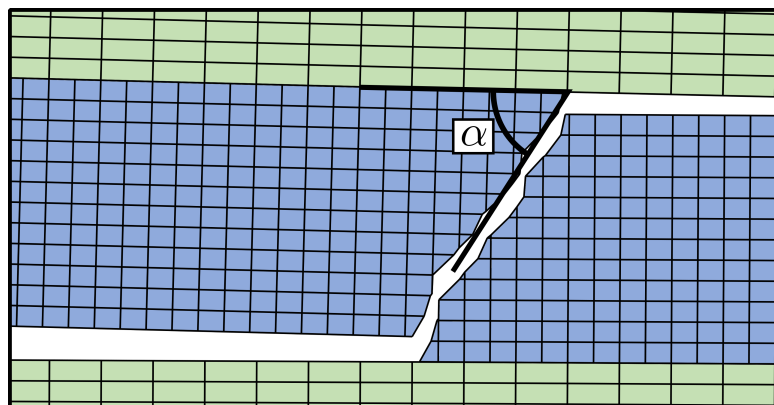


**Figure 5.3.** The predicted intralaminar crack path and the migration angle  $\alpha$  in the simulation of the SCB test for the case  $L = 1.1a_0$ .

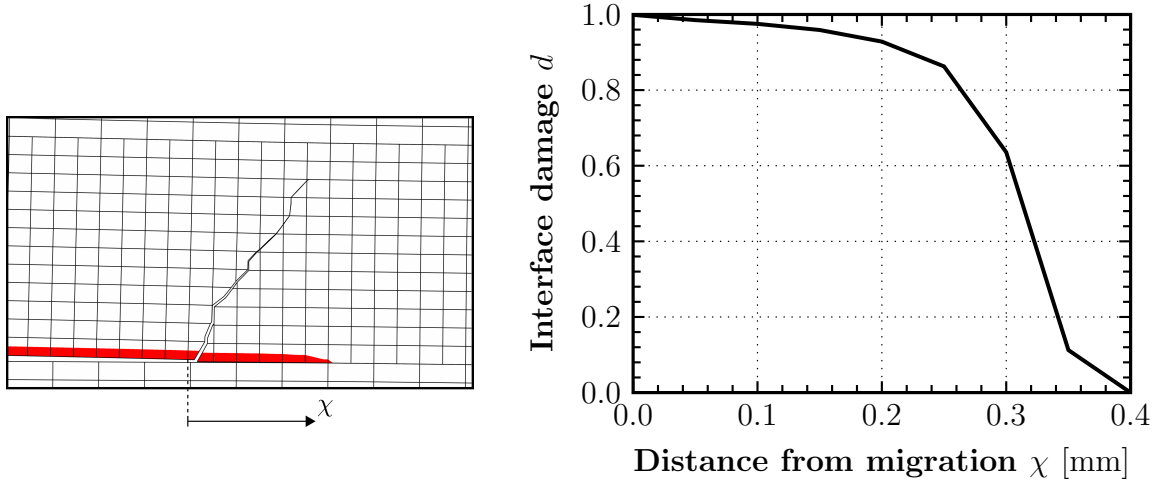


**Figure 5.4.** *Damage in the ply interface ahead of the delamination after initiation of the intralaminar crack. The coordinate  $\chi$  describes the distance from the migration location.*

in Fig. 5.3.

From the migration point where the intralaminar crack starts, the damage in the ply interface increases further ahead of the delamination tip, but without reaching complete failure. This can be seen in Fig. 5.4 where the coordinate  $\chi = 0$  at the first node to the left of the initiated migration path. The length of the damaged zone is 0.4 mm which corresponds to  $8l_e$ . This zone is shorter than the cohesive zone length for the propagating interface crack before migration, which indicates that damage progression in the ply interface has stopped or decreased after initiation of the intralaminar crack. It is most likely due to the reduced stiffness caused by the ply crack that cuts the continuum elements. A consequence of this observation is that the cohesive zone in front of the crack tip branches while the crack kinks out of the ply interface and into the ply. It is difficult to conclude if this has some physical correlation, but it may be reasonable to suggest that the phenomena seen in Fig 5.4 mainly occurs due to the applied crack discretisation. Furthermore, this points out a possible weakness with not having any direct coupling between fracture criteria for inter- and intralaminar cracks in the presented modeling approach.

The observed intralaminar crack path, represented by the XFEM discretisation can be seen for the failed and the partially failed ply in Fig. 5.3 and Fig. 5.4. As the predicted path slightly changes for every cracked element, there is reason to believe that the mesh has an impact. However, the first order elements that are applied can only represent straight crack segments, which naturally introduces the sharp kinks. If higher order elements would have been used instead, a more accurate prediction of

the crack path could possibly be achieved.

An additional factor to consider is that once a crack has been initiated in a continuum element, the mode-mix ratio  $\beta$  remains fixed. If the stress state changes, the ability to propagate is affected. This probably happens at the last steep part of the intralaminar crack path as onset of degradation of the second ply interface, to which the delamination migrates, takes place prior to completed migration. However, this has a minor impact on the result and the effect can be neglected in this case.

### 5.1.1 Mesh sensitivity

A mesh sensitivity analysis is carried out to evaluate the mesh dependency in the simulations. The SCB model is discretised with four different meshes in order to find an adequate element size that can represent the structural behaviour and the tractions in the cohesive zone with sufficient accuracy. Based on the estimated length of the cohesive in section 4.3.1, the characteristic elements lengths  $l_e = \{0.5, 0.1, 0.05, 0.025\}$  mm are simulated.

The force-displacement response for each mesh is shown in Fig. 5.5. For simplicity, only delamination in the first interface is considered here. In the simulation with the coarsest discretisation, the maximum load is clearly overestimated. A small load drop is observed during the loading stage, but the unstable event does not occur until  $U_2 = 0.9056$  mm. When using a finer mesh for  $l_e = 0.1$  mm and  $l_e = 0.05$  mm, the force-displacement responses are very similar. The initially stable delamination after the maximum load is reached is more distinguishable, which can be a consequence of using more elements along the cohesive zone and over the ply thickness. The most refined mesh with  $l_e = 0.025$  mm follows almost identically the force-displacement response for the mesh with  $l_e = 0.05$  mm.

The interlaminar shear traction and the normal traction in the cohesive zone in front of the initial delamination tip is shown in Fig. 5.6 for the four different discretisations. At this instance, the load is  $P = 247.7$  N and the displacement  $U_2 = 0.6$  mm, which is before the crack propagation starts. For the mesh where  $l_e = 0.5$  mm, the stresses are barely captured, which can explain why the maximum load in the force-displacement response is much higher for this case. The two finest discretisations are yet again almost identical in their representation of the stresses. Also for  $l_e = 0.1$  mm a similar stress distribution is obtained, although it is not able to capture the maximum shear- or normal stress.

The number of degrees of freedom in the mesh that each characteristic element length results in is presented in table 5.1, where the number of elements over the

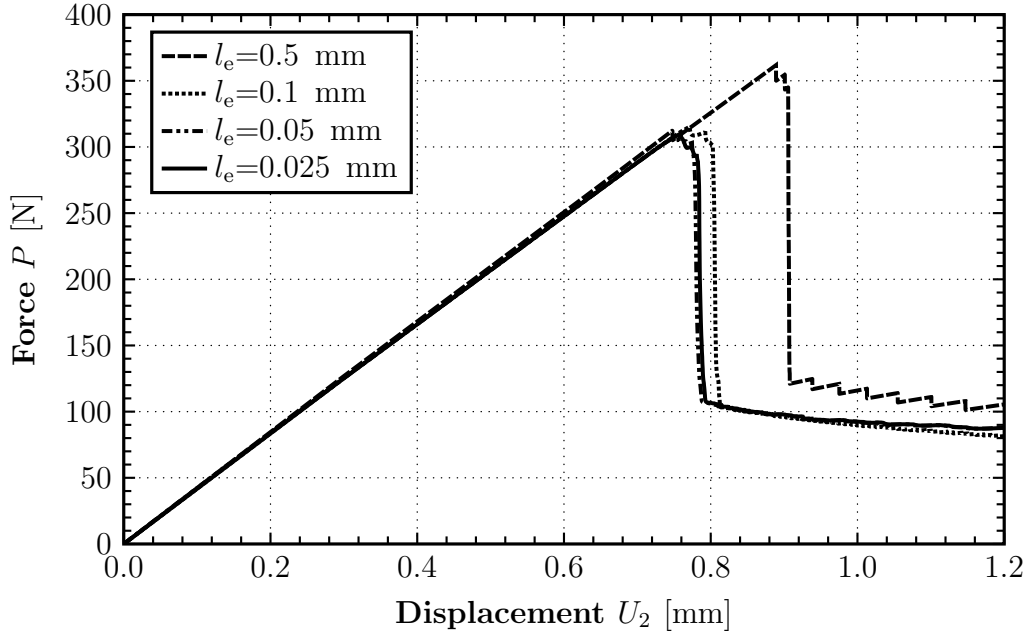


**Figure 5.5.** *The force-displacement response for the four different meshes corresponding to the characteristic element length  $l_e$  in the mesh sensitivity study for the SCB model where  $L = 1.1a_0$ . Only delamination in the first interface is considered.*

ply thickness also is given. Based on the results with different discretisations and their corresponding mesh size, the element length  $l_e = 0.05$  mm is chosen for the simulations in the present work. The force-displacement response and the interlaminar stress distribution is nearly identical to the finer mesh, but the number of degrees of freedom is reduced with over 30%. Moreover, by using an even coarser mesh the physics of the problem is not captured accurately enough. It would also result in fewer elements over the ply thickness, which may compromise the intralaminar crack path predicted when employing the XFEM. For the SCB model the length of the cohesive zone, i.e. from where the damage variable  $d = 1$  to where  $d = 0$  is measured

**Table 5.1.** *Comparison between the degrees of freedom and elements over the ply thickness for the different mesh sizes, corresponding to the characteristic element length  $l_e$ .*

$l_e$ [mm]	Degrees of freedom	Elements/ply-thickness
0.5	22,990	1
0.1	123,414	2
0.05	222,250	3
0.025	333,862	4



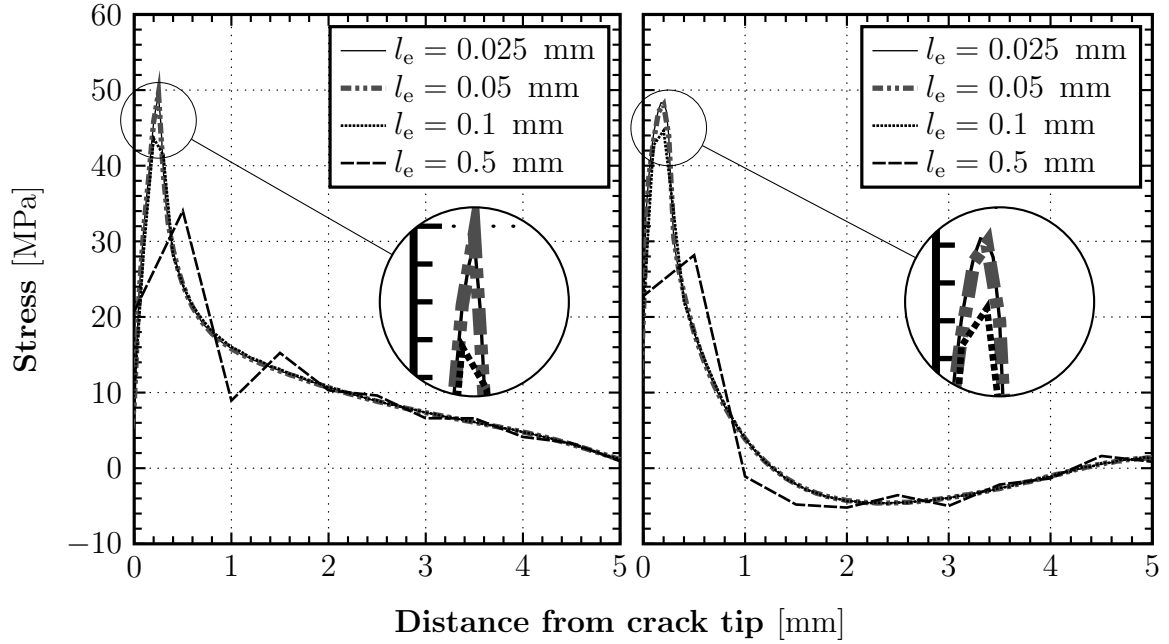


**Figure 5.6.** The shear traction  $t_s$  (left) and the normal traction  $t_n$  (right) in the ply interface in front of the initial delamination tip for  $L = 1.1a_0$  at the load  $P = 247.7$  N. The traction is calculated for the different element sizes used in the mesh sensitivity study for the SCB model.

to  $0.5 \text{ mm} \leq l_{cz} \leq 0.7 \text{ mm}$  in the ply interface, which for  $l_e = 0.05 \text{ mm}$  ensures at least 10 continuum elements subjected to the contact constraint over the cohesive zone length.

### 5.1.2 Energy evaluation

In order to further investigate the SCB model, the energy shares are calculated at each load increment. As no dynamic effects are considered and the simulated structure has no mass, the external work done on the system must be equal to the internal energy at any load state. This is true during the initial loading stage as can be seen in Fig. 5.7, where the energies are plotted over the displacement. The external work is supplied by the displacement and the reaction force  $P$ , and the internal energy is the sum of the total internal strain energy and the dissipated energy due to damage and to the viscous regularisation. The latter one is the numerical damping which is introduced through the viscous damage variable in Eq. (4.4.1). This artificial energy quantity in the model depends on the work done to separate the cohesive interfaces and on  $\mu$ , and ensures a quasi-static equilibrium path during unstable crack

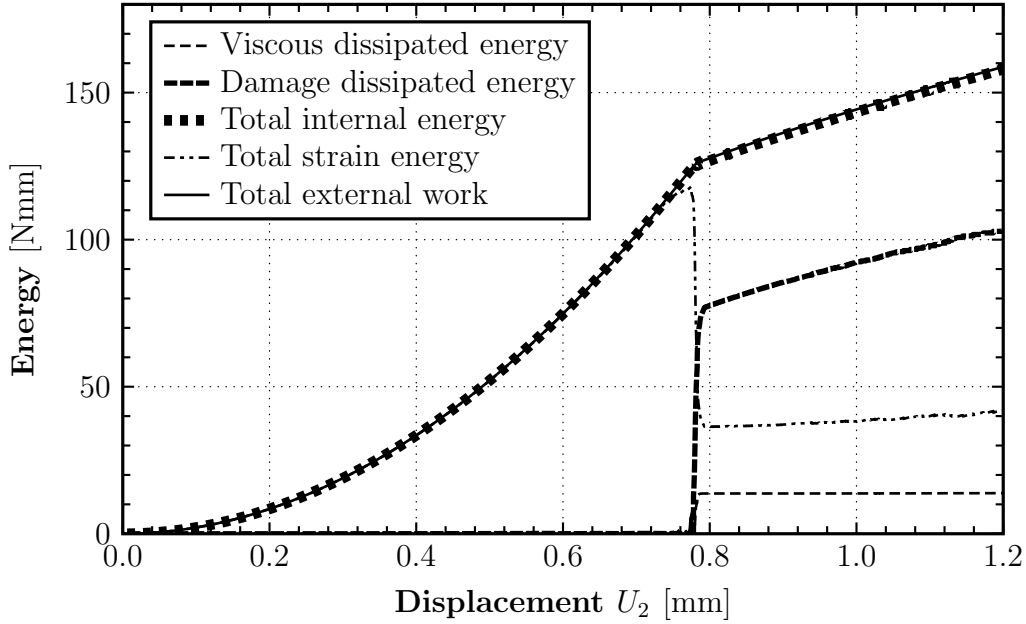


**Figure 5.7.** *The energy shares calculated at each load increment in the simulation of the SCB model for  $L = 1.1a_0$ .*

propagation. The energy can physically correspond to the effect of phenomena such as strain rate and elastic waves in the material [17]. However, in the present work the viscous regularisation is only used to approximately compensate for such effects, and to overcome convergence difficulties by making the system stable at states where the physical structure is unstable. As a consequence of the regularisation, the simulated model shows a difference between the total internal energy and the total external work after the unstable fracture event, although it is small.

The energy dissipated due to damage is quite large in comparison to the total strain energy, and mainly accumulates as the crack length increases during the stage corresponding to unstable crack propagation. Hence, the energy share dissipated due to viscous regularisation is also of significant size, which indicates that the structure may have a distinct snap-back behaviour.

### 5.1.3 The snap-back behaviour of the structure and the influence of viscous regularisation

As the load is introduced to the SCB model through a monotonically increasing displacement  $U_2$ , the force-displacement response deviates from the unstable equilibrium load path as crack propagation takes place. In order to understand the structural behaviour and to evaluate if the viscous regularisation of the system is

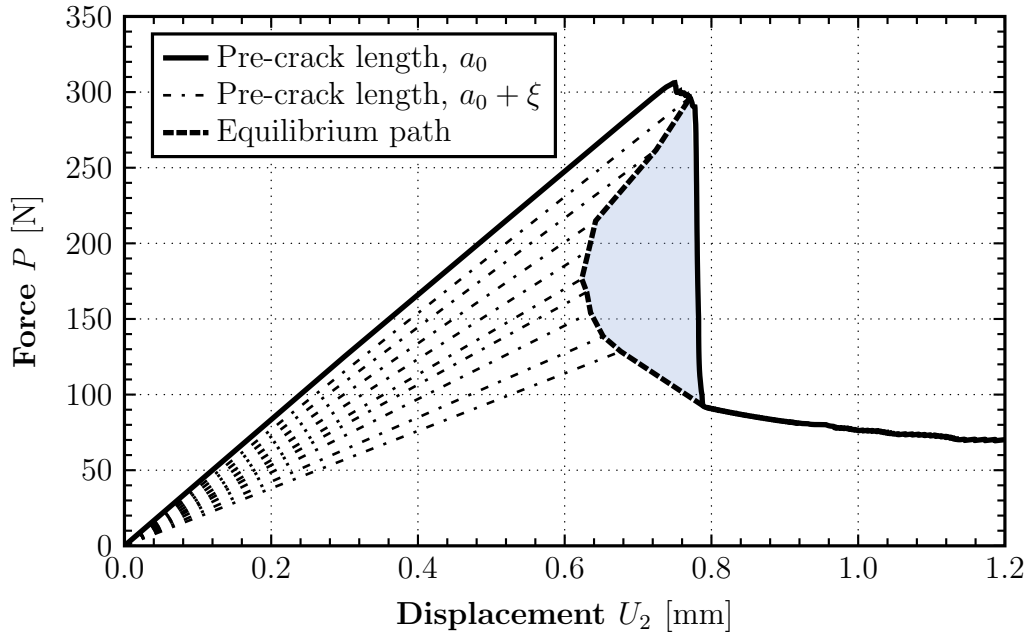


**Figure 5.8.** *The snap-back behaviour of the SCB model. By assigning different initial delamination lengths  $a_0 + \xi$ , the point before unstable crack propagation takes place is found and the approximate unstable equilibrium path can be drawn. The coloured area corresponds to the snap-back energy.*

adequate, the unstable equilibrium path is estimated. The model is simulated for different lengths of the initial interface crack  $a_0 + \xi$ , and the point before unstable crack propagation occurs can be found for each case. This is shown in Fig. 5.8, where  $\xi = \{2.0, 4.0, 6.0, 8.0, 10.0, 11.2, 13.0, 15.4, 17.8\}$  mm and  $\xi = 17.8$  mm just before migration takes place. During crack propagation with the initial interface crack length  $a_0$ , the corresponding unstable equilibrium point can thereby be found for every instance when the crack has propagated a distance  $\xi$ . The estimated path in Fig. 5.8 connects the unstable equilibrium points for the different initial crack lengths, and the snap-back behaviour of the structure is thereby visualised. The only way to hypothetically achieve such load path in practice is to continuously decrease the force and the displacement as the crack propagates.

The snap-back behaviour for the SCB model is very distinct and clearly has an impact on the failure of the structure. The indicated area that is defined by the force-displacement curve and the equilibrium path should approximately be equal to the energy dissipated due to viscous regularisation for an appropriate numerical simulation. Hence, the energy corresponding to the snap-back area is calculated from the 9 unstable equilibrium points corresponding to the initial crack lengths  $a_0 + \xi$  and the point directly after the unstable fracture event. This results in the

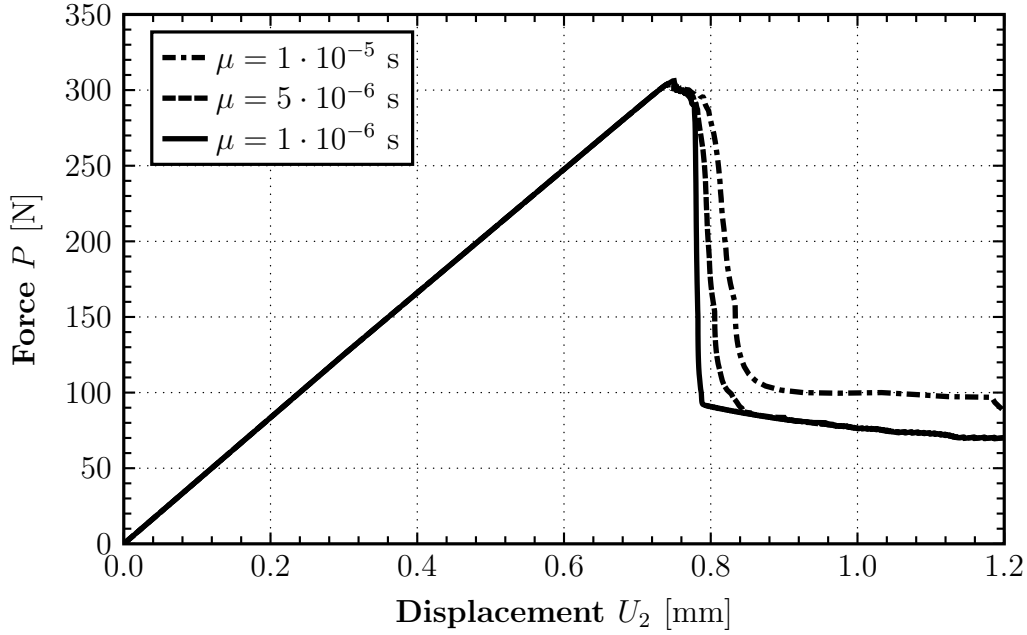


**Figure 5.9.** *The effect of the viscosity parameter  $\mu$  on the force-displacement response for the SCB model where  $L = 1.1a_0$ .*

snap-back energy 19.7 Nmm, which should be compared to the viscous dissipated energy 13.8 Nmm seen in Fig 5.7. Both energies are of the same order, and since the snap-back path is only defined by 9 points for delamination lengths in the first ply interface before migration, it is not an accurate estimation. Yet, it indicates that the viscous dissipated energy is of an appropriate magnitude.

To further evaluate the influence and the sensitivity from changing the viscous regularisation, different values of the viscosity parameter  $\mu$  are simulated. The structural response can be seen in Fig. 5.9. For a high value of  $\mu$ , the force tends to slightly overshoot, which can be directly traced back to how the viscous damage variable  $d_v$  is calculated and substituted into the stiffness matrix. This causes a slower damage progression and results in a smoother force-displacement response during the unstable fracture events. For  $\mu = 1 \cdot 10^{-5}$  s, the force is higher when the stable delamination in the second interface takes place, compared to using a lower value of  $\mu$ . This is only an effect of a shorter crack length due to slow damage progression, which results in a higher load carrying capacity of the structure at this instance. Also the delamination migration occurs for a higher load and at a larger displacement when  $\mu = 1 \cdot 10^{-5}$  s. By assigning a lower value to the viscosity parameter, the sudden drop in the force-displacement response during crack propagation tends to approach a vertical line and the overshoot effect almost disappears. This is in good agreement

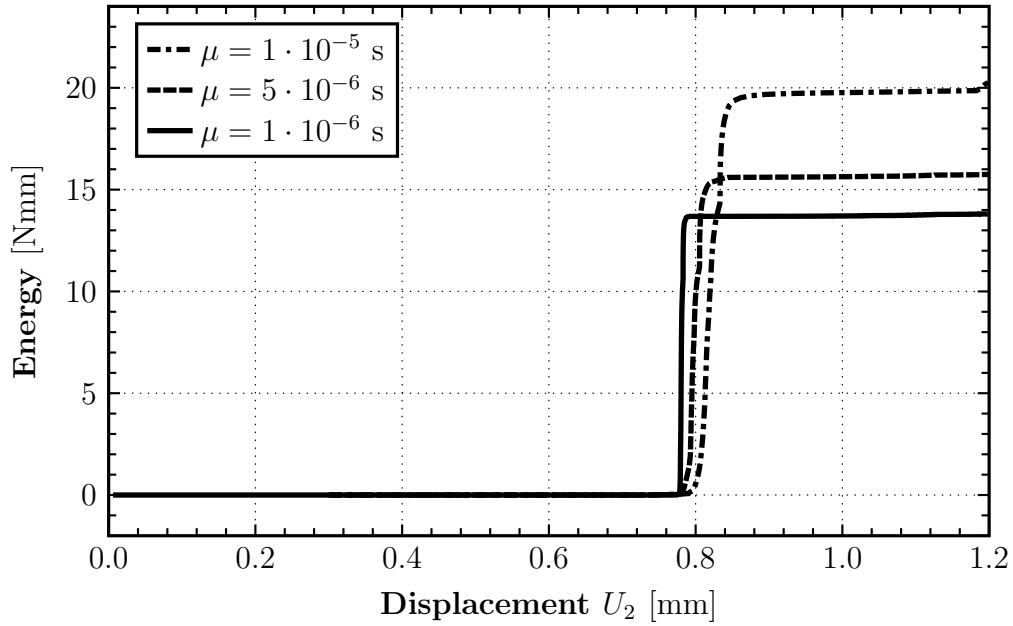


**Figure 5.10.** *The resulting viscous dissipated energy for different values of the viscosity parameter  $\mu$  in the SCB model.*

with how the system should respond when decreasing the value of  $\mu$ . However, the actual dissipated energy that this change of the viscosity parameter results in is very small. This is shown in Fig. 5.10, where the viscous dissipated energy that corresponds to the three different simulated values of  $\mu$  are plotted. By applying  $\mu = 5 \cdot 10^{-6}$  s, the dissipated energy due to viscous regularisation only increases with 14% compared to using  $\mu = 1 \cdot 10^{-6}$  s. Additionally, the computational time required for a converged solution drastically increases with a lower value of  $\mu$ . Despite this,  $\mu = 1 \cdot 10^{-6}$  s is employed for the simulations in the present work. The crack initiation criterion in the XFEM crack-domain is purely stress based, and overshooting loads caused by the regularised damage progression of the delamination may affect the stress state in the element where the intralaminar crack nucleates. This can lead to premature initiation of the XFEM crack and an insufficient prediction of its direction, which affects the delamination migration. Although a higher value of  $\mu$  clearly can be used, the objective of this thesis is to predict the fracture events as accurately as possible and not primarily to optimise the computational expenses.

### 5.1.4 Comparison between simulation and experiment for the SCB test

In order to evaluate the performance of the SCB simulation in the present work, some of the key results are compared to the SCB test in [33]. The general behaviour of the FEM model is similar to the experiment in terms of fracture events and unstable crack propagation. Delamination migration is successfully simulated for all three load cases under the assumption that no intralaminar cracks initiate before they are able to propagate completely through a whole ply. The FEM model is discretised with  $l_e = 0.05$  mm, and a viscosity parameter  $\mu = 1 \cdot 10^{-6}$  s is applied as discussed in the previous sections. In Appendix A, all extracted data from the experimental results in [33] can be found from which the graphical representations in this section are generated.

The simulated force-displacement response is plotted in Fig. 5.11 together with the experimentally measured response in [33]. For all three load cases the force increases linearly until damage is initiated. Moreover, the linear elastic stiffness of the structure is much higher in the FEM model than in the experiments, which can be seen in table 5.2. The structure's stiffness is overpredicted with about 40-55% which clearly should have a significant impact on the results. As the maximum load is reached, the displacement  $U_2$  is smaller in the simulations, which can be a consequence of the stiffer elastic response. The maximum value of the force  $P$  during the loading scenario is presented in table 5.3. For  $L = 1.1a_0$  and  $L = 1.2a_0$ , the difference in the maximum load between simulation and experiment is relatively small. This indicates that even though the stiffness is higher, the interface damage is initiated at approximately the same load magnitude. Since the damage initiation criterion in the ply interface is evaluated from the local contact traction in front of the of the initial delamination tip, it may not be very dependent on the deflection at the load application point. This can explain the relatively small difference in maximum load between simulation and

**Table 5.2.** *The linear elastic stiffness of the SCB model in the present work, compared with the experiments in [33] for three different load configurations.*

	$L = 1.1a_0$	$L = 1.2a_0$	$L = 1.3a_0$
Experiment	291.92 N/mm	337.39 N/mm	381.92 N/mm
Simulation	412.20 N/mm	488.94 N/mm	588.62 N/mm
Ratio	1.41	1.45	1.54

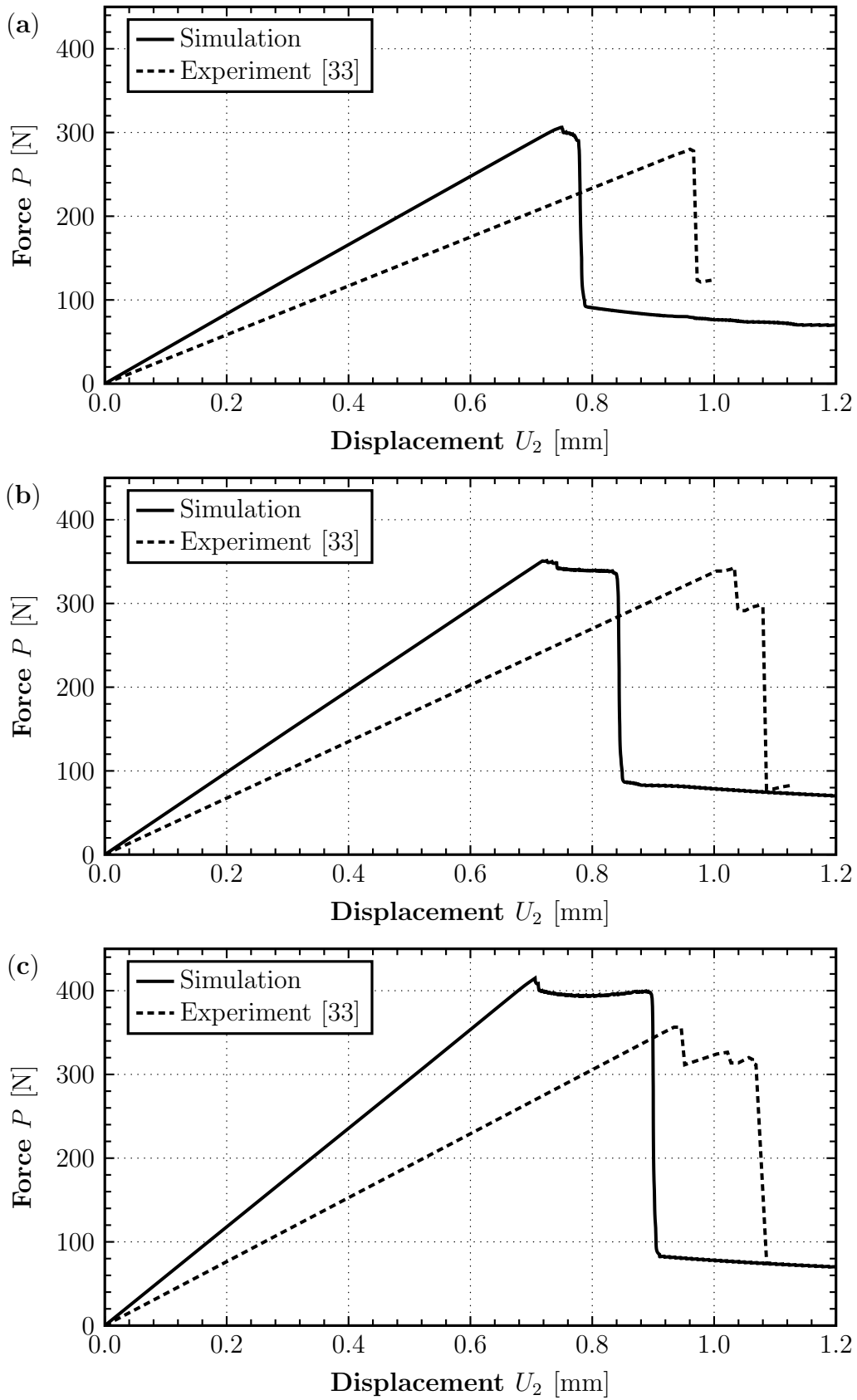


**Figure 5.11.** The force-displacement response at the load application point for the SCB model in the present work and from the experiments in [33], where (a)  $L = 1.1a_0$ , (b)  $L = 1.2a_0$  and (c)  $L = 1.3a_0$ .

experiment.

The shape of the force-displacement curves in Fig. 5.11 (b)–(c) differs from the experimental curves in the region between where the maximum force is reached, and where unstable crack propagation takes place. At this stage, stable delamination growth is detected in the simulations while more sudden load drops are observed in the experiments. A possible explanation to this can be that the mesh may not be able to transfer the shear stress across the ply interfaces accurately enough, and that it thereby is related to the discretisation. It can also be an effect caused by dynamic effects or the micro-structure of the physical laminate.

According to the fractography examination of a specimen where  $L = 1.3a_0$  in [33], the delamination propagates partially in mode II at this stage. It is also observed that the crack tends to kink into the  $0^\circ$ -ply, but is prevented to do so due to the presence of the actual fibers, forcing the crack to continue in the interface. This effect cannot be captured by the FEM model in the present work, but may be a contributing factor to the difference in the shape of the force-displacement curves.

As the simulated structure shows a higher linear elastic stiffness and fails at a lower displacement than the laminates in the experiment, the total potential energy in the system shortly before the unstable crack propagation takes place is compared. For the FEM model the potential energy is the total recoverable strain energy, presented in Fig. 5.7. From the experiments, this can approximately be calculated from the force-displacement curve, based on the data provided in Appendix A. The potential energies at this instance can be seen in table 5.4. The largest difference is observed for  $L = 1.1a_0$ , and the deviation from the experiment is between 5-15%. A possible explanation to this can be the effect of the relatively long stable delamination growth in the FEM model before unstable fracture as mentioned before. This results in a reduction of the total increasing strain energy due to the energy dissipated during crack propagation. However, the difference is within an acceptable range,

**Table 5.3.** *The predicted maximum force from the force-displacement response in the SCB model in the present work, compared with the experiments in [33] for the three different load configurations.*

	$L = 1.1a_0$	$L = 1.2a_0$	$L = 1.3a_0$
Experiment	280.0 N	343.0 N	356.4 N
Simulation	306.2 N	351.1 N	414.9 N
Difference	+26.2 N	+8.1 N	+58.5 N



**Table 5.4.** *The potential energy in the system before unstable crack propagation. The SCB model in the present work is compared with the experiments in [33] for the three different load configurations.*

	$L = 1.1a_0$	$L = 1.2a_0$	$L = 1.3a_0$
Experiment	134.3 Nmm	159.7 Nmm	169.0 Nmm
Simulation	114.8 Nmm	140.8 Nmm	178.0 Nmm
Difference	-19.5 Nmm	-18.5 Nmm	+9 Nmm

considering the approximative method of calculating the potential energy directly from the experimental force-displacement data.

An important parameter that can be predicted in the simulations is the location where the delamination migration takes place. The procedure for finding this position along the first ply interface is described in section 4.7. The migration location is measured as the horizontal distance between the load application point and where the intralaminar crack initiates. In Fig. 5.12, the migration location predicted by the FEM model is compared to the experiments from [33]. The load offset relates to the experimental data as the relation  $L/a_0$  was not identical for each load case in practice.

From Fig. 5.12 it can be concluded that the predicted migration distance is in good agreement with the experimental results. All predictions are within the same range as the test results in [33], and follows the implied tendency that the migration occurs closer to the load application point as the offset increases. However, the scatter in the experimental data for each load case is relatively high. Consequently, more test results would be required to make a detailed quantitative analysis of the accuracy in the prediction.

The migration angle  $\alpha$  from the simulated SCB model is compared to the experiments in Fig. 5.13 for each load offset. The predicted angles are within the same range as the ones obtained in the test in [33]. As it may be reasonable to expect that  $0^\circ \leq \alpha \leq 90^\circ$  due to the geometry, the experimental results are spread out over a relatively large interval, which makes it difficult to draw any general conclusions regarding the predicted angle. Furthermore, the intralaminar crack path seen in Fig. 2.4 gradually changes its direction from parallel to the ply interface until the migration angle  $\alpha$  is reached. This is not observed in the simulation, where the intralaminar crack is initiated with a much steeper path as in Fig. 5.3. Consequently, the modeling approach in the present work, combining continuum elements with homogenised material properties and a contact formulation, may not be able to

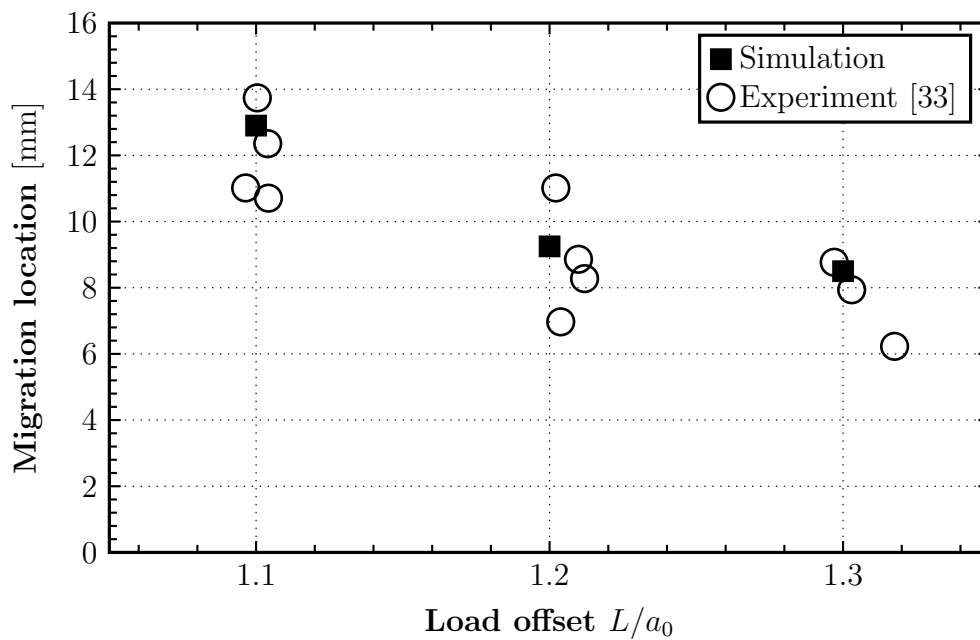


**Figure 5.12.** Comparison between the predicted migration location in the simulations of the SCB model and the experimental results in [33]. The migration location is defined as the horizontal distance to the load application point which is predicted to 12.90 mm, 9.25 mm and 8.50 mm for each load case respectively.

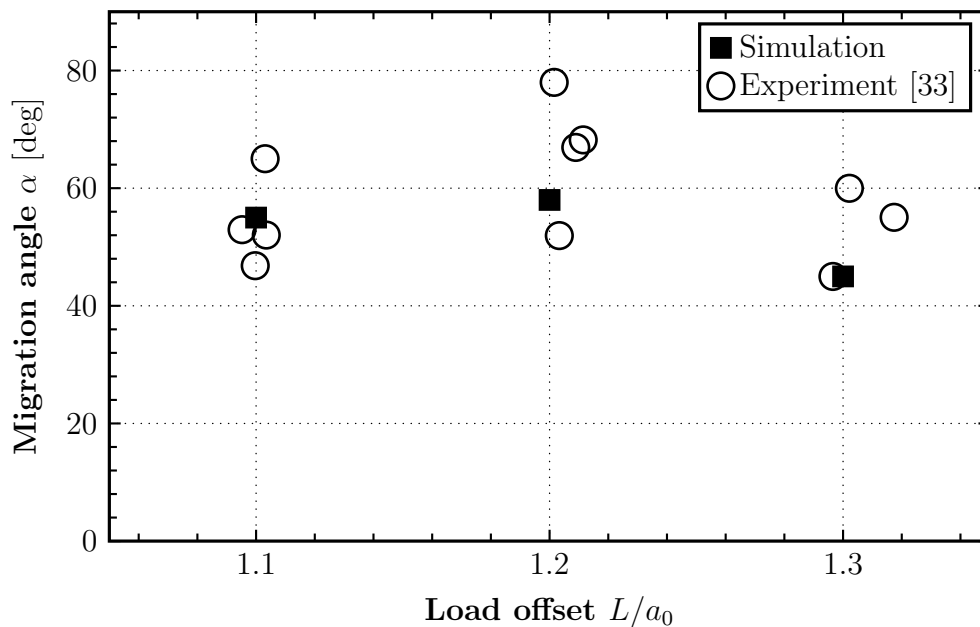


**Figure 5.13.** Comparison between the predicted migration angle  $\alpha$  in the SCB model and the experimental results in [33]. The angle is predicted to 55°, 58° and 45° for each load case respectively.

capture the complete interaction between inter- and intralaminar cracks properly. However, the difference between crack paths is related to the predicted direction of the ply crack that cuts the first continuum element, as the rest of the path is in agreement with the experiments.

## 5.2 Computational results from the L-flange simulation

Similarly to the SCB model, a mesh sensitivity study and an evaluation of the viscous regularisation energy for different values of  $\mu$  is carried out for the L-flange model. Based on the same criteria as discussed in 5.1.1 and 5.1.3 the characteristic element length  $l_e = 0.05$  mm and the viscosity parameter  $\mu = 1 \cdot 10^{-5}$  s is employed.

The general behaviour in terms of fracture events and load response in the simulation is similar to the experiments in [37], and the location for delamination migration is predicted by applying the simulation strategy described in section 4.7. The force-displacement response of the L-flange model can be seen in Fig. 5.14, and the failed structure with the predicted crack path is shown in Fig. 5.15. The key fracture events are indicated as point A-C in both figures.

The force  $P$  increases linearly as the pristine undamaged structure is loaded. At point A, when  $P = 623.5$  N and  $U_2 = 2.0467$  mm, delamination emerges in the curved part of the laminate and the load instantly drops. The initial detected length of delamination is 0.31 mm, from which it increases in size. Mainly normal traction causes the interface to fail where delamination emerges, which indicates that mode I is the dominating fracture mode. A 1.6-2.0 mm long cohesive zone is initiated ahead of each crack tip along the ply interface. As the delamination propagates, the length of the cohesive zone is shorter and remains approximately constant at  $l_{cz} = 1$  mm. This indicates that the longer cohesive process zone where the delamination emerges is an effect of high interlaminar traction in this region prior to local failure of the interface.

At point B, the intralaminar ply crack initiates. This happens where the curved part of the structure ends and transitions into the straight section, and the delamination gradually changes to be more mode II-dominated. The migration location is described by the angle  $\theta_m$  in Fig. 5.15. As the intralaminar crack propagates and reaches the next ply interface at point C, delamination is initiated and continues to propagate in this interface. All fracture events from point A-C occur unstable, and the migration event cannot be detected in the force-displacement response. The complete unstable load drop ends as  $P = 277.1$  N where  $U_2 = 2.0561$  mm, as seen

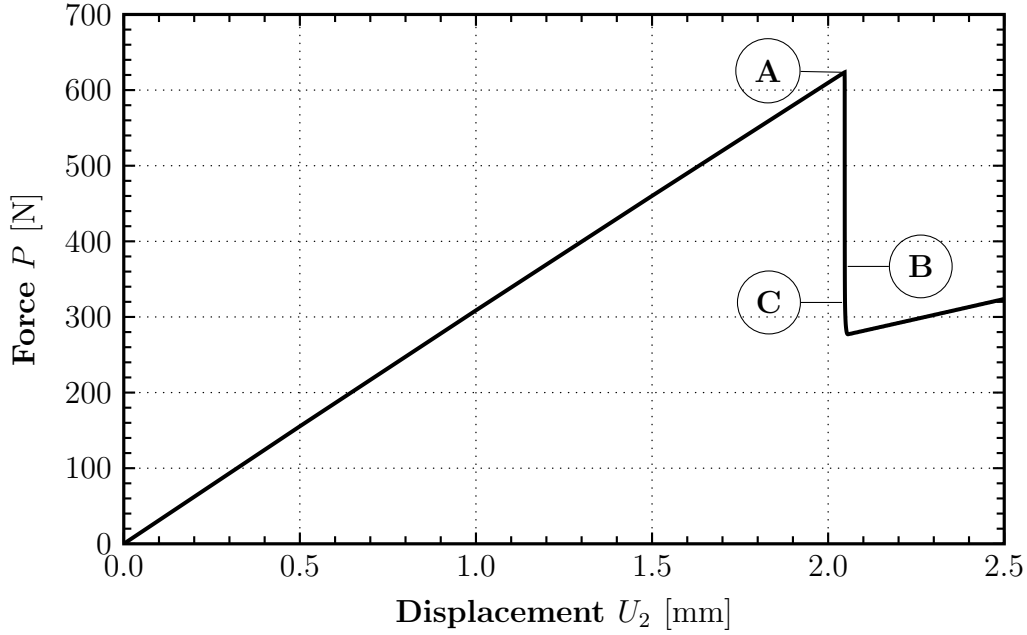


**Figure 5.14.** *The force-displacement response from the L-flange simulation.*

in Fig. 5.14. Eventually the migrated delamination becomes stable and continues to propagate as the displacement increases.

As discussed in [37] and [29], the snap-back behaviour of the L-flange is significant, which necessitates a relatively high amount of viscous regularisation to be applied in order to achieve a converging simulation. The emergence, propagation and migration of the delamination is thereby very unstable and dynamic effects, which are not considered in the model, may have a large impact in practice.

In Fig. 5.16 (a), the shear stress in the plies around the delamination front is shown prior to initiation of the intralaminar crack. The negative sign of the shear stress in the  $90^\circ$ -ply promotes the interface crack to kink into this ply. The corresponding maximum principle stress in the  $90^\circ$ -ply close to the delamination front is above 82 MPa, which is the transverse tensile strength of the material, and an intralaminar crack could thereby be initiated in the continuum elements here. However, the crack driving force at this instance, i.e. the strain energy release rate, makes it more energetically favourable to continue to propagate in the ply interface. An intralaminar crack, represented by the XFEM would at this point only initiate in a few elements before it stops. As the assumption is made that the crack can only initiate at a location where it causes complete delamination migration, this behaviour is suppressed as described in section 4.7. Consequently, this shows a weakness of the modeling approach since the stress in the  $90^\circ$ -ply may exceed the strength of the material in a

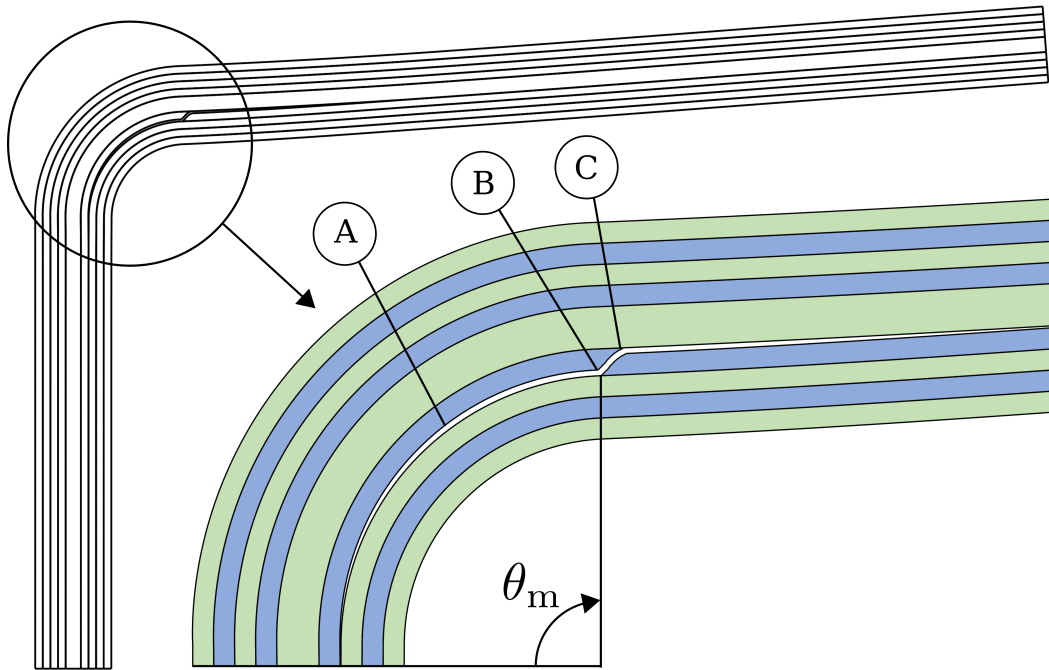


**Figure 5.15.** The failed L-flange model and the predicted crack path as  $U_2 = 2.5$  mm, where A-C indicate some of the key fracture events and  $\theta_m$  describes the position of the delamination migration.

limited region close to the delamination front, but is not accounted for unless it occurs in a pre-defined crack domain.

The intralaminar crack, partially propagated through the  $90^\circ$ -ply during delamination migration can be seen in Fig. 5.16 (b). The first elements cut by the crack path have failed completely and contain a crack interface degraded to zero stiffness, hence the physical crack face can be realised. Damage is initiated along the crack path ahead of the physical crack tip, and results in a cohesive process zone, stretching over 10 elements in the ply thickness direction. In the ply interface, damage progresses 0.65 mm or  $13l_e$  after of the point of migration, similar to Fig. 5.4 for the SCB model.

When simulating delamination migration in the curved region of the L-flange, it becomes clear that the element shape is crucial for XFEM to work properly. A crack in a pristine undamaged crack domain must always pass through the centre of the first element where it nucleates in *Abaqus/Standard*. As the mode of fracture changes relative to the ply interface during propagation in the curvature, the kink angle at migration depends on the migration location. If the kink angle  $\alpha_L$ , defined in Fig. 5.16 (b) is small, it will geometrically be very difficult to make sure that the initiated crack path starts from the ply interface if rectangular elements with an aspect ratio close to 1 are used. However, for the present simulation  $\alpha_L = 44^\circ$ , and an appropriate aspect

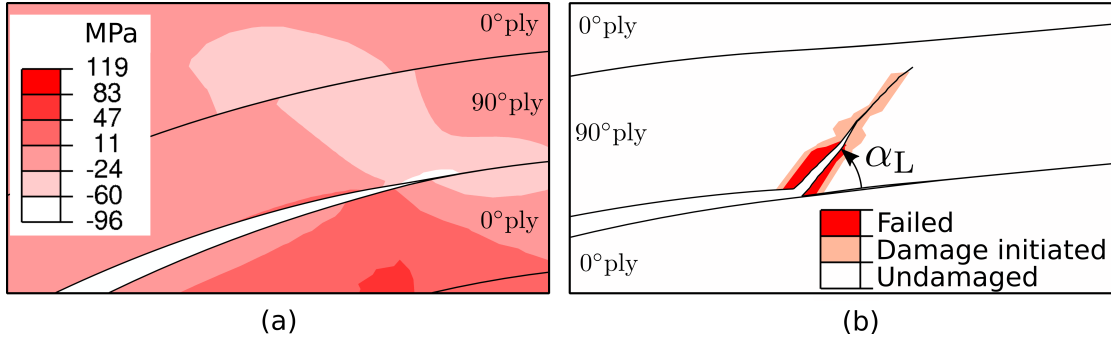


**Figure 5.16.** (a) The ply shear stress around the delamination front prior to migration and (b) the damage status in the crack interface along the intralaminar crack path during migration, represented by the XFEM. Displacements are scaled with a factor 2.

ratio can thereby be maintained.

### 5.2.1 Comparison between simulation and experiment for the L-flange

The simulation results from the L-flange is compared to the experiments in [37] in order to evaluate the performance and the accuracy of the prediction. Three specimens are tested in the experiment and the recorded force-displacement response can be seen in Fig. 5.17 together with the predicted response in the present work. The extracted force-displacement data from [37] can be found in Appendix B.

The series of fracture events take place in the same order in the simulation as in the experiments, and the delamination migration occurs under unstable crack propagation. However, the main difference is that failure takes place at a smaller displacement and the elastic stiffness of the structure is overpredicted by 12-26%, as can be seen in table 5.5. This can be related to the simplified boundary conditions

**Table 5.5.** Comparison of key parameters between the simulation of the L-flange model in the present work and the experiments in [37]. The range indicated for the experiment describes the lowest and the highest value found from the three specimens.

	Simulation	Experiment [37]
Structural stiffness [N/mm]	304.6	241.8 – 271.3
Maximum load [N]	623.5	647.6 – 690.8
Potential energy [Nmm]	638	772.9 – 977.3

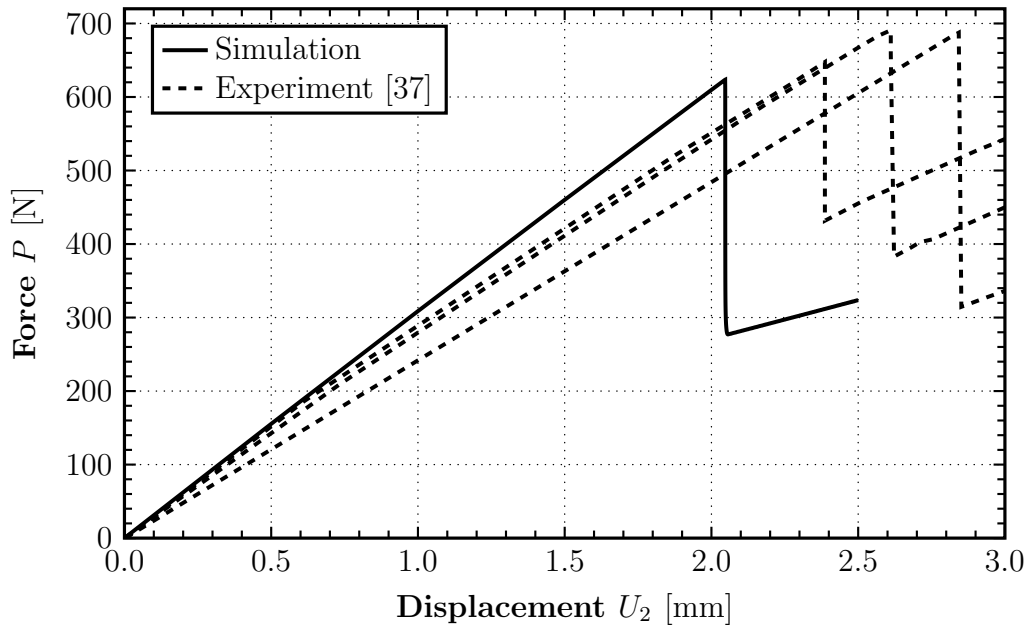


**Figure 5.17.** A comparison of the force-displacement response between the three tested specimens in [37] and the simulated response in the present work.

in the model where the contact between the loading device and the upper vertical leg of the L-flange is represented only by fixing the nodes in the horizontal direction. On the other hand, the elastic stiffness of the three test specimens deviate quite a lot from each other. According to [37], this has to do with a non-uniform thickness of the laminate and that the vertical leg in practice was slightly wedge-shaped, making it complicated to clamp it properly to the loading device. Additionally, some slipping between the loading device and the laminate is reported, which clearly can result in a lower measured stiffness compared to when applying the idealised boundary conditions in the FEM model.

The predicted maximum load in the force-displacement response is lower than in the experiments and takes place earlier at a smaller displacement. Consequently, the potential energy in the system just before unstable crack propagation is less, which can be seen in table 5.5.

By comparing the predicted crack path in Fig. 5.15 with the picture presented in the introduction of the experiment in Fig. 2.6, a difference in the migration location can be observed. In the prediction,  $\theta_m = 89^\circ$ , and in [37] the migration seems to be located closer to the centre of the curved part. However, as the exact location is not documented, the difference cannot be further quantified. Nonetheless, the shape of the intralaminar crack, represented through the XFEM in the model, has a very similar path to the test specimen.

### 5.2.2 The effect of interface strength and toughness

Due to the difficulties associated with accurate measurement of interface properties in FRPs, an analysis of the impact from changing these properties is performed on the L-flange. Additionally, it gives further insight in how small changes can affect the structure, which may explain some of the differences between the prediction in the present work and the experiment. The nominal interface properties are the ones given in table 4.4. In the analysis, the normal interface strength  $\hat{t}_n$  and the critical strain energy release rate  $\mathcal{G}_{Ic}$  for the interface is increased by 10-30%, while  $t_s$  and  $\mathcal{G}_{IIc}$  remains unchanged. A 30% increase of the normal interface strength yields  $\hat{t}_n = 78$  MPa which is still less than the transverse strength of the ply material  $R_{22}^t = 82$  MPa.

The resulting force-displacement response can be seen in Fig. 5.18. Evidently, increasing the strength and toughness has no effect on the elastic stiffness of the structure. The load carrying capacity is increased, as the unstable fracture occurs at a higher force and larger displacement. Furthermore, the shape of the curve is identical for all four cases, and after the unstable fracture event where stable delamination takes place, the load paths eventually coincide. This means that the loss of recoverable strain energy is higher with a stronger interface, hence the snap-back behaviour is also more pronounced and a higher amount of viscous regularisation is required.

An interesting effect of enhancing the interface properties is that the crack path slightly changes. It is a clear trend that delamination migration takes place earlier with a higher strength and toughness of the ply interface, which can be seen in table 5.6. Moreover, the difference in strength and critical strain energy release rate in absolute values between the simulations is not very big, considering how the parameters are measured in practice. This may contribute to explain the different migration location found in the simulation with nominal interface properties and in the experiment. The implication is supported by the fact that the potential energy in the simulation before

**Table 5.6.** *The relation between enhanced normal interface properties and the predicted location for delamination migration in the L-flange.*

Interface modification	$\hat{t}_n$	$\mathcal{G}_{Ic}$	$\theta_m$
Nominal	60 MPa	133 J/m <sup>2</sup>	89°
Nominal +10%	66 MPa	146 J/m <sup>2</sup>	87°
Nominal +20%	72 MPa	160 J/m <sup>2</sup>	81°
Nominal +30%	78 MPa	173 J/m <sup>2</sup>	78°



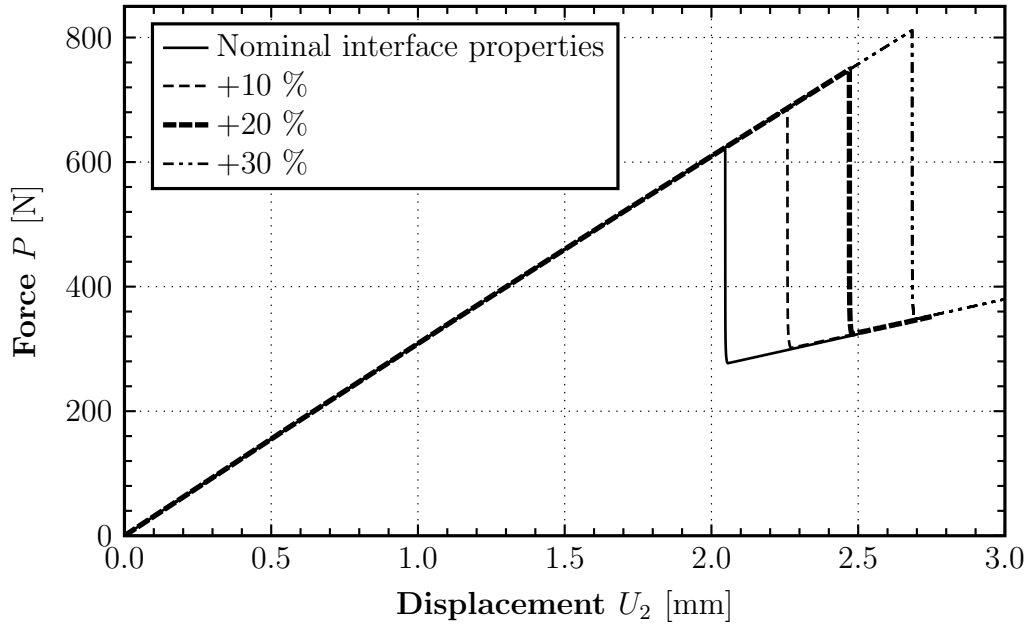


**Figure 5.18.** *The effect on the predicted force-displacement response of the L-flange from increasing the normal strength and the critical strain energy release rate for mode I in the ply interface, compared to the nominal interface properties given in table 4.4.*

unstable crack propagation takes place is significantly lower than in the experiment.

The relationship between the critical strain energy release rate in the ply interface and in the ply where the intralaminar crack initiates is affected by enhancing the interface properties. Consequently, it may energetically be more favourable for the intralaminar crack to propagate at an earlier stage when the interface toughness is increased. This is in agreement with the condition for when a crack kinks out of a bi-material interface as described by Eq. (3.1.15), but further analyses would be required to make any general conclusions. However, the simulated kinking mechanism in the model is clearly affected by changing  $\mathcal{G}_{Ic}$  for the interface, which is in line with how a physical structure likely would behave.

### 5.3 Assessment of the modeled interaction between inter- and intralaminar cracks

When employing the FEM modeling approach in the present work, it is observed that the element size in the ply where the intralaminar crack initiates has an influence on the migration location. For both the SCB model and the L-flange, the tendency is that delamination migration can occur earlier i.e after a shorter distance of delamination

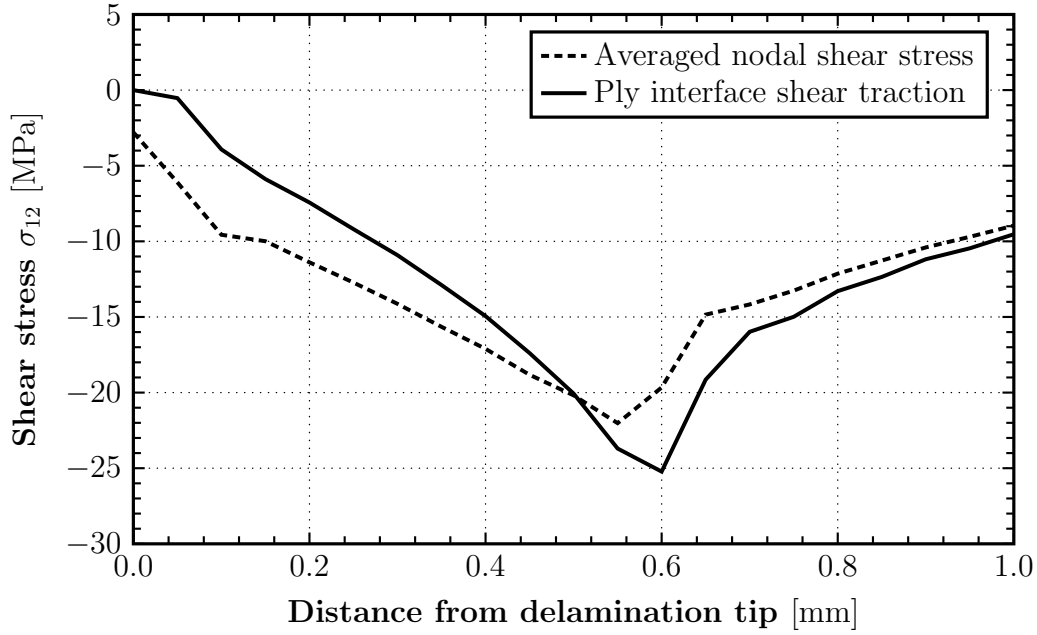


**Figure 5.19.** The averaged nodal shear stress calculated at the ply interface and the shear traction in the cohesive contact ahead of the physical delamination tip during propagation in the SCB model. The length of the cohesive zone in the ply interface at this instance is 0.61 mm.

propagation when a larger element size is being used. However, when decreasing the element size the migration location converges to one position. With respect to this observation, the meshes that are used in the present work are sufficiently refined, but the general modeling approach may suffer from related effects.

The first continuum element where the intralaminar crack is initiated during delamination migration is also subjected to the ply-interface contact formulation, where the constitutive behaviour is governed by the CZM. The stress state in the continuum element affects the interlaminar traction and vice versa. When the stiffness in this element is reduced due to damage of the XFEM-crack interface, the interlaminar traction locally decrease. If the continuum element is large, the reduced traction affects a longer part of the interlaminar cohesive zone, which have an impact on the damage progression ahead of the delamination. Hence, this can be a contributing factor to why the continuum element size influences the migration location.

Another observation regarding the interlaminar stress is that the shear traction from the cohesive contact formulation differs from the shear stress calculated to the continuum element nodes located at the ply interface. This can be seen in Fig. 5.19 where the nodal shear stress and the contact shear traction in the cohesive zone ahead

of the delamination tip is shown for the SCB model during propagation. Analytically, these quantities should be equal due force equilibrium. However, the stress in the continuum elements is calculated at the integration points, extrapolated to each node and averaged with the nodal stress from an adjacent element. The contact shear traction on the other hand is only calculated from the ply interface separation and stiffness at the current state of damage, related to the contact formulation and the CZM. It is thereby not surprising if a small difference between these quantities would occur numerically, but for the present case it is noteworthy. The cause can be found in the continuum elements where the degree of shear stress discontinuity is high close to the delamination front. This means that the relative difference in the shear stress calculated at the element level is high between adjacent elements. The degree of stress discontinuity is generally seen as an error indicator, related to the discretisation. In this case, it can be an effect from using first order elements in a region with high stress gradients which are not captured accurately. Refining the mesh further reduces the error but does not resolve the problem completely, since this is a very local phenomenon. Regardless of the cause of this issue, it will affect the stress state in the element where the intralaminar XFEM crack is initiated and can thereby have a critical impact on how the migration event is predicted by the model.



# Chapter 6

## Discussion and conclusions

An approach for modeling delamination migration in FRPs is utilised, where the XFEM and a surface-based contact formulation is combined with a cohesive zone model. A simulation strategy for dealing with the limitations of the XFEM implementation in *Abaqus/Standard* is employed to be able to predict the migration location. The two simulated structures show many similarities with the test results from the literature in terms of unstable crack propagation and the sequence of fracture events. For the SCB test, the predicted migration location is in good agreement with the experiment for all three load cases. Furthermore, the simulated migration angle and the maximum force during loading is comparable to the test results, although no distinct correlation is observed.

The migration location in the L-flange simulation is not as accurately predicted as in the case for the SCB test when comparing to the available results from the experiment. On the other hand, it is also demonstrated how relatively small variations of the ply interface properties changes the migration location and the failure of the structure. These are properties which are difficult to measure in practice, but clearly affects the simulation.

A pervading result in both FEM models is that the stiffness of the structure is significantly overpredicted, and failure occurs at a smaller displacement than in the experiments. This can be related to the machine compliance, which is unknown and thereby not accounted for in the models. Residual stresses from curing of the laminate, due to different coefficient of thermal expansion in the longitudinal and transverse fiber direction of the plies can also affect the load and displacement at failure in practice [34]. However, these two factors cannot entirely explain the difference between experiments and simulations, and a possibility is that the clamping of the specimens in the tests may allow some slip, which the idealised boundary conditions in the models do not.

The reported residual displacement after unloading of the SCB test in [33] indicates that this could be the case. It is not likely that the modeling of the plies and interfaces has a major influence on the overpredicted elastic stiffness, since previous simulations of the SCB test [12, 34] and the L-flange [29, 37] with other modeling techniques have generated similar results as in the present work.

The modeling approach suffers from two main issues. The first is that ply damage and intralaminar cracks are neglected prior to the point where complete delamination migration takes place. This is not optimal since it locally results in a maximum principal stress in the 90°-plies that is higher than the transverse tensile strength. The second issue is that the tedious process to find the location for delamination migration, by employing the simulation procedure from section 4.7, is time consuming and computationally expensive for large FEM models. However, with further improvements of the XFEM implementation concerning interactions between propagating cracks and more sophisticated fracture criteria, the modeling approach in the present work can be the basis for more accurate and efficient simulations of delamination migration in FRPs.

The representation of the ply with homogeneous material properties works good from an engineering point of view but cannot represent the effect on the crack path that the heterogeneous micro structure of the actual material may have. It is thereby difficult to say if the difference between the predicted intralaminar crack path and the paths observed in the experiments is caused by the simplification of the material properties or if the model fails to capture some effects. Concerns are expressed regarding the initiation of the XFEM crack close to the ply interface. It is only based on the maximum principle stress, while the kink mechanism clearly is a complex fracture event, and this simple criterion might not be sufficient.

Altogether, the modeling approach is performing well and the most relevant fracture events during the failure of the structures can be represented. By employing XFEM to model arbitrary intralaminar crack paths, further insight in the fracture process is provided while the method is both general and relatively mesh independent. The CZM is suitable for the progressive damage ahead of the crack tip and the crack modeling is thereby not only limited to the assumptions of LEFM. The results from the present work may contribute to further improvements of FEM models capable of simulating delamination migration, enabling the development of better computational tools for component design in FRPs.

## 6.1 Concluding remarks

A modeling strategy is developed that can simulate delamination migration in cross-ply FRPs under unstable conditions. The approach is computationally demanding but available within the framework of *Abaqus/Standard*, hence no implementation of new elements, discretisation schemes or damage models is required. The precision is accurate enough to predict delamination length, migration location and the approximate direction of intralaminar matrix cracks, which is generally in agreement with experimental results from the literature. It is also shown how the interface properties of a laminate have a significant impact on the crack path. However, the complete interaction between inter- and intralaminar cracks is most likely not captured in the FEM model, but has in the present work little effect on the overall failure of the structure. With further improvements of the modeling approach, more efficient and accurate simulations can be made, enabling better predictions of failure in FRP components in the future.

## 6.2 Future work

Based on the outcome of the present work, some suggestions for future research and improvements are given here.

- I. Enhancing the XFEM by implementing capabilities to model interactions between multiple propagating cracks, material interfaces and anisotropic materials. Additionally, higher order elements and crack tip enrichments to properly evaluate fracture criteria for propagating cracks can increase the accuracy.
- II. Extending the use of XFEM to model delamination, and possibly achieve a better representation of the interaction between inter- and intralaminar cracks.
- III. Enrichment of cohesive elements to model intra-element discontinuities.
- IV. Adding a continuum damage model to the present approach to account for ply damage where XFEM is not applicable.
- V. Dynamic analysis of the fracture events to include effects of crack propagation speed, inertia forces and strain rate.
- VI. Evaluation of the boundary conditions to better represent the experimental tests in the numerical models.





# Appendix A

**Table A.1.** *Experimental force-displacement data extracted from the SCB test in [33].*

$L = 1.1a_0$		$L = 1.2a_0$		$L = 1.1a_0$	
$U_2$ [mm]	$P$ [N]	$U_2$ [mm]	$P$ [N]	$U_2$ [mm]	$P$ [N]
0.0000	0.0	0.0000	0.0	0.0000	0.0
0.9371	273.6	1.0039	338.7	0.9108	347.9
0.9547	277.9	1.0156	338.7	0.9342	356.4
0.9605	280.0	1.0273	340.9	0.9459	356.4
0.9664	277.9	1.0332	343.0	0.9518	311.6
0.9664	273.6	1.0391	293.5	1.0044	324.4
0.9722	123.6	1.0450	291.4	1.0219	326.5
0.9781	121.4	1.0508	291.4	1.0278	313.7
0.9956	123.6	1.0566	293.5	1.0395	313.7
		1.0625	295.7	1.0570	320.1
		1.0742	297.8	1.0629	317.9
		1.0801	295.7	1.0629	313.7
		1.0859	78.5	1.0687	311.5
		1.0977	78.5	1.0863	74.4
		1.1094	80.6	1.0980	74.4
		1.1270	82.8		

**Table A.2.** *Experimental migration distance and crack angle from the SCB test, extracted from [33].*

Load offset $L/a_0$	Migration distance [mm]	Migration angle $\alpha$ [deg]
1.104	10.707	47
1.096	11.016	52
1.104	12.353	53
1.100	13.738	65
1.202	11.015	67
1.210	8.860	68
1.212	8.275	78
1.204	6.969	52
1.297	8.770	60
1.303	7.938	55
1.318	6.228	45

# Appendix B

**Table B.1.** *Experimental force-displacement data extracted from the L-flange test in [37].*

Specimen 1		Specimen 2		Specimen 3	
$U_2$ [mm]	$P$ [N]	$U_2$ [mm]	$P$ [N]	$U_2$ [mm]	$P$ [N]
0.0000	0.0	0.0000	0.0	0.0000	0.0
0.7333	209.2	0.6134	186.6	2.8134	681.2
1.8111	493.4	1.8711	519.5	2.8427	687.5
2.1778	588.2	2.2732	618.3	2.8515	314.6
2.5000	667.1	2.3866	647.6	2.9425	328.1
2.5667	682.8	2.3866	431.7	3.0833	347.9
2.6111	690.8	2.5103	457.3	3.2007	361.5
2.6111	659.2	2.9021	526.8	3.3650	380.2
2.6222	382.9	3.4175	611.0	3.5176	393.8
2.6778	394.7	3.6443	647.6	3.4237	386.5
2.7111	402.6	3.6856	651.2	3.6701	408.3
2.7555	406.6	3.6959	640.2	3.8110	419.8
2.9555	442.1				
3.0667	461.8				
3.1667	481.6				



# Bibliography

- [1] *Abaqus/Standard v6.14 Documentation*. Dassault Systems Simulia Corp., Providence, RI, USA, 2014.
- [2] T.L. Anderson. *Fracture mechanics: fundamentals and applications*. CRC Press, Boca Raton, Fla., 2nd edition, 1995.
- [3] I. Babuška and J.M. Melenk. The partition of unity method. *International Journal for Numerical Methods in Engineering*, 40(4):727, 1997.
- [4] G. Barenblatt. The mechanical theory of equilibrium cracks in brittle fracture. *Advances in Applied Mechanics*, 7:55–129, 1962.
- [5] T. Belytschko and T. Black. Elastic crack growth in finite elements with minimal remeshing. *International Journal for Numerical Methods in Engineering*, 45(5):601, 1999.
- [6] M.L. Benzeggagh and M. Kenane. Measurement of mixed-mode delamination fracture toughness of unidirectional glass/epoxy composites with mixed-mode bending apparatus. *Composites Science and Technology*, 56(4):439, 1996.
- [7] P.P. Camanho, J. Costa, C.G. Dávila, and A. Turon. An engineering solution for using coarse meshes in the simulation of delamination with cohesive zone models. Technical Report NASA/TM-2005-213547, NASA Langley Research Center, 2005.
- [8] P.P. Camanho and C.G. Dávila. Mixed-mode decohesion finite elements for the simulation of delamination in composite materials. Technical Report NASA/TM-2002-211737, NASA Langley Research Center, 2002.
- [9] B. Clegg. Brittle fracture. Dissemination of IT for the Promotion of Materials Science(DoITPoMS). [https://www.doitpoms.ac.uk/tlplib/brittle\\_fracture/printall.php](https://www.doitpoms.ac.uk/tlplib/brittle_fracture/printall.php) [Accessed on 18 January 2018].

- [10] Hexcel Corporation. *HexPly<sup>®</sup> 8552 Product Data Sheet*. Stamford, USA, 2016.
- [11] W. Cui and M.R Wisnom. A combined stress-based and fracture-mechanics-based model for predicting delamination in composites. *Composites*, 24(6):467–474, 1993.
- [12] N.V De Carvalho, B.Y. Chen, S.T Pinho, J.G Ratcliffe, P.M Baiz, and T.E. Tay. Modeling delamination migration in cross-ply tape laminates. *Composites Part A: Applied Science and Manufacturing*, 71:192–203, 2015.
- [13] D.S. Dugdale. Yielding of steel sheets containing slits. *Journal of the Mechanics and Physics of Solids*, 8:100–104, 1960.
- [14] F. Erdogan and G. Sih. On the crack extension in plates under plane loading and transverse shear. *ASME Journal of Basic Engineering*, 85(4):519–527, 1963.
- [15] T.P. Fries and T. Belytschko. The extended/generalized finite element method: An overview of the method and its applications. *International Journal for Numerical Methods in Engineering*, 84:253–304, 2010.
- [16] J. Gager and H.E. Pettermann. Numerical homogenization of textile composites based on shell element discretization. *Composites Science and Technology*, 72(7):806–812, 2012.
- [17] Y.F Gao and A.F Bower. A simple technique for avoiding convergence problems in finite element simulations of crack nucleation and growth on cohesive interfaces. *Modelling and Simulation in Materials Science and Engineering*, 12(3):453, 2004.
- [18] A.A. Griffith. The phenomena of rupture and flow in solids. *Philosophical Transactions of the Royal Society of London. Series A, Containing Papers of a Mathematical or Physical Character*, pages 163–198, 1921.
- [19] M.Y. He and J.W. Hutchinson. Kinking of a crack out of an interface. *Journal of Applied Mechanics*, 56:270–278, 1989.
- [20] A. Hillerborg, M. Mod er, and P.-E. Petersson. Analysis of crack formation and crack growth in concrete by means of fracture mechanics and finite elements. *Cement and Concrete Research*, 6(6):773–781, 1976.
- [21] X.F. Hu, B.Y. Chen, M. Tirvaudey, V.B.C Tan, and T.E Tay. Integrated xfem-ce analysis of delamination migration in multi-directional composite laminates. *Composites Part A: Applied Science and Manufacturing*, 90:161–173, 2016.

- [22] G.R. Irwin. Analysis of stresses and strains near the end of a crack traversing a plate. *Journal of Applied Mechanics – Transactions of the ASME*, E24:351–369, 1957.
- [23] A.R. Khoei. *Extended Finite Element Method: Theory and Applications*. John Wiley & Sons, Ltd, West Sussex, UK, 1st edition, 2014.
- [24] I. Lapczyk and J.A. Hurtado. Progressive damage modeling in fiber-reinforced materials. *Composites Part A: Applied Science and Manufacturing*, 38(11):2333–2341, 2007.
- [25] J. Lemaitre. A continuous damage mechanics model for ductile fracture. *Journal of Engineering Materials and Technology*, 107:83–89, 1985.
- [26] X. Li and J. Chen. A highly efficient prediction of delamination migration in laminated composites using the extended cohesive damage model. *Composite Structures*, 160:712–721, 2017.
- [27] D. Ling, Q. Yang, and B. Cox. An augmented finite element method for modeling arbitrary discontinuities in composite materials. *International Journal of Fracture*, 156(1):53–73, 2009.
- [28] D.S. Ling, X.J. Fang, B.N. Cox, and Q.D. Yang. Nonlinear fracture analysis of delamination crack jumps in laminated composites. *Journal of Aerospace Engineering*, 24(2):181–188, 2011.
- [29] E.R. Lista. *Finite element simulations of laminated composites under consideration of nonlinear ply material and delamination*. Diploma thesis, TU Wien, 2012.
- [30] N. Moës, J. Dolbow, and T. Belytschko. A finite element method for crack growth without remeshing. *International Journal for Numerical Methods in Engineering*, 46(1):131–150, 1999.
- [31] S. Murakami. *Continuum damage mechanics: a continuum mechanics approach to the analysis of damage and fracture*. Springer, Dordrecht, USA.
- [32] N.S. Ottosen and H. Petersson. *Introduction to the finite element method*. Prentice Hall, New York, USA, 1992.

- [33] J.G. Ratcliffe, M.W. Czabaj, and T.K. O'Brien. A test for characterizing delamination migration in carbon/epoxy tape laminates. Technical report, National Aeronautics and Space Administration, 2013.
- [34] M. Schasching. *Finite Elemente Simulation einer Composite-Struktur – Interaktion Schichtschädigung und Delamination*. Diploma thesis, TU Wien, 2017.
- [35] G.C. Sih. Strain-energy-density factor applied to mixed mode crack problems. *International Journal of Fracture*, 10(3):305, 1974.
- [36] H.M.W. Westergaard. Bearing pressures and cracks. *Journal of Applied Mechanics*, 6:A49–A53, 1939.
- [37] G. Wimmer. *Computational methods for the prediction of emergence and growth of delaminations in laminated composite components*. Dissertation thesis, TU Wien, 2009.
- [38] L. Zhao, J. Zhi, J. Zhang, Z. Liu, and N. Hu. Xfem simulation of delamination in composite laminates. *Composites Part A: Applied Science and Manufacturing*, 80:61–71, 2016.